SOFT X-RAY EMISSION SPECTROSCOPY STUDY OF A CATHODE MATERIAL FOR LI-ION BATTERIES IN COMBINATION WITH FULL-MULTIPLET CALCULATION

Daisuke Asakura[1,2], Yusuke Nanba[1,#], Eiji Hosono[1,2], Hideharu Niwa[3,4,†], Hisao Kiuchi[5,$], Jun Miyawaki[3,4], and Yoshihisa Harada[2,3,4]

[1]*Research Institute for Energy Conservation, National Institute of Advanced Industrial Science and Technology (AIST)*

[2]*AIST-UTokyo Advanced Operando-Measurement Technology Open Innovation Laboratory, AIST*

[3]*Synchrotron Radiation Laboratory, The Institute for Solid State Physics, The University of Tokyo*

[4]*Synchrotron Radiation Research Organization, The University of Tokyo*

[5]*Department of Applied Chemistry, The University of Tokyo*

Present affiliations: [#]Shinshu University, [†]University of Tsukuba, [$]Kyoto University

Enhancement of the energy-density and power-density of electrode materials is one of the important subjects in the research field of Li-ion batteries (LIBs). To improve the performances of electrode materials, the redox mechanisms due to Li-ion extraction/insertion should be clarified. In this study, high-energy-resolution soft x-ray emission spectroscopy (XES) was applied to understand changes in the electronic structure of $LiMn_2O_4$ cathode [1] by Li-ion extraction/insertion[2]. The Mn 2*p*-3*d*-2*p* resonant XES spectra were analyzed by the configuration-interaction full-multiplet (CIFM) calculation, which reproduced both *dd* and charge-transfer (CT) excitations.

The $LiMn_2O_4$ sample was fabricated by a sol-gel method. For electrochemical experiments, $LiMn_2O_4$ (75 wt%), acetylene black (20 wt%), and polytetrafluoroethylene (5 wt%) were ground into a paste. Lithium metal was used as the counter and reference electrodes, and 1M ethylene carbonate (EC)/diethyl carbonate (DEC) solutions of $LiClO_4$ were used as electrolytes for a three-electrode beaker cell. We prepared three samples for initial (before charging), charged, and discharged states by constant-current charge-discharge experiments with a current density of 10 mA/g. The corresponding voltages for the three states were 3.2, 4.3 and 3.2 V vs. Li/Li^+, respectively. Mn 2*p*-3*d*-2*p* resonant XES measurements for the $LiMn_2O_4$ samples were carried out at BL07LSU in SPring-8 using a high resolution XES spectrometer, HORNET[3]. The total energy resolution for XES was set to $E/\Delta E$ = 3200 at the Mn L_3 edge. All the XES measurements were carried out at room temperature in a high vacuum. The CIFM calculation for the electronic-structure analysis of Mn atoms in $LiMn_2O_4$ was carried out by assuming an octahedral MnO_6 cluster in which the Mn 3*d* and O 2*p* orbitals and the charge-transfer effect were taken into account[4].

The resonant XES spectra taken with an excitation energy of 642.0 eV corresponding to a Mn L_3-edge absorption peak showed drastic changes between the initial and charged states (Fig. 1). The initial state should be attributed to a mixed valence state of Mn^{3+}/Mn^{4+}. For the initial state, all the Mn^{3+} should be oxidized to Mn^{4+}. Fo

r the discharged state, the Mn ions should partially be reduced to Mn^{3+}. Between the initial and discharged state, the small changes of the ratio of Mn^{3+}/Mn^{4+} was detected by the use of resonant XES.

To confirm the changes and separately understand the Mn^{3+} and Mn^{4+}states, we analyzed the XES spectra by using the CIFM calculation (Fig. 2), while the Mn^{4+} state was regarded as unchanged during charge-discharge. Both the oxidation states have strong ligand-to-metal CT effect. In particular for the Mn^{4+} (charged) state, the CT energy Δ was highly negative, resulting in the dominant $d^4\underline{L}$ and $d^5\underline{L}^2$ charge transfer configurations. The present results

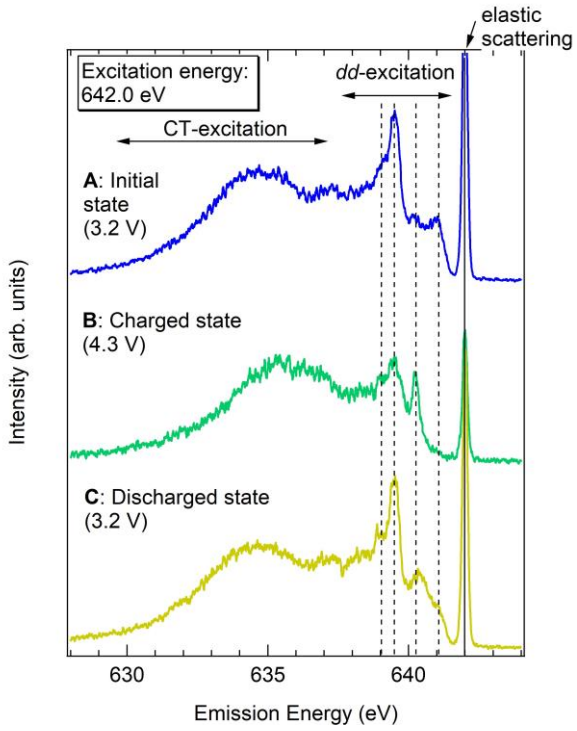

Fig. 1. Mn 2*p*-3*d*-2*p* resonant XES spectra for $LiMn_2O_4$ at the initial, charged and discharged states[2].

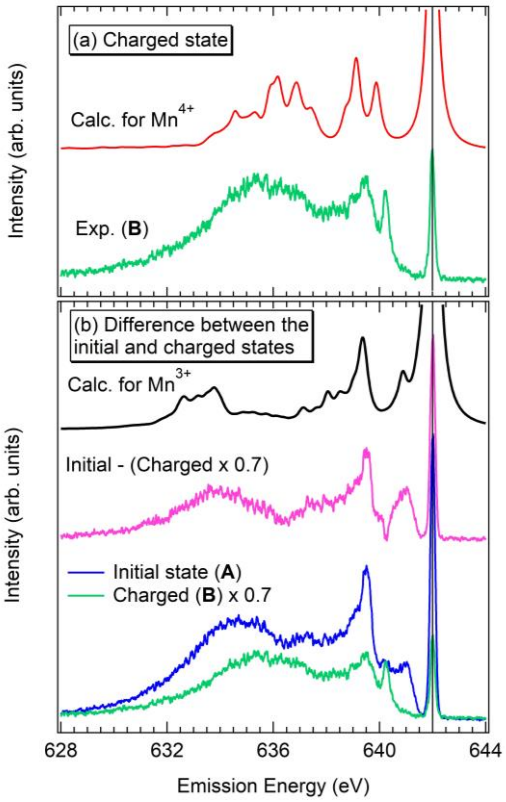

Fig. 2. CIFM calculation for (a) Mn^{4+} with the charged state and (b) Mn^{3+} states with a difference spectrum between the initial and charged states[2].

indicate possible reasons for the capacity fading in $LiMn_2O_4$: instability of the crystal-structure during charge-discharge and Jahn-Teller distortion at the Mn^{3+} site.

In summary, we measured Mn 2*p*-3*d*-2*p* resonant XES for $LiMn_2O_4$. Detailed information of the electronic-structure change such as the strong CT effect was obtained. In the near future, we will perform O 1*s*-2*p*-1*s* XES measurement to further understand the redox reaction.

REFERENCES

[1] For example, M. M. Thackeray, Prog. Solid State Chem. **25**, 1 (1997).
[2] D. Asakura *et al*., Phys. Chem. Chem. Phys. **21**, 18363 (2019).
[3] Y. Harada *et al*., Rev. Sci. Instrum. **83**, 013116 (2012).
[4] For example, D. Asakura *et al*., J. Phys. Chem. Lett. **5**, 4008 (2014).

DEVELOPMENT OF ALL-SOLID-STATE LI-ION-BATTERY CELL FOR OPERANDO SOFT X-RAY EMISSION SPECTROCOSPY

Daisuke Asakura[1,2], Eiji Hosono[1,2], Kosuke Yamazoe[3,4], Jun Miyawaki[3,4], and Yoshihisa Harada[2,3,4]

[1]*Research Institute for Energy Conservation, National Institute of Advanced Industrial Science and Technology (AIST)*

[2]*AIST-UTokyo Advanced Operando-Measurement Technology Open Innovation Laboratory, AIST*

[3]*Synchrotron Radiation Laboratory, The Institute for Solid State Physics, The University of Tokyo*

[4]*Synchrotron Radiation Research Organization, The University of Tokyo*

Development of high-performance lithium-ion battery (LIB) for electric vehicles is a one of the important research subjects to realize a sustainable low-carbon society. However, the trade-off relationships among the performances such as energy density, power performance, cycle performance, and safety property make the development difficult. Moreover, the combination of the materials among the cathode, anode, and electrolyte is crucial for the improvement of total performances of LIB. Thus, comprehensive researches and developments are highly important. In addition to the materials design, cutting-edge analyses are inevitable because understanding of the redox reactions and structural/electronic properties for the materials in LIBs is necessary to design/create innovative materials for LIBs.

Synchrotron radiation X-ray spectroscopy is a powerful technique to understand the crystal structure and electronic structure in LIB materials. We have been studying the charge-discharge mechanisms in LIBs based on the electronic-structure analysis by using soft X-ray spectroscopy at HORNET, BL07LSU. Especially, the redox reactions of electrode materials have been investigated by *operando* soft x-ray emission spectroscopy under the charge-discharge operation [1,2]. The *operando* cell consists of special electrode chip directly grown on Si_3N_4 thin-film window, counter electrode and electrolyte solution. On the other hand, all-solid-state LIB with solid-state electrolyte is of particular importance. We have already developed an all-solid-state-type *operando* cell for *operando* photoemission spectromicroscopy at 3DnanoESCA, BL07LSU [3,4].

In this study, we tried to install the all-solid-state-type *operando* cell for the HORNET chamber to perform *operando* soft x-ray emission spectroscopy for the all-solid-state LIBs. A special transfer vessel was developed to transfer the *operando* cell from a glove box filled with Ar gas to vacuum chamber without air exposure, because the *operando* cell includes a Li-metal counter electrode. The transfer vessel was fixed to the HORNET chamber and the *operando* cell was moved to the beam position (Figs. 1(a) and 1(b)).

The working electrode of the *operando* cell was $LiCoO_2$, a cathode material, which was single crystalline particles. The particles were mixed with a binder as a slurry and fixed on a carbon micro grid with an Au mesh (Fig. 1(d)). Then, the working electrode was stacked with the solid-state electrolyte sheets and Li-metal counter electrode as shown in Fig. 1(d).

Figure 1(c) shows the Co L_3-edge soft X-ray emission spectra for different 4 positions on the working electrode. For all the points, the intensity was too small, indicating that there were few $LiCoO_2$ particles. Because the size of the particles (μm order) is comparable with the beam size, it was difficult to find the positions of the small number of the particles. The density of the particles on the Au mesh should be much higher. On the other hand, we succeeded in the electrochemical charge-discharge using the *operando* cell and detecting the

signals of Co L_3-edge soft X-ray absorption by the total-electron yield detection mode.

In summary, we installed an all-solid-state-type *operando* cell for the HORNET chamber. The intensity of the Co L_3-edge soft X-ray emission spectra for the $LiCoO_2$ working electrode was too weak due to the small number of the μm-order particles. In the near future, we will increase the number of the particles by modifying the cell structure in order to perform soft X-ray emission measurement for the all-solid-state-type *operando* cell.

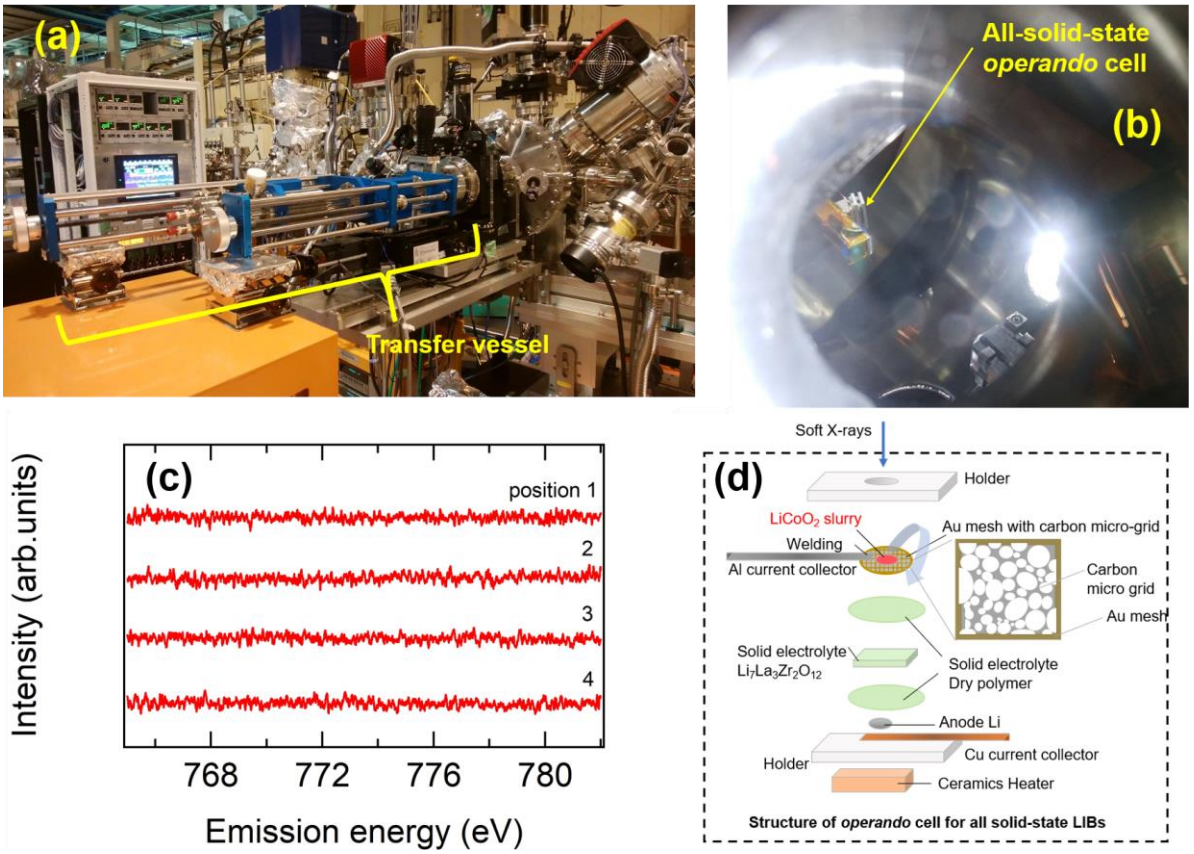

Fig.1. (a) A picture of the transfer vessel fixed with the HORNET chamber. (b) A picture of the inserted all-solid-state-type *operando* cell into the main chamber taken via a viewport. (c) Co L_3-edge soft X-ray emission spectra for different 4 positions on the working electrode. (d) A schematic picture of the all-solid-state-type *operando* cell [3,4].

REFERENCES

[1] D. Asakura *et al*., Electrochem. Commun. **50**, 93 (2015).
[2] D. Asakura *et al*., Phys. Chem. Chem. Phys. **21**, 26351 (2019).
[3] K. Akada *et al*., J. Electron Spectrosc. Relat. Phenom. **233**, 64 (2019).
[4] K. Akada *et al*., Sci. Rep. **9**, 12452 (2019).

VERIFICATION OF TWO-CARRIER STATE IN THE CUPRATE SUPERCONDUCTOR $Pr_{1.4-x}La_{0.6}Ce_xCuO_4$

Kenji Ishii[1], Shun Asano[2], Masaki Fujita[2],
Kohei Yamagami[3], Jun Miyawaki[3], Yoshihisa Harada[3]
[1]*Synchrotron Radiation Research Center, National Institutes for Quantum and Radiological Science and Technology*
[2]*Intsitute for Materials Research, Tohoku University*
[3]*Synchrotron Radiation Laboratory, The Institute for Solid State Physics, The University of Tokyo*

High-transition-temperature superconductivity in the cuprates occurs when either holes or electrons are doped into parent antiferromagnetic Mott insulators. Dope holes occupy the oxygen 2*p* orbitals predominantly. In contrast, electrons are doped into the Cu 3*d* orbital but doping evolution of the electronic states of the "nominally" electron-doped cuprates is not so simple. Most electron-doped cuprate superconductors have the chemical formula $RE_{2-x}Ce_xCuO_4$ (*RE* = La, Pr, Nd, Sm, Eu) and electrons are doped via partial substitution of trivalent *RE* with tetravalent Ce. At low Ce concentration (*x*), Hall and Seebeck coefficients, which are often used to determine the sign and number of carriers, are negative as expected. However, the coefficients change the sign in the temperature dependence in the intermediate concentration and the sign becomes positive in entire measured temperature at high concentration ($x > 0.155$ for RE = Pr and $x > 0.135$ for *RE* = La) [1-3]. Furthermore, reconstruction of the Fermi surface with increasing the Ce concentration is observed in ARPES [4] and quantum oscillation [5]. Recently, it was reported in a transport study [6] that superconductivity in the nominally electron-doped cuprates emerges under the coexistence of holes and electrons and a relation between the superfluid density of holes and the superconducting transition temperature agrees with that of hole-doped cuprates. This result indicates that the superconductivity in the nominally electron-doped cuprates is driven by the holes rather than the electrons and a unified mechanism of the superconductivity exists irrespective of the type of carries.

In this study, we aim to verify the two-carrier states in the nominally electron-doped cuprates, especially to prove the existence of the holes by means of x-ray absorption spectroscopy (XAS) and resonant inelastic x-ray scattering (RIXS) at the oxygen *K*-edge. In the hole-doped cuprates, O *K*-edge XAS gave a direct evidence of the holes in the O 2*p* orbitals [7]; a peak at the pre-edge is ascribed to the hole state. In addition, we recently demonstrated that O *K*-edge RIXS is sensitive to the charge excitations of the doped holes [8].

The experiment was performed using the HORNET spectrometer at BL07LSU of SPring-8. Total energy resolution of RIXS was 150 meV. For the present study, we selected $Pr_{1.4-x}La_{0.6}Ce_xCuO_4$ (PLCCO), in which superconductivity is observed in wide Ce concentration (*x*). We prepared single crystals of superconducting $x = 0.16$ and non-superconducting $x = 0.08$. The crystals of were cleaved in the air just before the measurement and σ-polarized x-rays were irradiated on the *ab*-plane of the crystal. The *ac*-plane was parallel to the horizontal scattering plane and momentum transfer in the CuO_2 plane (***q***) was scanned by rotating the crystal along the vertical *b*-axis. Scattering angle (2θ) was kept at 135° and temperature of the crystals was about 15 K.

The inset of Fig. 1 shows an XAS spectrum of PLCCO $x = 0.16$. The peak at 528.8 eV originates from the absorption to the Cu 3*d* upper Hubbard band (UHB) hybridized with the O 2*p* states. In the hole doped cuprates, absorption to the O 2*p* hole states appears at lower energy of the UHB peak but we cannot find any trace of the hole states in PLCCO. The main panel of Fig. 1 shows incident energy (E_i) dependence across the UHB peak in XAS as indicated by vertical bars in the inset. A Raman feature at 0.4 eV is observed at $E_i \leq 528.7$ eV and it gradually charges to fluorescence at higher E_i.

Figure 2 shows momentum dependence of RIXS measured at E_i = 528.5 eV. In the four spectra from the bottom, lines in light color present raw data and elastic scattering is subtracted for the lines in deep color. The subtracted spectra are overlaid at the top. Most of the spectral weight below 1eV is independent of the momentum and two-magnon excitation is a possible origin. In stark contrast, spectral weight in O *K*-edge RIXS exhibits large momentum dependence in hole-doped cuprates [8]. Though it is tiny, a momentum-dependent component is discernible in Fig. 2. Because the component follows the momentum dependence of the charge excitations observed in Cu *K*- and L_3-edge RIXS [9,10], it is reasonably ascribed to the same charge origin through the hybridization between Cu 3*d* and O 2*p* orbitals. Regarding the doping dependence, the momentum-independent spectral weight is similarly observed, intensity of the momentum-dependent component is weaker in x = 0.08.

In summary, present XAS and RIXS results of PLCCO are comprehensible without assuming the existence of the holes in the O 2*p* orbitals. Even if the holes exist in the nominally electron-doped cuprates, their orbital character is qualitatively different from that of the O 2*p* holes in hole-doped cuprates.

REFERENCES

[1] Y. Dagan et al., Phys. Rev. Lett. **92**, 167001 (2004).
[2] P. Li et al., Phys. Rev. B **75**, 020506 (2007).
[3] R. L. Greene et al, Annu. Rev. Condens. Matter Phys. **11**, 213 (2020).
[4] N. P. Armitage et al., Phys. Rev. Lett. **88**, 257001 (2002).
[5] T. Helm et al., Phys. Rev. B **92**, 094501 (2015).
[6] Y. Li et al., Sci. Adv. **5**, eaap7349 (2019).
[7] C. T. Chen et al., Phys. Rev. Lett. **66** ,104 (1991).
[8] K. Ishii et al., Phys. Rev. B **96** ,115148 (2017).
[9] K. Ishii et al., Phys. Rev. Lett. **94** ,207003 (2005).
[10] K. Ishii et al., Nat. Commun. **5**, 3714 (2014).

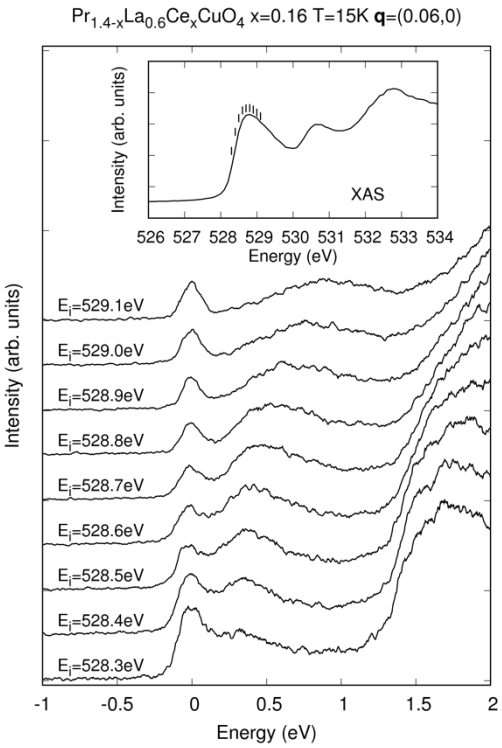

FIG. 1: Incident energy dependence of O *K*-edge RIXS in PLCCO x = 0.16. Inset shows XAS at the edge.

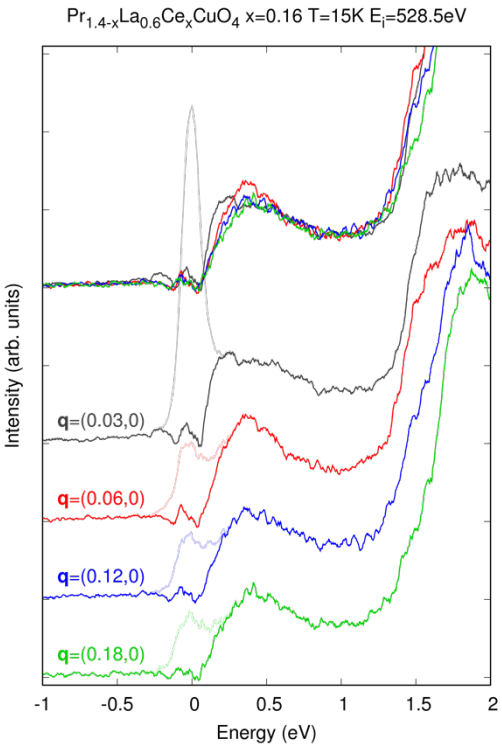

FIG. 2: Momentum dependence of O *K*-edge RIXS in PLCCO x = 0.16.

SPIN-POLARIZED ELECTRONIC STATE OF SINGLE CRYSTAL Co_2MnSi HEUSLER ALLOY PROBED BY RESONANT INELASTIC SOFT X-RAY SCATTERING (SX-RIXS) IN MAGNETIC FIELD

Rie Y. Umetsu[1], Hidenori Fujiwara[2], Jun Miyawaki[3,4], Kohei Nishimoto[2], Toshiyuki Kashiuchi[2], Akira Sekiyama[2], Akinori Irizawa[5] Yoshihisa Harada[3,4] and Shigemasa Suga[5]

[1] *Institute for Materials Research (IMR), Tohoku University*
[2] *Graduate School of Engineering Science, Osaka University, Osaka, Japan*
[3] *The Institute for Solid State Physics (ISSP), The University of Tokyo, Japan*
[4] *Synchrotron Radiation Research Organization, The University of Tokyo, Japan*
[5] *Institute of Scientific & Industrial Research, Osaka University, Osaka, Japan*

Introduction

It has been predicted from theoretical calculations that some of Mn- and Co-based Heusler alloys are half-metallic ferro- or ferri-magnets with the spin polarization of ~100 % around the Fermi energy (E_F) [1-3]. If the electrons are completely polarized around E_F, it is very efficient as a magnetic electrode in various spin dependent devices in the field of spintronics.

In the aspect of the fundamental investigations for half-metallic materials, it has been considered how to show the real evidence of the characteristic electronic structure. Attempts have been made worldwide to observe the detailed electronic state of Heusler alloys by photoelectron spectroscopy. Although a magnetic field must be applied in order to make a sample into a single domain state, the photoelectron orbit is greatly affected by the magnetic field. In our previous work, we have first studied the detailed electronic structure and magnetic properties of a single crystal Mn_2VAl by SX-RIXS measurements in magnetic field [4]. The RIXS is a bulk sensitive photon-in and photon-out spectroscopy, and very powerful to investigate such as *d*-*d* excitations for open shell 3*d* orbitals and magnetic excitations for spin systems as well as 2*p*-3*d* transitions in element- and symmetry-specific ways. In this study, we performed the RIXS experiments for single crystal of Co_2MnSi Heusler alloy, which was predicted to be a half-metallic ferromagnet.

Experiments

a) Sample preparation

A single crystal of Co_2MnSi was prepared by the Bridgman method after preparing a master alloy by arc melting in Ar gas atmosphere, and subjected to homogenizing heat treatment at 1373 K. The sample composition identified by an electron probe microanalyzer is Co:50.0, Mn:25.9, Si:24.1 at.%. Crystal orientation was checked by the Laue method and the specimens were cut out in the stripe form with the length of 6 mm along the <100> with about 1×1 mm^2 cross section. Magnetic properties were investigated with SQUID magnetometer and the spontaneous magnetization at 5 K was 142.2 emu/g (= 5.1 μ_B/f.u.), being comparable to the literature [5].

b) RIXS experiment

RIXS experiments were performed using a high-resolution soft X-ray emission spectrometer installed at the end of the BL07LSU of SPring-8. The specimen with the (001) plane was fractured in a glove box with Ar gas atmosphere, and then transferred into the analyzer chamber without exposure to the air. The RIXS spectra for Co and Mn 2*p* core excitation were measured with use of the right and left helicity circularly polarized light at room temperature. A permanent magnet with the field of 0.25 T was installed in the chamber and arranged as the X-ray incidence direction and the magnetic field direction become parallel [6].

Results

Figures indicate RIXS spectra obtained in parallel (μ^+) and antiparallel (μ^-) configurations between the photon helicity and the magnetic field at incoming photon energy, $h\nu_{in}$ of 779.0 eV (left figure) and 640.5 eV (right figure) for the Co and Mn-2$p_{3/2}$ edges, respectively. These photon energies correspond to the peak positions of the Co and Mn-2$p_{3/2}$ absorption spectra for the Co_2MnSi. Intensity peaks without any energy loss are the elastic component, and the other peaks in the larger energy loss region are the so-called fluorescence peaks. As shown in the figures, clear fluorescence components were observed and their circular polarization dependence (MCD = $\mu^+ - \mu^-$) was also confirmed. This RIXS-MCD signals originate from the spin-selective dipole-transition from $m_j = \pm 3/2$ which is separated by the Zeeman splitting due to the effective magnetic field of 3*d* electron states [4]. It was found that the positive and negative MCD fluorescence components in both Co and Mn have a large contribution of fluorescence from m_j = +3/2 and −3/2, respectively, suggesting that the valence band electronic structures of Co_2MnSi is highly spin-polarized.

References

[1] R.A. de Groot, F.M. Mueller, P.G.van Engen, K.H.J. Buschow, Phys. Rev. Lett. 50 (1983) 2024-2027.
[2] J.J. Kübler, A.R. Williams, C.B. Sommers, Phys. Rev. B 28 (1983) 1745-1755.
[3] S. Ishida, S. Akazawa, Y. Kubo, J. Ishida, J. Phys. F 12 (1982) 1111-1122.
[4] R.Y. Umetsu, H. Fujiwara, K. Nagai, Y. Nakatani, M. Kawada, A. Sekiyama, F. Kuroda, H. Fujii, T. Oguchi, Y. Harada, J. Miyawaki, S. Suga, Phys. Rev. B 99 (2019) 134414.
[5] R.Y. Umetsu, K. Kobayashi, A. Fujita, R. Kainuma, K. Ishida, Scripta Mater. 58 (2008) 723-726
[6] J. Miyawaki, S. Suga, H. Fujiwara, H. Niwa, H. Kiuchi, Y. Harada, J. Synchro. Rad. 24 (2017) 449-455.

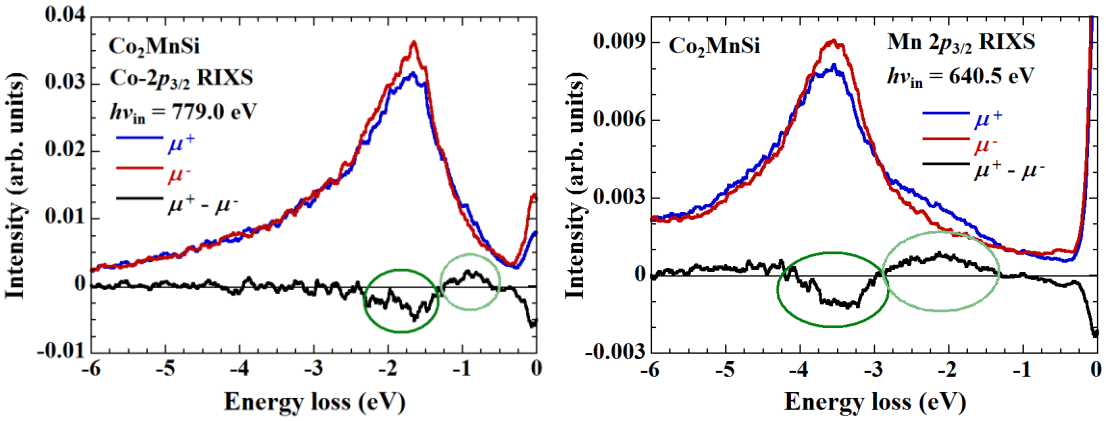

Figs. RIXS spectra recorded for parallel (μ^+) and antiparallel (μ^-) configurations of the photon helicity at Co-2$p_{3/2}$ with incident photon energy, $h\nu_{in}$ of 779.0 eV (left figure) and at Mn-2$p_{3/2}$ of 640.5 eV (right figure). Black lines indicate MCD (=$\mu^+ - \mu^-$).

MULTIORBITAL BOND FORMATION FOR STABLE OXYGEN-REDOX REACTION IN BATTERY ELECTRODES

Masashi Okubo
Department of Chemical System Engineering, School of Engineering, The University of Tokyo

The development of advanced electrochemical energy storage devices has been an active research field because it offers sustainability prospects, for instance, reduction of fossil fuel reliance by realizing an electric vehicle range of 500 km per charge or integrating renewable energy sources to an electrical grid. Market-leading lithium-ion batteries (LIBs) efficiently store energy by lithium-ion (de)intercalation associated with redox reactions. However, their energy density approaches the theoretical limit, in part owing to the small capacity of the positive electrode materials, which severely obstructs the wide deployment of LIBs. Therefore, it is important to find an alternative battery chemistry that can exceed the existing positive-electrode capacity limits.

The use of the extra redox reactions of oxygen in addition to conventional transition-metal redox reactions is an attractive way to increase the capacity of transition-metal oxides.[7] In general, most oxygen 2*p* orbitals in conventional electrode materials LiMO$_2$ (M: transition metal) form σ-type bonds with axial M 3*d* orbitals (e_g orbitals in an O_h symmetry). As the atomic energy level of oxygen 2*p* orbitals is usually lower than that of M e_g orbitals, the σ-type bonding orbitals are predominantly from oxygen 2*p* orbitals. Therefore, it is difficult to oxidize oxygen 2*p* orbitals that have a σ-type bonding character. However, research groups led by Bruce and Ceder postulated that oxygen in Li-excess transition-metal oxides Li$_{1+x}M_{1-x}$O$_2$ (Fig. 1a) intrinsically have localized ('orphaned') 2*p* orbital along the Li−O−Li axis without the σ-type bonding character, which can contribute to an additional oxygen-redox capacity. Indeed, large capacities exceeding the capacity limit of M redox reactions have been reported for many Li-excess transition-metal oxides including Li$_2$MnO$_3$-LiMO$_2$ solid solution, layered honeycomb Li$_2$IrO$_3$, random rock salt Li$_{1.2}$Ti$_{0.4}$Mn$_{0.4}$O$_2$, three-dimensional β-Li$_2$IrO$_3$, and anti-fluorite Li$_5$FeO$_4$. However, despite the theoretical adequacy of the proposed 'orphaned' oxygen 2*p* orbital hypothesis, the existence of the localized oxygen 2*p* orbitals in Li-excess transition-metal oxides has not been verified experimentally. Furthermore, although localized, the oxygen 2*p* orbital along the Li−O−Li axis still has a π-type interaction with the M t_{2g} orbital, which should play an essential role in oxygen-redox reactions. It is important to emphasize that the rigid-band model, which was frequently used for

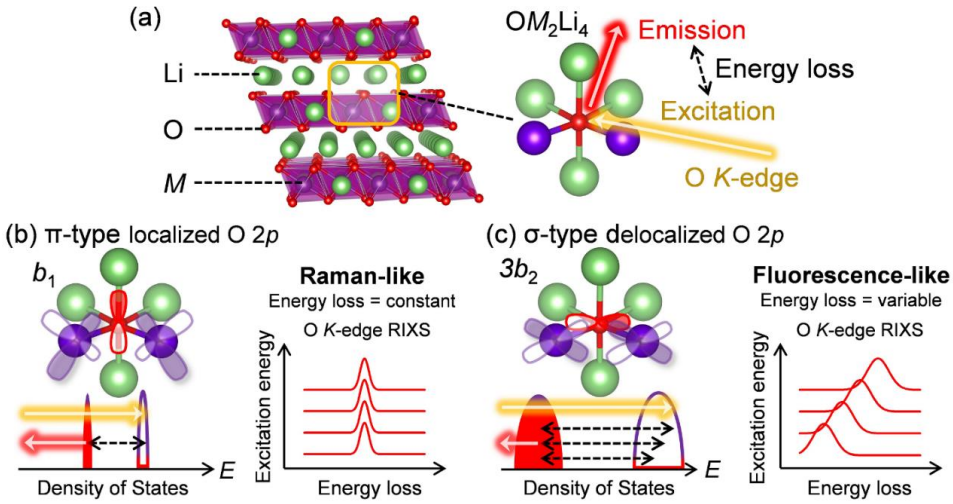

Figure 1. Resonant inelastic X-ray scattering (RIXS) spectra for delocalized and localized oxygen 2*p* orbitals. (a) Crystal structure of Li-excess layered transition-metal oxides Li[Li$_x$$M_{1-x}$]O$_2$ (M: transition metal). (b) π-type localized occupied/unoccupied states consisting of oxygen 2*p* and M t_{2g} orbitals (b_1/b_1^* bands in a C_{2v}-symmetry O$M$$_2Li_4$ cluster). (c) σ-type delocalized occupied/unoccupied states consisting of oxygen 2*p* and M e_g orbitals ($3a_1$/$3a_1^*$ and $3b_2$/$3b_2^*$ bands in a C_{2v}-symmetry O$M$$_2Li_4$ cluster).

consideration of oxygen-redox electrodes, cannot qualitatively discuss M–O interaction (*e.g.*, covalency), because it only considers a bandwidth and a band center energy of each band. Therefore, for a thorough understanding of the reversible oxygen-redox reactions occurring in Li-excess transition-metal oxides, it is necessary to clarify the nature of the π-type bonds during the oxygen-redox reactions from the molecular orbital viewpoint. In this work, we used oxygen *K*-edge resonant inelastic X-ray scattering (RIXS) spectroscopy combined with *ab initio* computations to demonstrate (σ + π) multiorbital bond formation as a firm criterion for stable oxygen-redox reactions.

Oxygen *K*-edge RIXS spectroscopy was used to examine the existence of π-type localized oxygen 2*p* orbitals in Li_2MnO_3, a standard Li-excess layered transition-metal oxide. Oxygen *K*-edge RIXS spectroscopy records the inelastic scattering during core excitation–relaxation (1*s*→2*p*→1*s*), in which the energy loss corresponds to valence excitation between occupied and unoccupied 2*p* bands. RIXS spectroscopy has a probing depth of approximately 100 nm (bulk sensitive). Importantly, when occupied/unoccupied oxygen 2*p* bands have a localized character with weak orbital hybridization, the inelastic scattering becomes Raman-like and has constant energy loss regardless of the incident photon energy (Fig. 1b). Conversely, delocalized occupied/unoccupied oxygen 2*p* bands with a large orbital hybridization gives fluorescence-like inelastic scattering with variable energy loss depending on the incident photon energy (Fig. 1c). Therefore, oxygen *K*-edge RIXS spectroscopy allows us to diagnose localized or delocalized oxygen 2*p* bands.

The *ab initio* calculations using HSE06 hybrid functional for Li_2MnO_3 indicates that a localized oxygen 2*p* orbital exists along the Li–O–Li axis with an orbital energy of approximately −0.9 to 0.0 eV versus the Fermi energy (Fig. 2a). The RIXS spectra and the corresponding second differential RIXS map (Fig. 2b and 2c) exhibit two broad fluorescence-like peaks, which could be related to the valence excitation between the σ-type wide oxygen 2*p* bands strongly hybridized with axial Mn e_g orbitals (Fig. 1c). Based on the C_{2v} symmetry of an OMn_2Li_4 cluster, these bands are labelled as $3a_1/3b_2$ bands. More importantly, the RIXS spectra show an intense Raman-like peak with constant energy loss of approximately 2.5 eV. This Raman-like peak clearly indicates the existence of the π-type narrow oxygen 2*p* bands weakly hybridized with Mn t_{2g} orbitals (b_1/b_1^* bands based on the C_{2v}-symmetry labelling, Fig. 1b). It is important to note that the Raman-like feature is not the simple projection of the *d*-*d* excitation of Mn *L*-edge, because O *K*-edge XAS and RIXS involve charge-transfer processes through O-Mn interactions. In contrast, for a non-Li-excess layered oxide $LiNi_{1/3}Co_{1/3}Mn_{1/3}O_2$, the RIXS spectra show only fluorescence-like peaks with variable energy loss depending on the incident photon energy because most oxygen 2*p* orbitals form σ-type wide bands with axial *M* 3*d* orbitals. Therefore, this is the first experimental verification of the 'orphaned' oxygen 2*p* orbital hypothesis for Li-excess transition-metal oxides, and oxygen *K*-edge RIXS spectroscopy is definitely an effective diagnostic tool to detect electrochemically active oxygen states.

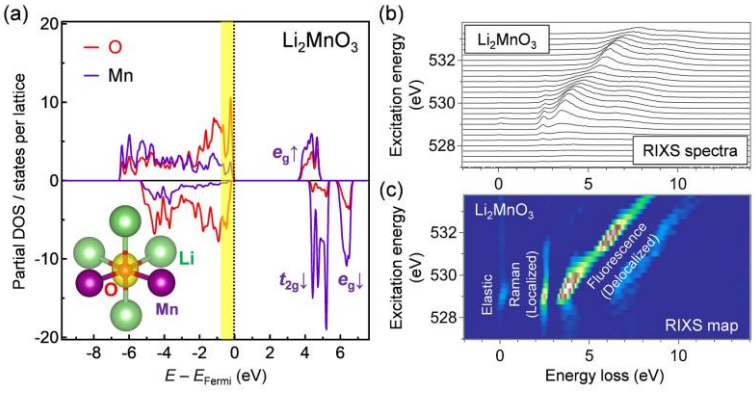

Figure 2. Direct observation of orphaned oxygen 2*p* orbitals in Li_2MnO_3. (a) Calculated partial density of states for oxygen and manganese in Li_2MnO_3. The inset shows the spatial electron density at the energy range from −0.9 to 0 eV versus the Fermi energy. (b) Oxygen *K*-edge RIXS spectra, and (c) second differential RIXS map for Li_2MnO_3 with excitation photon energy from 527 to 533.75 eV.

MULTIORBITAL BOND FORMATION FOR STABLE OXYGEN-REDOX REACTION IN BATTERY ELECTRODES

Masashi Okubo
Department of Chemical System Engineering, School of Engineering, The University of Tokyo

High energy density batteries are a long-standing target for sustainability efforts, but the energy density of the state-of-the-art lithium-ion batteries is limited in part owing to the small capacity of positive electrode materials. Although the additional oxygen-redox reaction of Li-excess transition-metal oxides is an attractive approach to increase the capacity, an atomic-level understanding of the reaction mechanism has not been established. Here, using bulk-sensitive resonant inelastic X-ray scattering (RIXS) spectroscopy combined with ab initio computations, we prove the existence of an orphaned oxygen 2*p* orbital that was theoretically predicted to play a key role in oxygen-redox reactions.

As a target Li-excess layered transition metal oxide, $Li_{1.2}Ni_{0.13}Co_{0.13}Mn_{0.54}O_2$ was used as an oxygen-redox electrode material. Before measuring the RIXS spectra, the *ab initio* calculations using the HSE06 hybrid functional were carried out for $Li_{1.2-x}Ni_{0.13}Co_{0.13}Mn_{0.54}O_2$. The calculated electronic structures show that the averaged Bader charges of Ni and Co decrease only during the early stage of Li^+ extraction ($x < 0.4$), whereas that of oxygen continuously decreases during the whole delithiation process, suggesting the occurrence of the additional oxygen-redox reactions for $x > 0.4$. Indeed, $Li_{1.2}Ni_{0.13}Co_{0.13}Mn_{0.54}O_2$ delivers a large capacity of approximately 250 mAh/gexceeding the theoretical capacity (123 mAh/g) of the Ni^{4+}/Ni^{2+} and Co^{4+}/Co^{3+} redox reactions.

The oxygen *K*-edge X-ray absorption spectrum (XAS) in a bulk sensitive partial fluorescence yield mode for the pristine $Li_{1.2}Ni_{0.13}Co_{0.13}Mn_{0.54}O_2$ shows two absorption peaks (528.5 and 531 eV) of 1*s* core-electron excitation to unoccupied σ-type bands (oxygen 2*p*−Mn $e_g^{\downarrow}/e_g^{\uparrow}$, $3a_1^*/3b_2^*$ in C_{2v}) and an unoccupied π-type band (oxygen 2*p*−Mn $t_{2g}^{\downarrow}$, b_1^* in C_{2v}). This band picture agrees with the calculated partial density of states (pDOS) for Mn. Upon charging to 4.4 V vs. Li/Li^+, a new XAS shoulder emerged at 527 eV owing to hole generation in σ-type (oxygen 2*p*−Ni e_g) and π-type (oxygen 2*p*−Co t_{2g}) bands. After oxygen oxidation, a new absorption emerged at a relatively high absorption-energy region of approximately 530.5 eV. Similar spectral changes were also observed during the second cycle. The XAS signal at 530.5 eV can be ascribed to an unoccupied π-type band (oxygen 2*p*−Mn $t_{2g}^{\uparrow}$) resulting from oxygen oxidation. The emergence of the absorption at a relatively high energy region is reasonable because oxygen oxidation increases the effective nuclear charge, which lowers the initial energy level of an oxygen 1*s* core and hence raises the excitation energy[18]. Similar changes in the XAS signals by oxidation (the emergence of new absorption at a high energy region) are often observed for transition-metal *K*-edge absorption spectra.

The RIXS spectra and the second differential RIXS map of pristine $Li_{1.2}Ni_{0.13}Co_{0.13}Mn_{0.54}O_2$ (Fig. 1) exhibit a Raman-like peak with constant energy loss corresponding to a π-type narrow oxygen 2*p* band ($\pi \rightarrow \pi^*$), in addition to the fluorescence-like peaks ($\sigma \rightarrow \sigma^*$). The *ab initio* calculations for pristine $Li_{1.2}Ni_{0.13}Co_{0.13}Mn_{0.54}O_2$ supports the existence of the localized oxygen 2*p* orbitals along the Li−O−Li axes with an orbital energy near the Fermi level. The $\pi \rightarrow \pi^*$ RIXS peak intensified after charging to 4.4 V vs. Li/Li^+ (transition-metal oxidation, Fig. 1b), which indicates accumulation of the localized oxygen 2*p* states to the Fermi level. The initial Li^+ extraction associated with Co and Ni oxidation gives an oxygen coordination environment with a □−O−Li^+ or □−O−□ axis (□: Li^+ vacancy), which electrostatically raises the energy level of the localized oxygen 2*p* orbitals. Indeed, the fact that the energy loss of the Raman-like RIXS peak decreased from 2.5 to 2.0 eV supports the rise in the energy level of the localized oxygen 2*p* orbitals. We presume that the accumulation of the localized oxygen 2*p* states to the Fermi level should be an essential

preceding process to trigger the oxygen-redox reactions. For example, it is well known that the electrochemical properties of Li_2MnO_3 is poor even though oxygen has a Li^+–O–Li^+ axis and hence a localized oxygen 2*p* orbital. Most likely, as Li_2MnO_3 cannot exhibit the initial Li^+ extraction owing to the electrochemically inactive Mn^{4+}, it is difficult to generate the □–O–Li^+ and □–O–□ axes, and the energy level of the localized oxygen 2*p* orbital remains too low to undergo oxidation within the electrolyte stability window. Conversely, when redox-active transition metals are present, such as in Li_2MnO_3-Li*M*O_2 solid solution, the □–O–Li^+ and □–O–□ axes are easily formed by the initial Li^+ extraction to raise the energy level of the localized oxygen 2*p* orbital, unlocking the redox activity of oxygen. Once the oxygen-redox reaction is triggered, the □–O–Li^+ and □–O–□ axes are continuously generated to achieve a large oxygen-redox capacity.

After charging to 4.8 V vs. Li/Li^+ (oxygen oxidation, Fig. 1c), the Raman-like $\pi \rightarrow \pi^*$ RIXS peaks disappear, and all the RIXS peaks become fluorescence-like. Importantly, a new intense fluorescence-like peak emerges at an energy loss of approximately 7.0 eV with an incident photon energy of 530.5 eV. Recalling that an incident photon of 530.5 eV excited 1*s* core electron to an unoccupied π-type band (oxygen 2*p*–Mn $t_{2g}^{\uparrow}$), the inelastic scattering resonance with the 530.5 eV incident photon includes the valence excitation between the π-type bands ($\pi \rightarrow \pi^*$). Therefore, a large energy loss of approximately 7 eV for this RIXS peak corresponds to π-type splitting. This large π-type splitting should be induced by the hole generation in the antibonding π-type band, and makes the Mn–O bonds more bonding (more delocalized). Therefore, the RIXS peak is observed as fluorescence-like. The enhanced π-type interaction stabilizes the oxidized oxygen, leading to reversible oxygen-redox reactions. Indeed, the Raman-like RIXS peak of the localized oxygen 2*p* orbitals was recovered after full discharge (Fig. 1d), and the changes in the RIXS spectra were reversible even during the subsequent cycle.

To summarize the reaction mechanism, the Li^+–O–Li^+ coordination in the pristine state forms localized oxygen 2*p* orbital weakly hybridized with the Mn t_{2g} orbital. When the initial Li^+ extraction occurs in association with *M* redox reactions, the □–O–Li^+ and □–O–□ coordination axes are generated, which raises the energy level of the localized oxygen 2*p* states to the Fermi level. After this accumulation, oxygen oxidation occurs to delocalize the hole within a Mn–O–Mn bond. The resulting large b_1/b_1^* splitting stabilizes the oxidized oxygen, enabling a reversible oxygen-redox reaction.

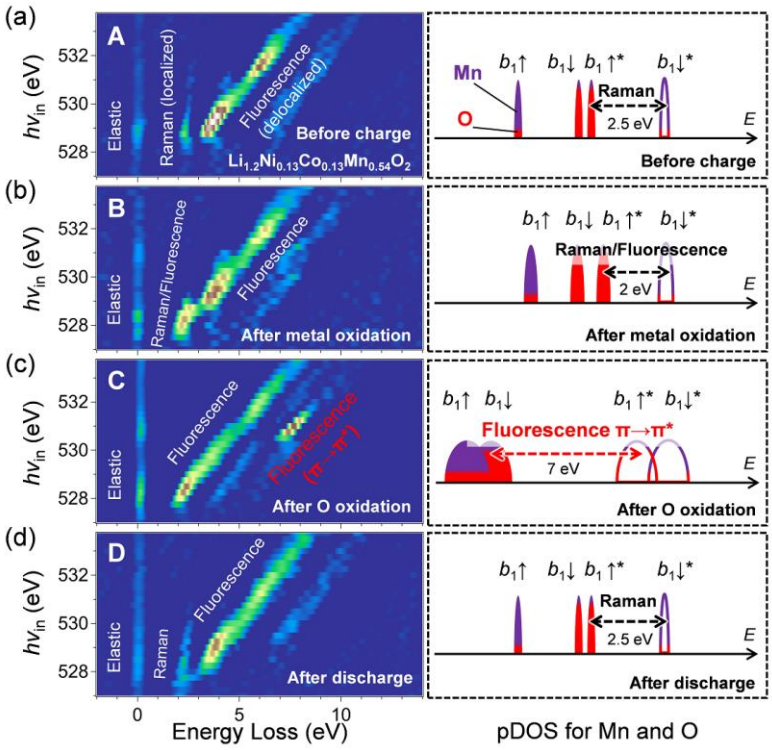

Figure 1. Monitoring oxygen 2*p* orbitals during oxygen-redox reaction of $Li_{1.2}Ni_{0.13}Co_{0.13}Mn_{0.54}O_2$. Oxygen *K*-edge second differential RIXS map for the samples (a) before charge, (b) after transition-metal oxidation, (c) after oxygen oxidation, and (d) after discharge, with excitation photon energy from 527 to 533.75 eV. The schematic partial density of states (pDOS) for Mn 3*d* and oxygen 2*p* orbitals are shown for comparison.

UNDERSTANDING OF SOLVATION AND DESOLVATION STATE OF ACTIVE MATERIALS FOR REDOX-FLOW BATTERIES DERIVED FROM HYDROGEN-BONDING ANALYSIS BY SOFT X-RAY SPECTROSCOPY

Akihiro Ohira[1], Eiji Hosono[1,2,3], Daisuke Asakura[1,3], Takashi Funaki[1], Kosuke Yamazoe[4], Jun Miyawaki[4,5], Yoshihisa Harada[4,5]

[1]Research Institute for Energy Conservation, National Institute of Advanced Industrial Science and Technology (AIST), [2]Department of Energy and Environment, Global Zero Emission Research Center, AIST, [3]AIST-UTokyo Advanced Operando-Measurement Technology Open Innovation Laboratory (OPERANDO-OIL), [4]Synchrotron Radiation Laboratory, The Institute for Solid State Physics, The University of Tokyo [5]Synchrotron Radiation Research Organization, The University of Tokyo

Power generation systems that use natural energy, such as sunlight and wind, and that do not generate greenhouse gases have been actively introduced globally. Although they do not generate carbon dioxide, compared to power sources like thermal and hydroelectric power, these renewable energy sources provide an unstable power supply that is affected by various situations. In order to use renewable energy efficiently and smoothly, the generated electricity must be stored and discharged as required; thus, a storage battery (secondary battery) that can adjust the constantly fluctuating output over short and long cycles is significantly desired. Large scale storage batteries are famous for lithium ion batteries, sodium-sulfur batteries, lead storage batteries and redox flow batteries.[1-3] Lead storage batteries have been used as batteries for automobiles and motorcycles for a long time and have abundant achievements as small storage batteries. Lithium ion batteries also have many achievements as small batteries. Sodium-sulfur batteries have an extremely high energy density and are widely used in load leveling applications in substations due to their high charge and discharge efficiency.

Redox flow batteries (RFBs) have been successfully developed by NASA around 1974.[4] At the beginning of development, the Fe/Cr system was mainstream,[5] but it was not put into practical use due to the disadvantage that mixing of the positive/negative electrolyte through the membrane leads to a decrease in capacity of the battery. In around 1984, Kazacos et al. has developed a vanadium-based RFB (VRFB).[6] Since that time, the awareness of RFBs have increased and research and development has been accelerating.

The significant issue in studying RFBs is to correctly evaluate the reactivity of electrodes and active materials in addition to newly active material search and clarify material properties necessary for improving battery performance.

In addition to the search for new active materials, it is important to precisely understand the reactivity of the electrodes and active materials. In particular, the state of solvation and desolvation associated with the electrochemical reaction between active material and solvent has not been well-understood at all, and a detailed understanding of the dynamics of solvation/desolvation at the interface between the active material and the electrode is required. This will lead to a dramatic increase in solubility and redox activity, which will lead to the realization of high-performance RFBs. In this study, to obtain a guideline for the design of the interface between the active material and the electrode, which is indispensable for the realization of a high-performance RFB, the hydration state of water-soluble active materials was investigated by X-ray absorption and emission spectroscopy.

A dendrimer molecule with a viologen unit [7] dissolved in methanol was cast on the SiN window and after drying the membrane, the cell was assembled and mounted in a chamber. Water vapor was introduced while bubbling with nitrogen gas to control the relative humidity in the cell. We observed changes in the O1s soft x-ray emission spectra of oxygen upon hydration and dehydration of the dendrimer molecules.

Figure 1 shows the change in the O1s XES spectrum of water in dendrimer molecules during the hydration and dehydration processes. With increasing humidity, emission spectra similar to those of bulk water were obtained. In addition, in the spectrum of the dehydration process (the change from wet to dry state indicated by the sign Re), 1b' is relatively small, and the change is not reversible when comparing the each spectra of the hydration and dehydration processes. To irreversible change in the spectra, optical microscopy observations of the cast films before and after the measurements were performed. Since the film disappeared in the area irradiated by X-rays, it is inferred that the film was dissolved during the hydration process.

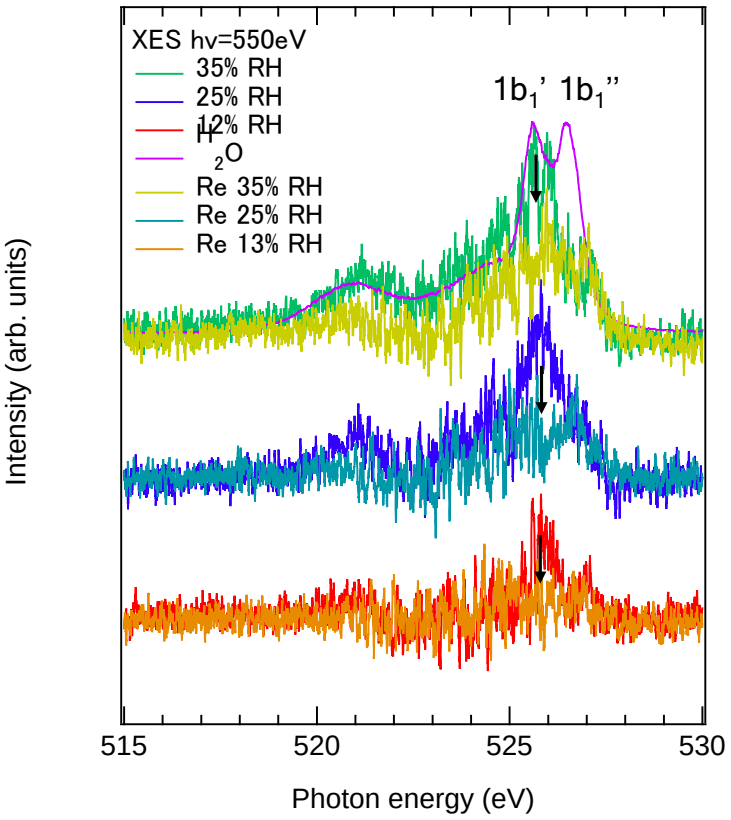

Figure 1 Change in the O1s XES spectrum of water in dendrimer molecules under humidity control.

In the future, we plan to immobilize the molecules on the substrate to check the changes in hydration and dehydration.

REFERENCES

[1] B. Zakeri. S. Syri, Renewable and Sustainable Energy Reviews, **42**, 569 (2015).
[2] F. Shi, Reactor and Process Design in Sustainable Energy Technology, Elsevier Amsterdam (2016).
[3] B. Dunn, H. Kamath, J.-M. Tarascon, Science, **334**, 928 (2011).
[4] L. H. Theller, NASA TM X-71540, 1 (1974).
[5] R. F. Gahn, N. Hagedorn, NASA Tech Briefs February, 42 (1987).
[6] M. S. Kazacos, M. Rychcik, R. G. Robin, A. G. Fane, J. Electrochem. Soc., **133**, 1057 (1986).
[7] A. Ohira, T. Funaki et al. ACS Appl. Energy Mater., **3**, 4377 (2020)

PHOTOEXCITED CARRIER DYNAMICS IN LEAD SULFIDE QUANTUM DOT PHOTOVOLTAIC CELL

Kenichi Ozawa [a,b], Susumu Yamamoto [c], Iwao Matsuda [d]

[a] *Department of Chemistry, Tokyo Institute of Technology,* [b] *Institute of Materials Structure Science, High Energy Accelerator Research Organization,* [c] *Institute of Multidisciplinary Research for Advanced Materials, Tohoku University,* [d] *The Institute for Solid State Physics, The University of Tokyo*

INTRODUCTION

For realizing a sustainable society, uses of solar energy are essential. Photovoltaic (PV) devices are one of solutions to utilize the solar energy. It has been recognized that there is the Shockley-Queisser limit, which is the theoretical maximum light-electricity conversion efficiency of a PV cell using a single p/n junction. The limit is 34% at a band gap of 1.34 eV [1]. One of techniques to exceed this limit is tandemaization of multiple p/n junctions composed of different materials to cover several photon energies. Another solution is the use of quantum dots (QDs) in a light-receiving layer. The QDs allow to absorb lights of various wavelengths owing to the formation of quantum-well states. One of advantages of the QD PV cells is that the absorption band can be controlled simply by changing the QD size so that the production cost can be kept low in comparison with the multijunction PV cells.

Preceding studies on the QD PV cells have mainly focused on synthesis methods of various kinds of QDs as well as their optical properties. On the other hand, accumulation of knowledge of photoexcited carrier dynamics in the QD PV cells is still insufficient. In the present study, therefore, we shed the light on the dynamics of carriers generated in the QDs by using time-resolved soft X-ray photoelectron spectroscopy (TRXPS). TRXPS has been proved to be a powerful tool to clarify the carrier dynamics in model organic PV cells [2, 3].

EXPERIMENTAL

The QDs employed in this work were lead sulfide (PbS) nanoparticles with average sizes of 3 and 9 nm (Quantum Solutions). PbS QD films were prepared under ambient conditions by spin-coating the PbS QD solutions on 0.05 and 0.5 wt% Nb-doped rutile TiO_2(110) substrates. Since PbS and TiO_2 are p-type and n-type semiconductors, respectively, a p/n junction is realized at the PbS/TiO_2 interface. The prepared QD films were treated with 3-mercaptopropionic acid (3-MPA) by dropping a 3-MPA solution onto the films and then by removing the solution. This procedure allowed to replace a capping layer of the PbS QD from original oleic acid to 3-MPA.

The TRXPS measurements were carried out at BL07LSU of SPring-8 in the H operation mode [4]. Visible (807 nm) and ultraviolet (404 nm) lasers with a repetition rate of 208 kHz were used to generate the photoexcited carriers in the PbS QD films, and the excited states were monitored through synchrotron-radiation excited Pb 4f and S 2p peaks of PbS and Ti 2p peak of TiO_2.

RESULTS AND DISCUSSION

Fig. 1 shows S 2p and Pb 4f spectra of the 3-nm PbS QD film. Four peaks are observed in the S 2p spectrum; two of them originate from the spin-orbit splitting S 2p levels of the S atoms in the PbS QD

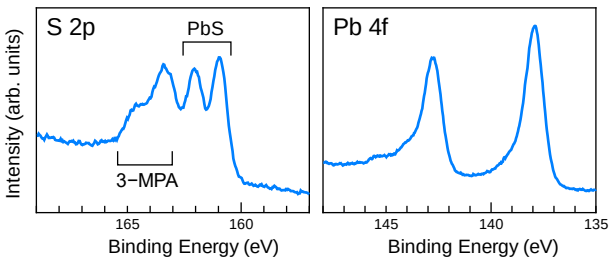

FIGURE 1. S 2p and Pb 4f core-level peaks of the 3-nm PbS QD film on TiO_2(110). The photon energy was 370 eV.

film, and the other two arise from 3-MPA. The lower and higher binding-energy components are associated with PbS and 3-MPA, respectively. This assignment is rationalized because (1) the PbS/3-MPA intensity ratio is higher in the film composed of the 9-nm QDs than the 3-nm QDs and (2) the low binding-energy component is transiently shifted upon laser pulse irradiation (this will be described below). The Pb $4f_{7/2}$ and $4f_{5/2}$ peaks have a tailing towards higher binding energies (Fig. 1). This suggest an existence of oxidation species such as PbO. Although the PbS QD films were prepared and treated under ambient conditions, oxidation of the PbS QD is limited because of a relatively low intensity of the tail structure.

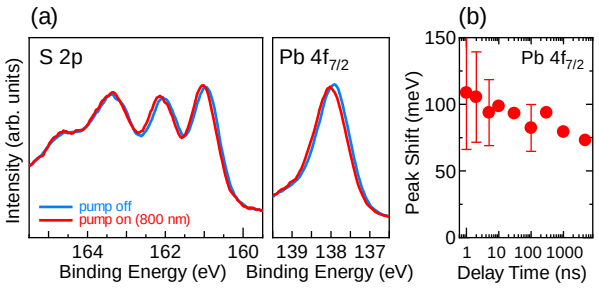

FIGURE 2. (a) Comparison of the S 2p and Pb $4f_{7/2}$ peaks of 3-nm PbS QD with and without 800-nm laser pulse irradiation. The photon energy was 370 eV. The spectra with laser irradiation were acquired at a delay time of 1 ns. (b) Change in the magnitude of the Pb $4f_{7/2}$ peak shift as a function of a delay time.

As the PbS QD films are irradiated by either visible or ultraviolet laser, the PbS-originated peaks move to the higher binding energies. Fig. 2a compares the S 2p and Pb $4f_{7/2}$ spectra of the 3-nm PbS QD film acquired with and without the visible laser (807 nm = 1.54 eV). Except for the S 2p component of 3-MPA, all peaks move by ~100 meV upon laser irradiation. The direction of the peak shift can be interpreted by a loss of an excited electron in the PbS QD by charge transfer from PbS to TiO_2.

Fig. 2b shows that the magnitude of the laser-induced shift of the PbS peaks diminishes with a delay time. This suggests that electron-hole recombination should proceed with time if the magnitude of the shift is proportional to the number of the PbS cations. It is apparent that the decay curve can be reproduced neither by a biexponential function nor by a triexponential function. This is in contrast to decay curves obtained from model organic PV cells [2], where the curves are reproduced by a biexponential function. A gradual decrease of the peak shift in the present case implies that there should be several PbS cations with different lifetimes. A certain distribution of the QD size, though the average size is 3 nm in the case of Fig. 2b, may be responsible for a wide range of the lifetime.

A point to be noted is that the peak shift remains even after 4.8 μs, the longest delay time examined in the present study. A long lifetime of the excited state of PbS, i.e., the cationic state of PbS, is one of advantages for the efficient light-electricity conversion because there is an enough time for the free electrons and holes to be transported to the electrodes before they are quenched via electron-hole recombination. Thus, the PbS QD/TiO_2 system can be a good candidate for a PV cell with high efficiency.

ACKNOWLEDGEMENT

The TRXPS study was conducted using the facilities of the Synchrotron Radiation Research Organization, The University of Tokyo (Proposal No. 2019B7460). A financial support from MEXT, Japan (KAKENHI 16H06027) is appreciated.

REFERENCES

[1] S. Rühle, Sol. Energy **130**, 139−147 (2016).
[2] K. Ozawa *et al.*, J. Phys. Chem. C **123**, 4388−4395 (2019).
[3] F. Roth *et al.*, Phys. Rev. B 99, 020303(R) (2019).
[4] S. Yamamoto *et al.*, J. Synchrotron Radiat. **21**, 352−365 (2014).

Photo-induced valence transition dynamics of SmS studied by time-resolved x-ray absorption spectroscopy

H. Watanabe[A], T. Nakamura[A], Y. Shibata[A], K. Yamagami[B], Y. Hirata[C], K. Ikeda[B], Y. Zhang[D], H. Wadati[D], K. Imura[E], H. S. Suzuki[B], N. K. Sato[E], S. Kimura[A]

[A]*Osaka University*, [B]*ISSP. The University of Tokyo*, [C]*National Defense Academy*, [D]*University of Hyogo*, [E]*Nagoya University*

Samarium monosulfide (SmS) is known to show a phase transition (namely BG transition) from a black insulator phase to a valence-fluctuating golden metal phase by applying pressure and/or elemental substitution (yttrium doping) [1]. Although the research has a long history for about 50 years, the origin of the BG transition has not been revealed yet. One possibility of the origin is due to an instability of excitonic states, namely excitonic instability [2]. If so, when the exciton states are produced by photo-irradiation, a phase transition like the BG transition is supposed to occur. So far, we have reported the existence of a metastable state of yttrium-doped SmS accompanied by high carrier density by photo-irradiation [3]. However, it has not been revealed that the metastable state is related to the valence transition. In this study, to clarify the valence change of Sm ions by photo-irradiation, we measured the temporal structure of the Sm $3d_{5/2}$ XAS after the photo-irradiation.

The time-resolved pump-probe XAS experiment was performed at BL07LSU of SPring-8 using the H mode (11/29-filling + 1-bunch). The Sm $3d_{5/2}$ core level absorption peak at about 1080 eV was used to evaluate the ratio between Sm^{2+} and Sm^{3+} ions. A Ti:sapphire laser (pulse width: 50 fs, photon energy: 1.55 eV, reputation rate: 1 kHz) synchronized with the synchrotron radiation x-ray (pulse width: 50 ps) was used as the pump light.

Figure 1 shows the time evolution of the signal intensity of 1077 eV (Sm^{2+} $3d_{5/2}$ core level) before and after the one-laser-pulse irradiation at 0 ps, but no significant change was observed after the photo-irradiation. The same result was obtained at the Sm^{3+} $3d_{5/2}$ peak at 1080 eV. These suggest that the spectral change due to the one-pulse irradiation was less than the experimental accuracy of about 1 % estimated from the variation in strength before the pump pulse irradiation (t < 0 ps) as shown in Fig. 1. According to our time-resolved reflectance measurements, a 20-% change of the reflectivity was observed just after the photo-irradiation, but the change was relaxed to less than 1 % within 1 ps. Therefore, no spectral change in the

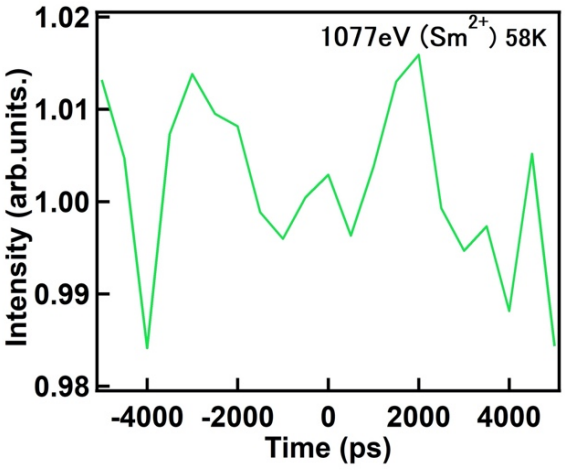

Fig. 1. Time development of the peak intensity at 1077 eV before and after photo-irradiation at the time of 0 ps.

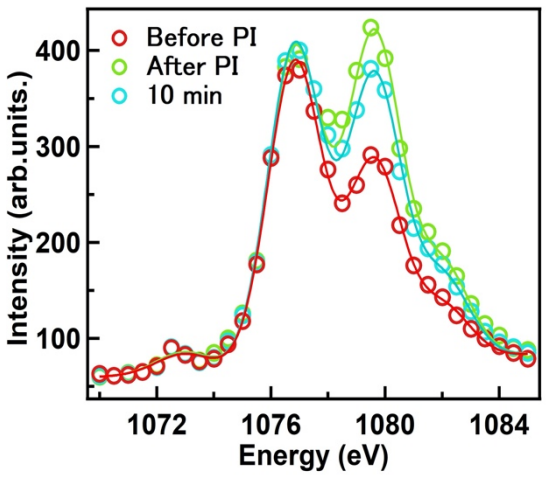

Fig. 2. XAS spectra of the Sm $3d_{5/2}$ core level before (red), just after (green) and 10 minutes after (blue) the photo-irradiation (PI). The spectra were normalized by the peak intensity at 1077 eV.

XAS result by one laser pulse is consistent with our previous time-resolved reflectance measurement.

Next, the time evolution of the Sm $3d_{5/2}$ XAS spectrum after many light pulses irradiation was measured. Figure 2 shows the Sm $3d_{5/2}$ core absorption spectra before (red), immediately after (green) and 10 minutes after (blue) the photo-irradiation for 1 hour at a temperature of 58 K. The absorption shape obviously changes by time suggesting the temporal change of the mean valence. Also, combined with no temporal change by one pulse excitation, the valence change by one pulse is too small to be observed and it is pilled up by many pulses because it does not relax completely before the next pulse after 1 ms.

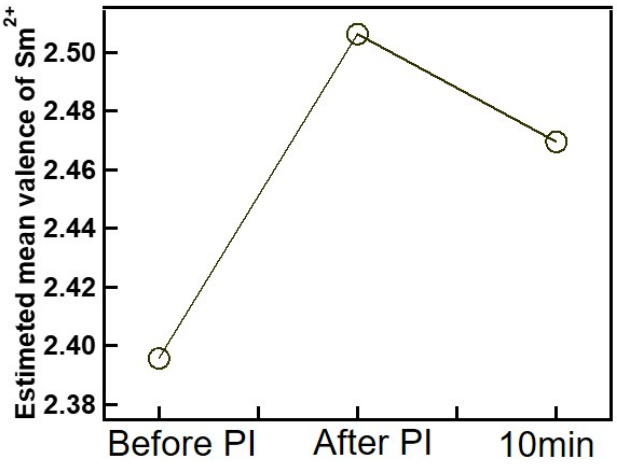

Fig. 3. Time evolution of the mean valence before and after one-hour laser pulse irradiation (PI). The mean valence is obtained by the ratio between the 1077-eV and 1080-eV peaks.

Before the photo-irradiation, not only the peak at 1077 eV (mainly originating from a Sm^{2+} component) but also the peak at 1080 eV (mainly from Sm^{3+}) was observed suggesting the intermediate valence of Sm ions. From Figure 2, combined with core level calculations, the mean valence can be roughly evaluated from the ratio of peak intensity at 1077 eV and 1080 eV as shown in Fig. 3. The mean valence before the photo-irradiation was evaluated as 2.40. Just after the photo-irradiation shown by blue circles, the intensity of the Sm^{3+} peak increased compared to that of Sm^{2+} suggesting the mean valence of Sm increased to 2.51 by many laser pulses. After 10 minutes, the mean valence of Sm decreased to 2.47, but the mean valence does not come back to the original value even after 1 hour. The origin of the remained higher valence cannot be explained by a very long relaxation time because surface oxidation also makes a valence change from Sm^{2+} to Sm^{3+}. However, since the decrease of the mean valence after 10 min is the opposite change to the oxidation, it suggests the relaxation from Sm^{3+} to Sm^{2+} without photo-irradiation. This implies that the photo-excited Sm^{3+} intermediate state decays to the Sm^{2+} ground state by a very long relaxation time for several 10 min. The detailed relaxation dynamics is reported in a separate report [4].

REFERENCES

[1] K. Matsubayashi *et al.*, J. Phys. Soc. Jpn. **76**, 064601 (2007).
[2] T. Mizuno *et al.*, J. Phys. Soc. Jpn. **77**, 113704 (2008).
[3] R. Ikeda *et al.*, J. Phys.: Conf. Ser. **1220**, 012005 (2019).
[4] H. Watanabe et al., ACTIVITY REPORT OF SYNCHROTRON RADIATION LABORATORY 2019, ISSP, The University of Tokyo.

Relaxation dynamics of Photo-induced valence transition of SmS studied by time-resolved x-ray absorption spectroscopy

H. Watanabe[A], T. Nakamura[A], Y. Shibata[A], K. Yamagami[B], Y. Hirata[C], K. Ikeda[B], Y. Zhang[D], H. Wadati[D], K. Imura[E], H. S. Suzuki[B], N. K. Sato[E], S. Kimura[A]

[A]*Osaka University,* [B]*ISSP. The University of Tokyo,* [C]*National Defense Academy,* [D]*University of Hyogo,* [E]*Nagoya University*

Samarium monosulfide (SmS) is known to show a phase transition (BG transition) from a black insulator phase to a valence-fluctuating golden metal phase by applying pressure and/or elemental substitution (yttrium doping) [1]. We have reported the existence of a metastable state of yttrium-doped SmS accompanied with high carrier density by photo-irradiation [2] and the valence transition from Sm^{2+} to Sm^{3+} could be occurred by photo-irradiation at 58 K by the time-resolved x-ray absorption spectroscopy (trXAS) [3]. In the trXAS, the valence change of Sm could not be observed by one-pulse excitation, but after the many pulse irradiation, the valence finally changes from 2.40 to 2.51. This suggests that the photo-excited metastable state has a very longer life-time than the interval of the pump pulse (1 ms) and it is piled up by the multi-pulse excitation, and finally, the photo-excited state could be observed. The origin of the metastable state is related to the pressure-induced BG transition and recently observed non-linear conduction phenomena of black-SmS [4].

The origin of the metastable state, as well as the valence transition by the photo-irradiation, has not been clarified yet. One possibility is the BCS-to-BEC transition of the photo-excited exciton state, namely "excitonium" [5]. The excitonium is expected to have carriers, so the other experiment to detect the time-dependence of carrier density, band structure, and lattice constants must be combined with trXAS. In this study, to evaluate the lifetime of the photo-excited state, we measured the relaxation dynamics after multi-pulse excitation.

The time-resolved pump-probe XAS experiment was performed at BL07LSU of SPring-8 using the H mode (11/29-filling + 1-bunch). The Sm $3d_{5/2}$ core level absorption peak at about 1080 eV was used to evaluate the ratio between Sm^{2+} and Sm^{3+} ions. A Ti:sapphire laser (pulse width: 50 fs, photon energy: 1.55 eV, reputation rate: 1 kHz) synchronized with the synchrotron radiation x-ray (pulse width: 50 ps) was used as the pump light.

Figure 1 shows the temporal structure of the 1080-eV peak after the 5-min (about 300,000 laser pulse) laser irradiation. The valence of the photo-excited state has been evaluated as about 2.5 [3], which is smaller than that of the golden phase (2.6-2.7) induced by pressure [6]. So, the consistency between the photo-excited state and the golden phase is still unclear but it is obviously different from that of the divalent black phase. The photo-excited state might be a new

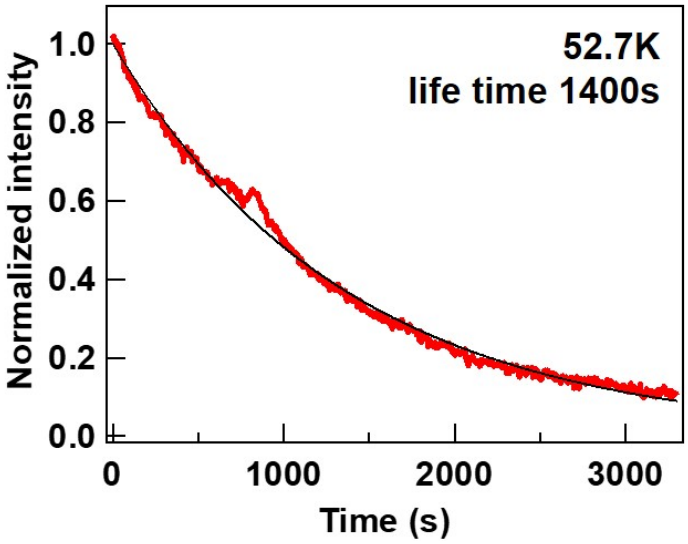

Fig. 1. Temporal structure of the 1080-eV peak at 52.7 K. The time dependence can be fitted by an exponential decay curve with a lifetime of 1400 s.

intermediate state. The decay curve can be fitted by an exponential relaxation with ~~the~~ a lifetime of 1400 s (about 23 min), i.e., the photo-excited intermediate state has a very long time. To clarify the origin of the photo-excited state, a further trXAS and other time-resolved experiments are needed.

REFERENCES

[1] K. Matsubayashi *et al.*, J. Phys. Soc. Jpn. **76**, 064601 (2007).
[2] R. Ikeda *et al.*, J. Phys.: Conf. Ser. **1220**, 012005 (2019).
[3] H.Watanabe *et al.*, ACTIVITY REPORT OF SYNCHROTRON RADIATION LABORATORY 2019, ISSP, The University of Tokyo.
[4] H. Ando *et al.*, JPS Conf. Proc. **30**, 011132 (2020).
[5] B. I. Halperin and T. M. Rice, Rev. Mod. Phys. **40**, 755 (1968).
[6] K. Imura *et al.*, JPS Conf. Proc. **30**, 011131 (2020).

LOW-TEMPERATURE METHANE OXIDATIVE COUPLING ON MODIFIED PD MODEL CATALYSTS STUDIED BY *OPERANDO* AMBIENT-PRESSURE XPS

Takanori Koitaya,[†] Susumu Yamamoto,[‡] Iwao Matsuda,[‡] Jun Yoshinobu[‡] and Toshihiko Yokoyama[†]

[†] *Department of Materials Molecular Science, Institute for Molecular Science*

[‡]*The Institute for Solid State Physics, The University of Tokyo*

Direct observation of heterogeneous catalysts under operation condition is important for understanding reaction mechanism and nature of active sites on the catalysts. Various *operando* methods have been developed to investigate surface chemistry on heterogeneous catalysts. We have investigated reactions of inert molecules, such as carbon dioxide and methane, using an ambient-pressure XPS (AP-XPS) system at SPring-8 soft X-ray beam line BL07LSU [1, 2]. The XPS measurements can be currently performed in the presence of reactant gases up to 2000 Pa using synchrotron radiation or a conventional X-ray source. In the gas environment, the sample can be heated up to around 900 K to investigate thermal reaction on the surface of catalysts.

In this study, oxidation of methane on the Pd(110) surface was studied by AP-XPS and QMS. Fig. 1 shows QMS spectra of reaction products and sample temperature of the Pd(110) surface in the presence of 2.0 mbar oxygen and 5.6 mbar methane. As shown in Fig. 1, reactivity of the Pd(110) sample was very low, when the sample was heating from room temperature to 615 K in the presence of the feed gases. However, the amount of the products increased significantly after heating to 780 K.

Chemical states of the surface during the reaction were investigated by operando AP-XPS. Fig. 2 shows AP-XPS spectra measured at sample temperature of 615 K. Before heating to 780 K, the surface of the sample was oxidized, and PdO thin film was formed as indicated by Pd 3d and O 1s spectra. In addition, peaks of adsorbed species were observed in O 1s and C 1s, which can be attributed to oxidized carbon species (COx). Since the surface before heating to 780 K is less reactive, the observed adsorbate is not an important reaction intermediate, but a spectator or poisoning species. After the activation process, Pd 3d and O 1s spectra shows that the sample was still (partially) oxidized. In O 1s and C 1s spectra, gas-phase peaks of the produced species (water and CO_2) were observed, indicating that this surface is much more reactive. Note that the adsorbed COx was not observed after the activation process. This indicates that coverage of the intermediates is negligible during the methane oxidation reaction. Therefore, the rate-limiting step for the methane oxidation is dissociative adsorption of methane. Once the formation of CH_3 species occurs, following reactions, including desorption of products, proceed at much faster rates compared to the initial methane dissociation.

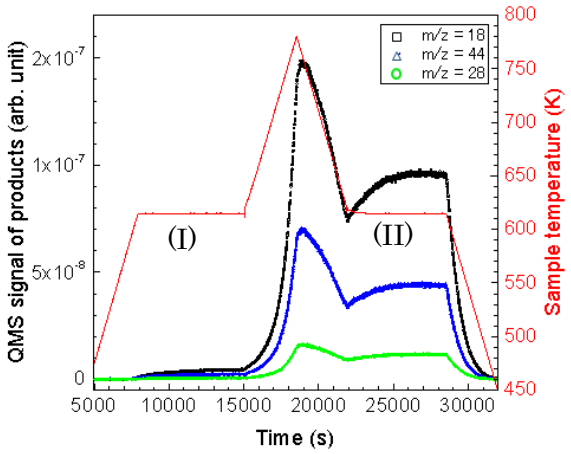

Figure 1. QMS spectra of oxidation products (water, CO, CO_2) on the Pd(110) surface in the presence of 2.0 mbar oxygen and 5.6 mbar methane. Sample temperature is also shown in the figures.

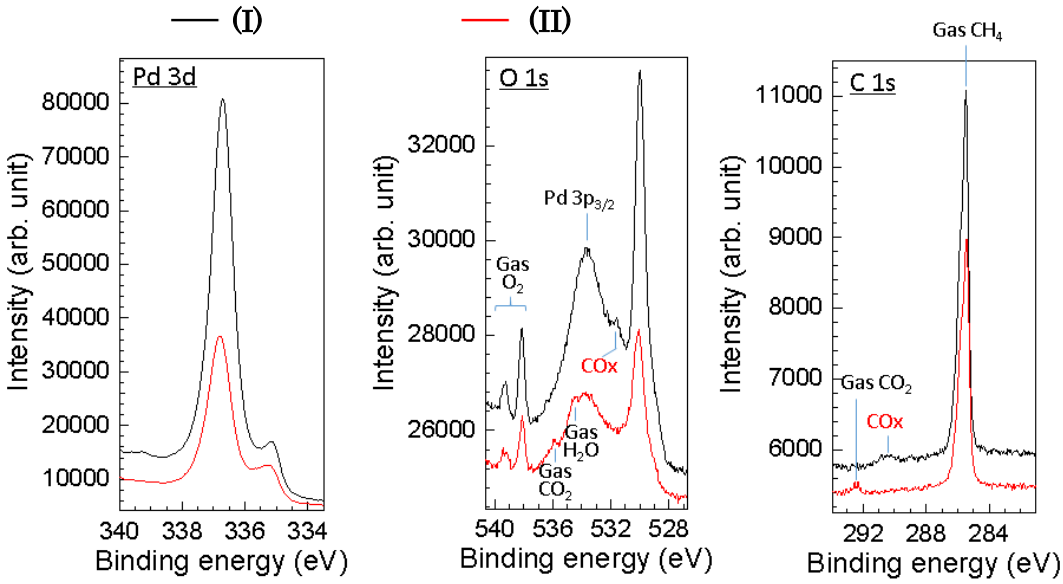

Figure 2. AP-XPS spectra measured at region (I) and (II) indicated in Fig. 1. During the measurement, the Pd(110) sample was kept at 615 K in the presence of 2.0 mbar oxygen and 5.6 mbar methane gases.

REFERENCES

[1] Koitaya, T. et al., Top. Catal. **59**, 526-531 (2016).
[2] Koitaya, T. et al., e-J. Surf. Sci. Nanotech. **17**, 169-178 (2019).

X-ray Spectral Imaging Analysis of Interface States at p^+-WSe_2/n-MoS_2 Hetero Junctions in TFET Device Structure

Naoka Nagamura[1,2], Keigo Nakamura[3], Hayami Kawamoto[3], Naoki Higashitarumi[3], Keishi Akada[4], and Kosuke Nagashio[3]

[1]*National Institute for Materials Science (NIMS), Tsukuba, Ibaraki, Japan.*
[2]*PRESTO, Japan Science and Technology Agency, Honcho, Saitama, Japan.*
[3]*Department of Materials Engineering, The University of Tokyo, Hongo, Tokyo, Japan.*
[4]*Institute for Solid State Physics, The University of Tokyo, Kashiwa, Chiba, Japan.*

Reducing power consumption in semiconductor devices is an imminent challenge, but the present field effect transistors (FETs) require at least 60 mV of gate voltage to increase the current by one order of magnitude at room temperature. Tunnel FETs can overcome this limitation because of the band-to-band tunnelling (BTBT).

Two-dimensional materials are promising for TFETs. Recently, using p^+-WSe_2 source doped by charge transfer from a WO_x surface oxide layer, we succeeded in observing a clear BTBT in the stable TFET system of p^+-WSe_2/n-MoS_2[1].

In this study, we systematically study the local band alignment in the p^+-WSe_2/MoS_2 TFET device structure as shown in Fig. 1 by scanning photoelectron emission microscopic (SPEM) measurements using a three-dimensional nanoscale electron- spectroscopy chemical analysis (3D nano-ESCA) system installed at BL07LSU of SPring-8.

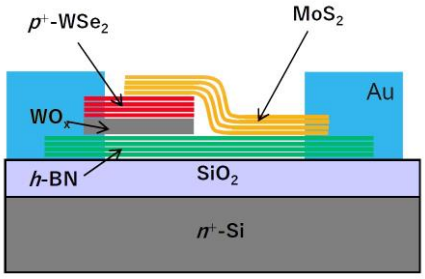

Fig. 1 Schematic image of a p^+-WSe_2/MoS_2 TFET device structure

2D materials used in the sample are fabricated by exfoliation of bulk crystals. WO_x side of WSe_2 film is transferred onto h-BN on a SiO_2/n^+-Si substrate after forming WSe_2/WO_x by O_3 annealing. Then, the p^+-WSe_2/MoS_2 heterostructures were fabricated via dry transfer method using PDMS under the alignment system. Ni/Au was deposited as source/drain electrodes by EB lithography.

Figure 2a shows an intensity mapping image for the Mo 3d 5/2 peak for the 3L-n-MoS_2/p^+-WSe_2 heterostructure on h-BN. The position of the heterostructure is clearly identified. Figure 2b shows the pinpoint core-level spectra for W 4f 5/2 and 4f 7/2 peaks recorded at points of (i) p^+-WSe_2/h-BN and (ii) 3L-n-MoS_2/p^+-WSe_2/h-BN. W 4f peaks for (ii) p^+-WSe_2 in contact with 3L-n-MoS_2 shifts to the higher binding energy side than that for (i) p^+-WSe_2 directly on h-BN. When p^+-WSe_2 is doped with electron, E_F in p^+-WSe_2 increases, resulting in the higher binding energy of W 4f peaks. Therefore, this data supports the p-doping reduction in WSe_2[2]. The mapping of the E_F modulation in p^+-WSe_2 by the top gate is obtained by high-throughput peak fitting analysis using machine learning techniques[3].

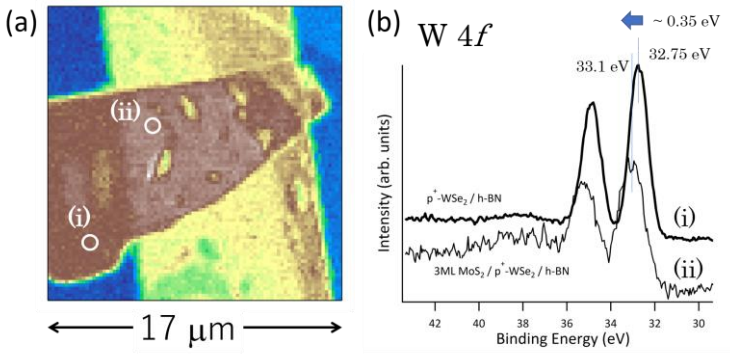

Fig. 2 (a) Photoelectron intensity mapping image for the Mo 3d 5/2 peak for the 3L-n-MoS_2/p^+-WSe_2 heterostructure on h-BN. (b) Pinpoint core-level spectra for W 4f 5/2 and 4f 7/2 peaks recorded at points (i) and (ii).

We also worked on chemical characterization of monolayer tin monosulfide (SnS), a two-dimensional group IV monochalcogenides[4]. The special distribution of different phases, SnS, Sn_2S_3, and SnS_2, around the SnS single crystal nanosheet grown by the physical vapor deposition on a mica substrate has been clarified[5].

REFERENCES

[1] J. He *et al*. Adv. Electron. Mater. **4**, 1800207 (2018).
[2] K. Nakamura *et al*., submitted.
[3] T. Matsumura *et al*. Sci. Technol. Adv. Mater. **20**, 733 (2019).
[4] N. Higashitarumi *et al*. Nature Commun. **11**, 2428 (2020).
[5] H. Kawamoto *et al*., submitted.

SOFT X-RAY ADSORPTION AND EMISSION SPECTROSCOPY OF THE INTERMEDIATE WATER IN BIOCOMPATIBLE POLLYMERS

Shin-nosuke Nishimura[1], Keishi Akada[3], Daiki Murakami[1,2], Kosuke Yamazoe[3], Tomoya Ueda[2], Jun Miyawaki[3], Yoshihisa Harada[3], Masaru Tanaka[1,2]

[1]*Institute of Materials Chemistry and Engineering, Kyushu University,*
[2]*Graduate School of Engineering, Kyushu University,*
[3]*Institute for Solid State Physics, The University of Tokyo*

INTRODUCTION

Recently, significant efforts have been applied toward the design of polymer biomaterials which have central roles in regenerative medicine and tissue engineering application. Water definitely exists on an interface between material and biotissue, of which hydration state essentially affects for biocompatibility [1]. Hydrated water around polymer, as represented by poly(2-methoxyethyl acrylate) (PMEA), is classified into three types, non-freezing water (*NFW*), intermediate water (*IW*), free water (*FW*) in ascending order of the intensity of interaction with polymer chain [2]. Among them, the *IW* has a key role on the affinity of polymer with an organism. However, it has not been clarified what it is in a chemical structure of polymer that works on formation of the *IW*. As the first step to systematize relationship between the *IW* and polymer structure, we evaluated a hydration process on the PMEA brush depending on humidity and succeeded to detect the *IW* by soft x-ray absorption/emission spectroscopy (XAS/XES), whereas origin of the *IW* is still unclear [3, 4]. In this study, we designed and prepared the cyclic PMEA and linear poly(ethylene glycol) monomethyl ether (mPEG) brushes to examine effect of a polymer end and polymer species, respectively (Figure 1). The hydration process on these polymer brushes was evaluated by XAS/XES measurement using the same method as our previous reports.

EXPERIMENTAL

We prepared the cyclic PMEA and linear mPEG brushes on gold-coated SiC substrate by grafting-to method using sulfur-gold interaction (Figure 1). Thiol-terminated PMEA at both end was synthesized *via* reversible addition-fragmentation chain transfer (RAFT) polymerization and subsequent aminolysis. The obtained polymer was treated with iron(III) chloride under high-diluted condition, resulting in an objective cyclic PMEA. The number average molecular weight (M_n) and polydispersity index ($Đ$) of cyclic PMEA were estimated to be 76000 g mol^{-1} and 1.06 from size exclusion chromatography measurement, respectively. A commercially available product was used for thiol-terminated mPEG (M_n = 10000 g mol^{-1}, $Đ$ = 1.13). The gold-cated SiC substrates were soaked in methanol solutions of these polymers. The substrates were washed with methanol and dried *in vacuo* to give objective polymer brushes. Grafting density of the cyclic PMEA and linear was determined to be 0.048 and 0.11 chains nm^{-2} by quartz crystal microbalance measurement, respectively.

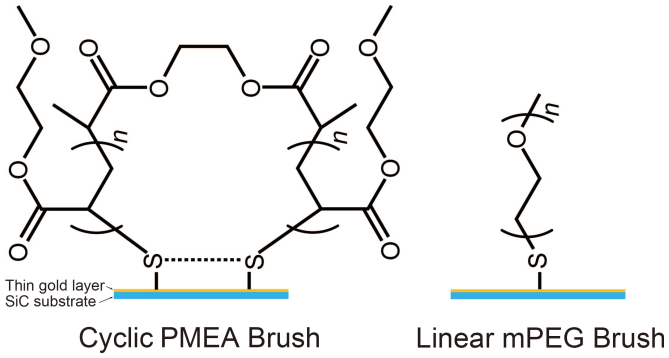

Figure 1. Chemical structure of cyclic PMEA and linear PEG brushes used in this study. These polymer brushes were prepared by grafting-to method.

XAS/XES measurement was performed at BL07LSU HORNET station in SPring-8. The humid air with controlled humidity was flowed on the samples to change the water contents in the brush samples

RESULTS AND DISCUSSION

In the XES spectrum of bulk liquid water, two significant peaks are basically observed at ca. 525.6 eV and 526.8 eV corresponding to ordered hydrogen bonds (tetrahedral coordination) and distorted hydrogen bonds, respectively [5]. Figure 2 shows XES spectra of the cyclic PMEA and linear mPEG brushes under the humidity control. In the low humidity range below a relative humidity of 65%, broad profiles peaked at the tetrahedrally-coordinated component dominates along with a sharp peak at ca. 527.1 eV. Above a relative humidity of 75%, increase of the peak at 526.5 eV was observed from the both spectra. We reported that *IW* was formed on the linear PMEA brush at a relative humidity of 75% [4]. The hydration behaviors obtained from this experiment were similar to that of our previous study, indicating that the *IW* existed on the cyclic PMEA and linear PEG brushes. Interestingly, formation of the *IW* on the cyclic PMEA brush significantly increased compared with that on the linear PMEA brush even though these polymer brushes had the same monomer unit and chemical component. This result suggested that the cyclic PMEA brush formed nano-scaled space based on its loop structure and promoted adsorption of interfacial water by confinement effect. There is a possibility that the cyclic PMEA brush shows higher biocompatibility than the linear PMEA.

In this study, we successfully carried out to trace hydration process of the interfacial water including *IW* onto the cyclic PMEA and linear mPEG brushes by XAS/XES measurement with humidity control. State of polymer chain on the outermost of surface might has a great effect on structure of the interfacial water. Although this challenging experiment make it increasingly clear that the origin of *IW* and the relationship of chemical structure with *IW* formation, the knowledge still is not enough to accomplish the ultimate design of biomaterial. Further investigation will be performed in our future work in order to clarify the essential feature of *IW* and the role on biocompatibility.

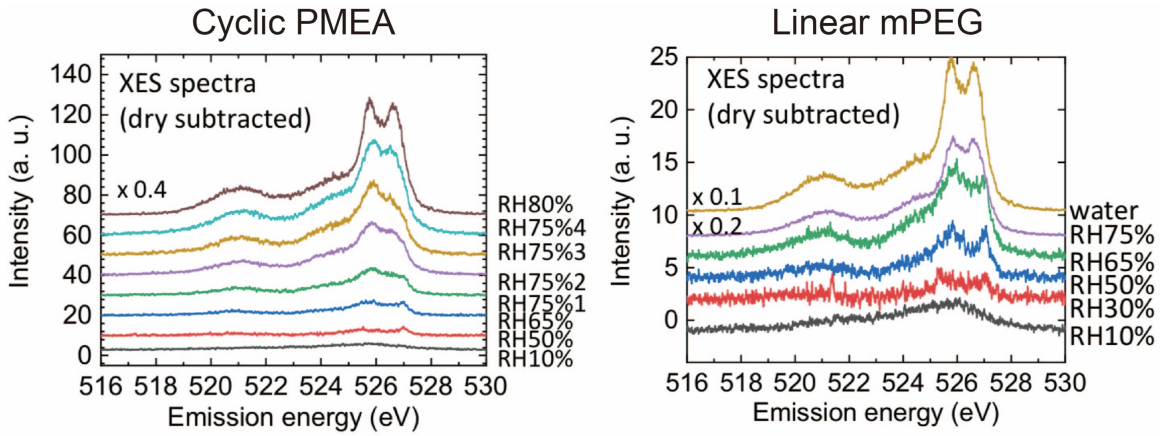

Figure 2. XES spectra of cyclic PMEA and linear mPEG brushes under the humidity control.

REFERENCES

[1] T. Tsuruta, *J. Biomater. Sci. Polym. Ed.*, **2010**, *21*, 1831-1848.
[2] M. Tanaka *et al.*, *Polym. Int.*, **2000**, *49*, 1709-1713.
[3] D. Murakami *et al.*, *Activity Report of Synchrotron Radiation Laboratory 2018*, **2019**, 68-69.
[4] D. Murakami *et al.*, *Activity Report of Synchrotron Radiation Laboratory 2018*, **2019**, 70-71.
[5] T. Tokushima *et al.*, *Chem. Phys. Lett.*, **2008**, *460*, 387-400.

DEVELOPMENT OF TIME-RESOLVED X-RAY PHOTOELECTRON DIFFRACTION FOR THE OBSERVATION OF THE STRUCTURAL DYNAMICS OF EPITAXIAL SILICENE

Kouichi Hayashi[1,2], Artoni Kevin R. Ang[1], Koji Kimura[1], Yuichiro Fukatsu[1], Susumu Yamamoto[3], Iwao Matsuda[3], Takahiro Yonezawa[4], Antoine Fleurence[4], Yukiko Yamada-Takamura[4]

[1]*Department of Physical Science and Engineering, Nagoya Institute of Technology, Nagoya, Japan*
[2]*Frontier Research Institute for Materials Science, Nagoya Institute of Technology, Nagoya, Japan*
[3]*Institute of Solid State Physics, The University of Tokyo, Kashiwanoha, Chiba, Japan*
[4]*School of Materials Science, Japan Advanced Institute of Science and Technology, Ishikawa, Japan*

Introduction

Over the past half-century, photoelectron spectroscopy (PES) has become one of the most important experiments in physics, chemistry and material science. Among the related techniques, X-ray photoelectron diffraction (XPD) has grown into a powerful technique in studying surface structures. Since the first reported XPD experiments by Siegbahn and Fadley in the 1970's, XPD has been used to investigate the structures of surface reconstructions, adsorbates, interfaces and thin films.

Through the years, PES has evolved significantly alongside the rapid developments in electron spectrometers, synchrotron radiation facilities, laser light sources, and other related technologies. Typical PES experiments can now resolve nm-resolution spatial information, time-resolved and even spin-resolved information. Taking advantage of these developments, new dimensions of space-, time- and spin- can incorporated into XPD experiments.

In this work, we demonstrate, for the first time, time-resolved X-ray photoelectron diffraction (trXPD) of an epitaxial silicene layer using a time-resolved two-dimensional angle-resolved time-of-flight (2DARTOF) system. The evolution of the diffraction rings (DR) and the forward focusing peaks (FFP) after laser irradiation can be used to extract atomic resolution structural information about the surface structure (Fig. 1). The 2DARTOF system in BL07LSU is well suited for this experiment because of its high energy and angular resolutions, and most importantly, its simultaneously recording of the photoemission intensity as a function of θ_x, θ_y, and E.

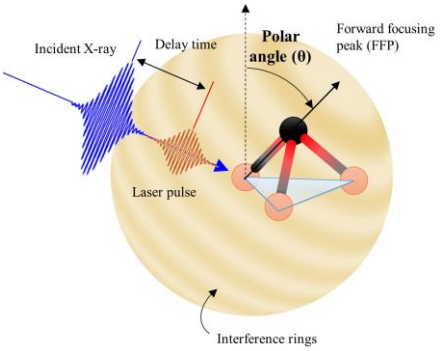

Fig. 1. Schematic diagram of the time-resolved XPD experiment.

Experiment and data processing

The experiments were performed using an epitaxial silicene sample grown on a ZrB_2 thin film [1]. It has been shown that this epitaxial silicene layer has minimal electronic interactions with the substrate, and that the silicene layer buckled easily, resulting in a mixed sp^2/sp^3 hybridization that can be tuned to control its electronic properties [2,3]. XPS studies have shown that the Si atoms occupy at least 3 chemically different sites, and that the surface structure consists of a planar surface structure with an adatom [3,4]. This sample was chosen because of its relatively simple surface structure, and the current interest in silicene for next generation electronic device applications.

The sample was prepared *in situ* by the spontaneous segregation during the annealing of the ZrB_2/Si(111) substrate at 800°C [1]. LEED and the Si 2p core-level spectra confirms the formation of a well-defined silicene layer.

The photoemission experiments were done using a photon energy of $h\nu$ = 300 eV. The ARTOF detector was set to simultaneously measure the photoemission intensity with an acceptance angle of ±13°, within the energy range 97-103 eV. To obtain a larger section of the hologram pattern, the sample's orientation was scanned along the [1120] direction. For the time-resolved experiments, a 1.5 eV, 208 kHz laser was used.

Compared to other electron detector systems used in XPD, the 2DARTOF system has a major advantage in that it can simultaneously measure $I(\theta_x, \theta_y, E)$ (Fig. 2a). To extract the angle-integrated Si 2p spectra, the raw data is integrated along both the θ_x and θ_y directions. To get the XPD spectra, the raw data is integrated within a small energy region centred around the Si 2p binding energy (Fig. 2c). However, this will contain XPD signal from Si atoms at all sites. To separate the XPD patterns from the Si atoms occupying different sites, peak fitting of the spectra at each (θ_x, θ_y) pixel is done [5].

The extracted XPD patterns are then normalized by a background image obtained by integrating the raw 3D data within a narrow energy region in the low binding energy side.

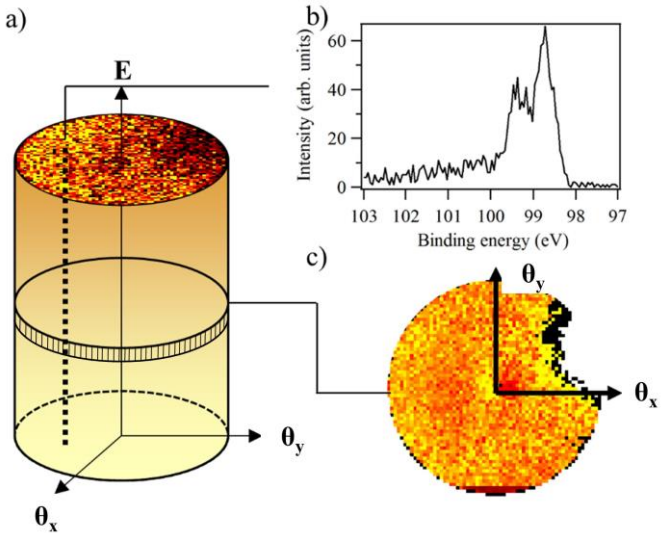

Fig. 2. a) Schematic diagram of the raw data obtained by the 2DARTOF system, b) a typical Si 2p spectra from a (θ_x, θ_y) pixel, and c) a raw 2D cut taken at the Si 2p binding energy.

Results

Figure 3a shows the "planar" structural model of epitaxial silicene showing the 3 distinct sites occupied by Si atoms. From the peak fitting of the angle integrated Si 2p spectra (Fig. 3b), the 2 main peak components corresponding to the Si atom at the Si_A and Si_B sites were resolved. The simulated and experimental XPD patterns extracted for these peak components are shown in Fig. 3c) and 3d), where the DR and FFPs in the simulation are well resolved in the experiment.

Epitaxial silicene consists mostly of in-plane scatterers, and thus the XPD patterns are dominated by these DRs. In XPD pattern of Si_B, a strong FFP at θ~48° is observed, which corresponds to the direction of the Si_C atom from the Si_B emitter. This confirms that the 2DARTOF system can be a viable system for XPD measurements.

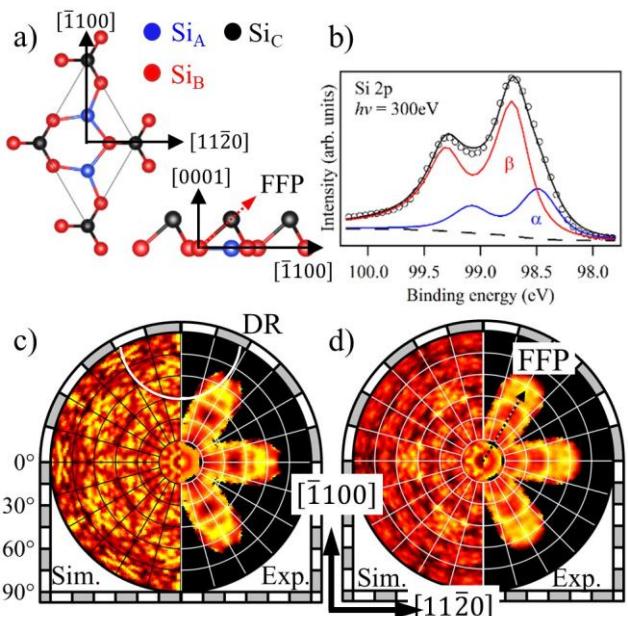

Fig. 3. a) "Planar" model for epitaxial silicene, b) the Si 2p core level spectra measured from the sample, and simulated and experimental XPD patterns from the c) Si_A and d) Si_B component.

Conclusion

In this work, we have demonstrated for the first time that the 2DARTOF system is well-suited in XPD experiments. The simultaneous measurement of $I(\theta_x, \theta_y, E)$, makes acquisition of XPD patterns faster, opening up the possibility of time-resolved XPD measurements. In our future work, we will obtain the trXPD patterns of epitaxial silicene in the pump-probe scheme.

REFERENCES

[1] A. Fleurence, et al., Phys. Rev. Lett. **108**, 245501 (2012).
[2] R. Friedlein and Y. Yamada-Takamura. J. Phys. Condens. Matter **27**, 203201 (2015).
[3] C.C. Lee, et al., Phys. Rev. B, **90**, 075422 (2014).
[4] R. Friedlein, et al., J. Chem. Phys. **140**, 184704 (2014).
[5] K. Tsuitsui, et al., Nano Lett. **17**, 7533 (2017).

TIME-RESOLVED X-RAY PHOTOELECTRON DIFFRACTION STUDY OF EPITAXIAL SILICENE

Kouichi Hayashi[1,2], Artoni Kevin R. Ang[1], Koji Kimura[1], Yuichiro Fukatsu[1], Susumu Yamamoto[3], Iwao Matsuda[3], Takahiro Yonezawa[4], Antoine Fleurence[4], Yukiko Yamada-Takamura[4]

[1]*Department of Physical Science and Engineering, Nagoya Institute of Technology, Nagoya, Japan*
[2]*Frontier Research Institute for Materials Science, Nagoya Institute of Technology, Nagoya, Japan*
[3]*Institute of Solid State Physics, The University of Tokyo, Kashiwanoha, Chiba, Japan*
[4]*School of Materials Science, Japan Advanced Institute of Science and Technology, Ishikawa, Japan*

Introduction

Silicene is a monolayer of Si atoms arranged in a honeycomb lattice that exhibits massless Dirac fermions, similar to its carbon based counterpart in graphene. The development of silicene based devices has seen significant interest recently because of the expected remarkable electronic properties, stronger spin-orbit coupling of Si, and the ease of adapting such technologies into the already Si-based manufacturing infrastructure. Until recently, silicene could only be synthesized on conductive substrates, resulting in electronic interactions with the substrate. It was recently demonstrated that silicene with minimal substrate interactions can be grown on a ZrB_2/Si(111) substrate through the surface segregation of Si atoms[1]. This silicene layer was found to buckle easily, resulting in sp^2/sp^3 hybridization that can tailored to tune its electronic properties [1,2]. Photoemission studies have shown that the Si atoms occupy at least 3 chemically different sites on the silicene layer (Fig. 1a) [1,3]. In this study, we investigate the local structures of epitaxial silicene and the structural dynamics induced by laser irradiation.

Experiment

The sample was prepared *in situ* by the spontaneous segregation during the annealing of the ZrB_2/Si(111) substrate at 800°C [1]. The ZrB_2/Si(111) substrate was prepared elsewhere, and degassed in the prior to sample preparation. The silicene surface was confirmed by LEED and the core-level spectra.

The photoemission experiments were done using a photon energy of $h\nu$ = 300 eV. The ARTOF detector was set to simultaneously measure the photoemission intensity with an acceptance angle of ±13°, within the energy range 97-103 eV. To obtain a larger section of the hologram pattern, the sample's orientation was scanned along the [1120] direction. For the time-resolved experiments, a 1.5 eV, 208 kHz laser was used.

Results

The LEED and Si 2p spectra confirmed the formation of a well-defined silicene layer. From the peak fitting of the Si 2p spectra (Fig. 1b), the 2 main peak components of silicene were resolved. These 2 peaks correspond to the Si atoms occupying the Si_A and Si_B sites in Fig. 1a [2,3]. The XPD patterns of these 2 peak components were extracted by peak fitting [5], and are shown in the right hemispheres of Fig. 1c and 1d. The corresponding simulations are shown in the left hemispheres. Some diffraction rings (DR) and forward focusing peaks (FFP) in the simulations are well reproduced in the experiment.

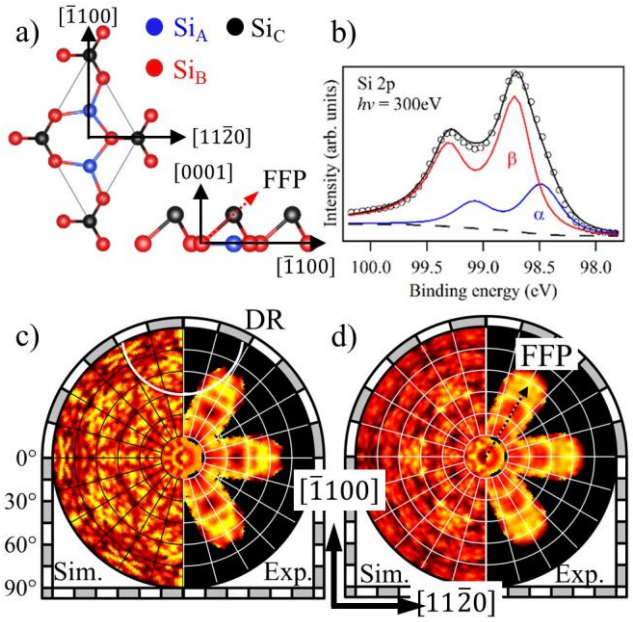

Fig. 1. a) "Planar" model for epitaxial silicene, b) the Si 2p core level spectra measured from the sample, and simulated and experimental XPD patterns from the c) Si_A and d) Si_B component.

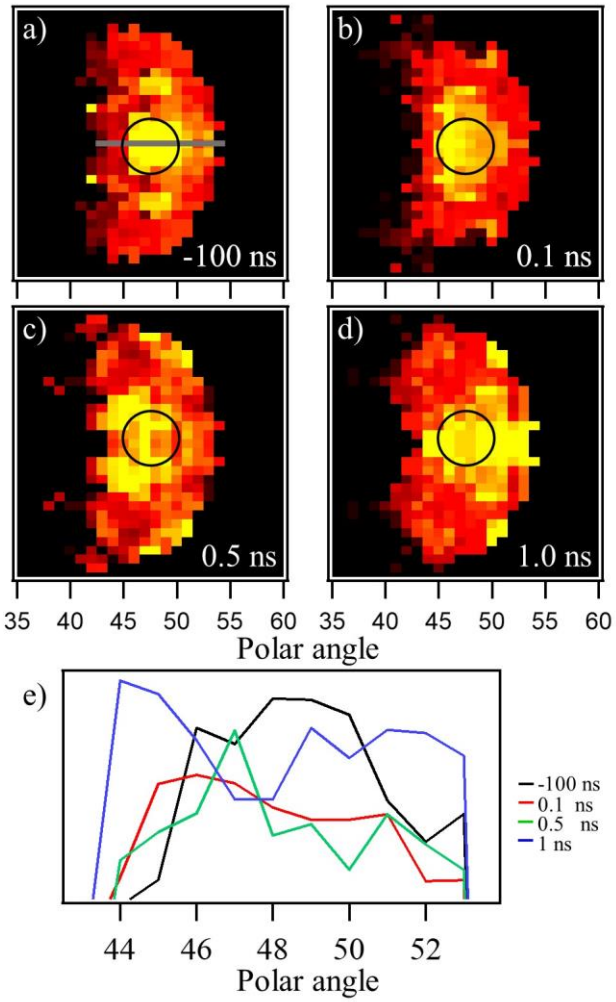

Fig. 2. The time-resolved XPD patterns of the SiB component taken at various delay times: a) -100ns, b) 0.1 ns, c) 0.5 ns and d) 1.0 ns, and d) the line profiles taken across the FFP.

In this sample, most of the neighboring scatterers are in-plane, thus the XPD patterns are dominated by these DRs. Meanwhile, the XPD pattern of Si_B shows a strong FFP at θ~48°, which corresponds to the direction of the Si atom at the Si_C site from the emitter at Si_B.

In the time-resolved experiments, we focused on this FFP at θ~48° to observe any changes in the surface structure. At -100 ns, the FFP is observed as a strong peak (marked with the black circle in Fig. 2a). At later delay times (Figs. 2b, 2c, 2d), the FFP is first seen decreasing in peak intensity and shifting to lower θ (0.1 and 0.5 ns), before shifting to higher θ and recovering its intensity (1.0 ns). At 1.0 ns, the shift to higher polar angles corresponds to an in-plane expansion of the silicene layer, which could be explained by laser-induced thermal expansion.

Meanwhile, at 0.1 and 0.5 ns, the decrease in FFP peak intensity suggests an intermediate structure that occurs before the onset of thermal equilibrium between the photoexcited electrons and phonons. This could be due to bond softening due to the increased anti-bonding character of the excited charge distribution. At higher laser fluence, it has been reported that this can even result in bond breaking and the formation of disordered state, a non-thermal melting of the surface [6,7].

While the details of the structural changes observed in silicene is still not clear, this work has demonstrated that time-resolved XPD experiments are now feasible and can be used to probe the structural dynamics of surfaces. Analysis of the evolution of the diffraction rings and forward focusing peaks in the XPD patterns can provide element sensitive, atomic resolution structure information about surfaces. Further experiments and first principles calculations are needed to completely understand the evolution of the epitaxial silicene structure after laser-induced heating.

REFERENCES

[1] A. Fleurence, et al., Phys. Rev. Lett. **108**, 245501 (2012).
[2] R. Friedlein and Y. Yamada-Takamura. J. Phys. Condens. Matter **27**, 203201 (2015).
[3] C.C. Lee, et al., Phys. Rev. B, **90**, 075422 (2014).
[4] R. Friedlein, et al., J. Chem. Phys. **140**, 184704 (2014).
[5] K. Tsuitsui, et al., Nano Lett. **17**, 7533 (2017).
[6] K.J. Gaffney, et al., Phys. Rev. Lett. **95**, 125701 (2005).
[7] M. Harb et al. Phys. Rev. Lett., **100**, 155504 (2008).

ELECTRIC STRUCTURE OF WATER IN THE VICINITY OF MODEL ORGANIC SURFACES BY X-RAY EMISSION SPECTROSCOPY

Tomohiro Hayashi

Department of Materials Science and Engineering, School of Materials and Chemical Technology

Tokyo Institute of Technology

JST-PRESTO

Introduction

Self-assembled monolayers (SAMs) have been employed as model organic surfaces since the 1980s (Figure 1). Just by changing the terminal groups of the molecules, we can easily control the physicochemical properties of the surfaces. In a field of biomaterial and biosensing, SAMs are often employed as scaffolding layers for protein and cells or passivating layer preventing non-specific adsorption of non-target molecules. [1] Recently, water-mediated force has been found to play an important role to govern the interaction of materials with protein molecules and cells. [2-5] However, the properties of the interfacial water, in particular, hydrogen bonding state and the mechanism underlying the water-mediated force are still matters of intense debate. [1] In this work, we attempt to answer these questions by using X-ray emission spectroscopy (XES), which provides a detailed picture of the hydrogen bonding state of water.

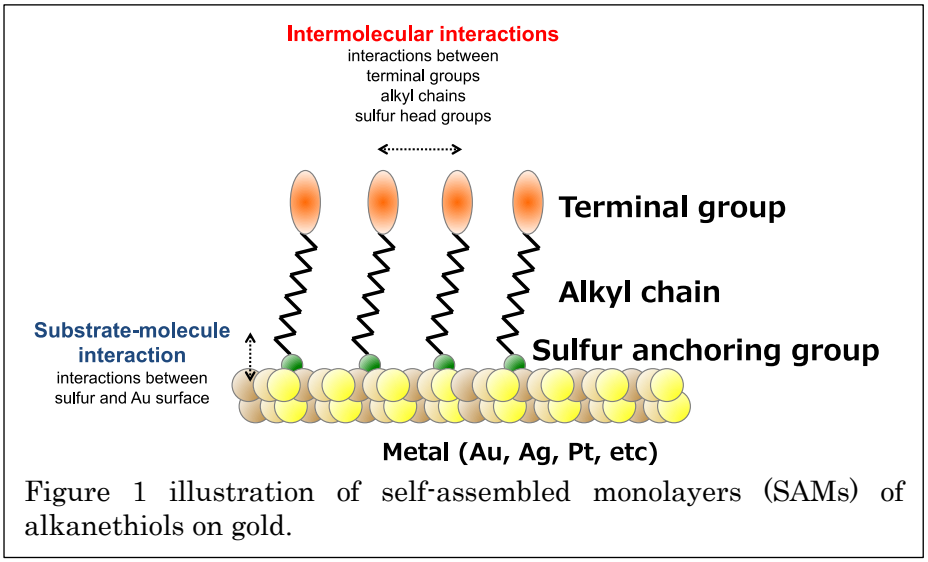

Figure 1 illustration of self-assembled monolayers (SAMs) of alkanethiols on gold.

Experimental

In this work, we employed a measurement setup shown in Fig. 2. SAMs were formed on the backside of the window. In this work, we used 8 types of SAMs. They are hydrophobic (metyl-terminated: C8), hydrophilic (hydroxy-terminated: OH), positively charged (trimethylamine-terminated: TMA), negatively charged (sulfuric acid-terminated: SA), and non-fouling [oligoethylene glycol: EG and sulfobetaine: SB]. The humidity is changed to vary the amount of water condensed on the SAMs. The energy of the incident X-ray was fixed at 550 eV.

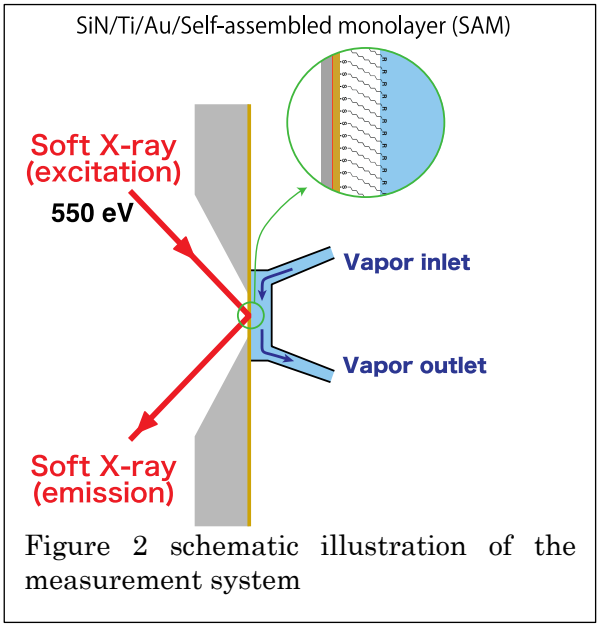

Figure 2 schematic illustration of the measurement system

Results and discussion

We confirmed that the thickness of the water strongly depended on the humidity in the chamber. From the quartz crystal microbalance (QCM), the thickness of water at relative humidity at 28 degree in Celcius is about 0.5 to 1 nm.

Figure 3 shows XE spectra of water adsorbed on the SAMs. For water molecules in the vicinity of OH- and C8-SAMs, the tetrahedral-coordinated water (ice-like water) is concentrated only near the interface (with a film thickness of less than 0.5 nm) and steeply changes to the structure of bulk water. In contrast, it was found that water molecules with hydrogen bonding in the distorted tetrahedral coordination was dominant for non-fouling SAMs (Fig. 3). Therefore, the distorted tetrahedral-coordinated water layer is key to the anti-adhesion properties, in agreement with our previous findings.

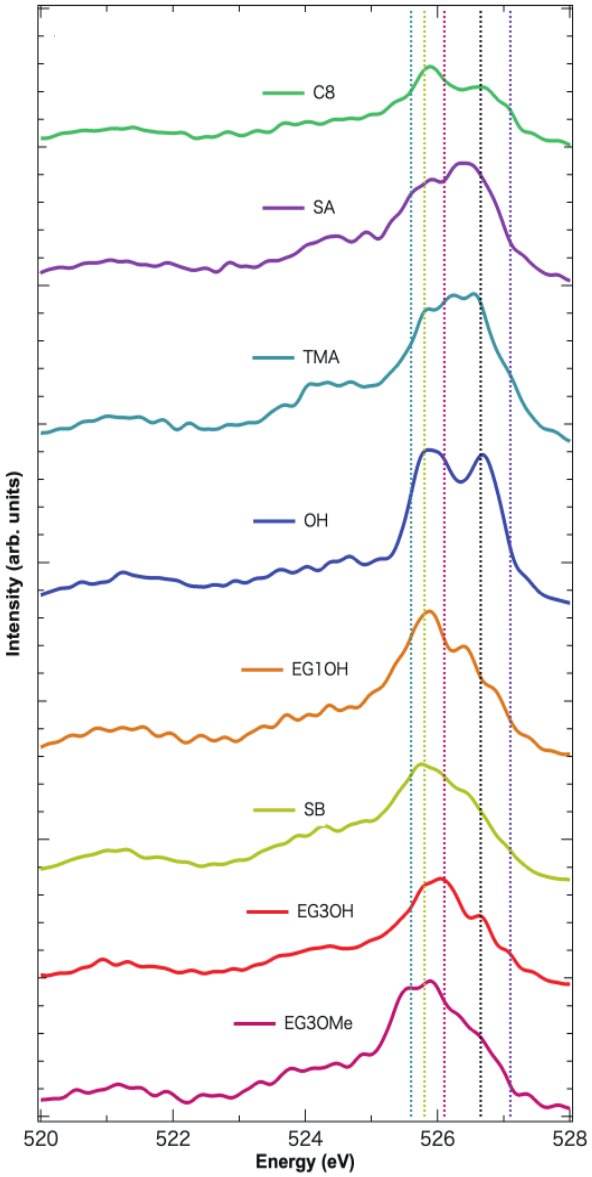

Figure 3 X-ray emission spectra of water adsorbed on SAMs.

REFERENCES

(1) Hayashi, T.; Hara, M., Nonfouling self-assembled monolayers: mechanisms underlying protein and cell resistance. *Current Physical Chemistry* **2011,** *1*, 90-98.

(2) Chang, R.; Asatyas, S.; Lkhamsuren, G.; Hirohara, M.; Mondarte, E. A. Q.; Suthiwanich, K.; Sekine, T.; Hayashi, T., Water near bioinert self-assembled monolayers. *Polym. J. (Tokyo, Jpn.)* **2018,** *50*, 563-571.

(3) Kanayama, N.; Sekine, T.; Ozasa, K.; Kishi, S.; Nyu, T.; Hayashi, T.; Maeda, M., Terminal-Specific Interaction between Double-Stranded DNA Layers: Colloidal Dispersion Behavior and Surface Force. *Langmuir* **2016,** *32*, 13296-13304.

(4) Sekine, T.; Tanaka, Y.; Sato, C.; Tanaka, M.; Hayashi, T., Evaluation of Factors To Determine Platelet Compatibility by Using Self-Assembled Monolayers with a Chemical Gradient. *Langmuir* **2015,** *31*, 7100-5.

(5) Tanaka, M.; Hayashi, T.; Morita, S., The roles of water molecules at the biointerface of medical polymers. *Polym. J. (Tokyo, Jpn.)* **2013,** *45*, 701-710.

MEASUREMENT OF THE THICKNESS DEPENDENCE OF THE MAGNET-OPTICAL CONSTANTS OF METAL FE USING FAST POLARIZATION SWITCHING

Yasuyuki Hirata[1], Keisuke Ikeda[1], Kohei Yamagami[1], Yujun Zhang[2], Hiroki Wadati[2], Souliman El Moussaoui[1], Iwao Matsuda[1]

[1]*Synchrotron Radiation Laboratory, Institute for Solid State Physics, University of Tokyo*

[2]*Graduate School of Material Science, University of Hyogo*

Magneto-optical effect is quite important not only for its use in devices such as magneto-optical storage devices, but also as a probe for unraveling the spin and orbital states of electrons in magnetic materials, therefore researchers of magnetism have measured magneto-optical spectrum at various wavelengths. In particular, the measurement of resonant X-ray magnetic circular dichroism (R-XMCD) and resonant X-ray magneto-optical Kerr effect (R-XMOKE) using soft X-ray are powerful measurement methods that can selectively observe the magnetic behavior of each 3*d*-transition-metal element, which is a main player of magnetism. However, despite the fact that the fine structure of the spectrum is important for analysis, R-XMCD for materials with a small magnetic signal has a difficulty on improving accuracy because it requires subtraction between two absorption/reflection spectra for the incident light with different polarizations. R-MOKE measurement is free from this problem, but it has an experimental limitation that it takes a long time for measurement because it requires an ellipsometry scan for each measurement point.

Taking advantage of the characteristics of the BL07LSU light source where high-speed polarization switching is available [1,2], from the 2016A period we have performed the R-MOKE measurement using the optical delay modulation method [3], and measured the magneto-optical constant of the Fe thin film (30 nm thickness) [4]. With this method, the real part (corresponding to Kerr rotation angle) and the imaginary part (corresponding to ellipticity) of the off-diagonal component of the permittivity can be simultaneously measured independently in a short time, without Kramers-Kronig transformation analysis. Although the obtained permittivity of Fe thin film was generally in good agreement with the result of the first-principles calculation, a dip structure at Fe L_3 absorption edge in the measured spectrum could not be reproduced from the calculation. It is very important to distinguish experimentally whether the dip structure is intrinsic in Fe metal, comes from interference with the thin film [5], or has another origin. In this study, we performed an R-MOKE measurement on Fe thin films with different film thickness by the optical delay modulation method using polarization switching, and clarified the film thickness dependence of the magneto-optical spectrum. The dip structure was hardly reproduced, which indicates it is not intrinsic in the magneto-optical spectrum of Fe metal. No systematic film thickness dependence was observed in the permittivity spectrum.

We prepared two Fe thin films with different thickness (30 nm thick and 15 nm thick) on MgO substrate, and capped with Ru layer (5 nm thick) to prevent surface oxidization. The reflection spectroscopy measurement with grazing geometry (incident angle of 80 degree) was performed at Fe L_3 and L_2 edge under the in-plane magnetic field of 0.3 T applied by superconducting coil magnet. The polarization of the incident light was continuously modulated between left circular polarization and right circular polarization with the frequency of 13 Hz. The reflected light was analyzed with ellipsometer at both *p*-polarization and *s*-polarization geometry. The 13 Hz component of analyzed signal corresponded to ellipticity, and the 26 Hz component of analyzed signal corresponded to Kerr rotation angle.

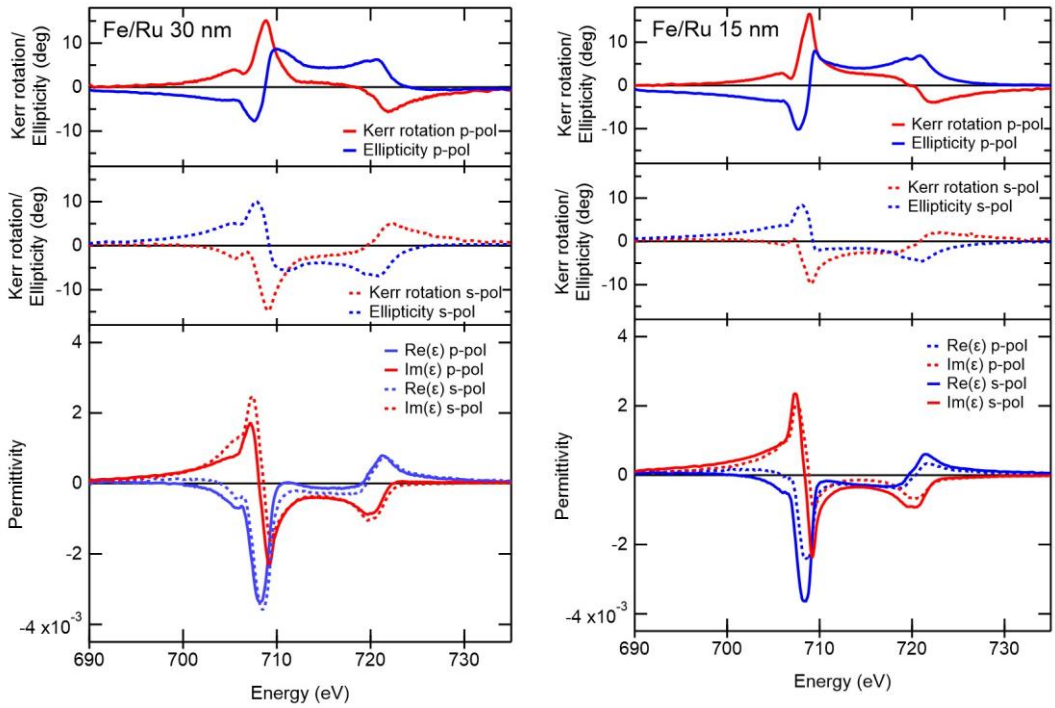

Fig. 1: Kerr rotation angle, ellipticity, and off-diagonal permittivity ε of Fe film with 30 nm thick (left panel) and Fe film with 15 nm thick (right panel). Solid line (dashed line) is obtained from *p*-polarization (*s*-polarization) reflection measurement, respectively.

Figure 1 shows the measured spectra of Kerr rotation angle, ellipticity, and off-diagonal permittivity of Fe film (30 nm thick) and Fe film (15 nm thick). Off-diagonal permittivity was derived from Kerr rotation angle, ellipticity, and refraction index of Fe [6]. Under both *p*-polarization and *s*-polarization reflection geometry, obtained off-diagonal permittivity spectra show good agreement with theoretical calculation. We cannot find any systematic dependency on thickness in the spectra of the 30 nm thick film and the 15 nm thick film, and a large dip structure observed in previous experiment has almost disappeared. Our result clearly shows the dip structure is neither real magnetic signal of Fe nor originating from an optical interference within the film. The capping layers of the samples are different between previous measurement (Cu 2 nm thick and Ta 2 nm thick) and ours (Ru 5 nm thick), but it is less likely that the dip structure comes from the capping layer because Cu and Ta do not have any optical structure at the energy around Fe *L*-edge. One possible origin of the dip structure is surface oxidization of the sample which may be caused by x-ray radiation.

In conclusion, we have observed the thickness dependence of off-diagonal permittivity of Fe thin film at Fe *L*-edge by the optical delay modulation method. No systematic dependency on thickness was found out, and the dip structure in spectrum observed in previous experiment was shown not to be intrinsic.

REFERENCES

[1] S. Yamamoto *et al*., J. Synchrotron Radiat. **21**, 352 (2014).
[2] I. Matsuda *et al*., Nucl. Instrum. Methods Phys. Res., **767**, 296 (2014).
[3] K. Sato, Jpn. J. Appl. Phys. **20**, 2403 (1981).
[4] Y. Kubota *et al*., Phys. Rev. B **96**, 214417 (2017).
[5] S. Valencia *et al*., Physica B **345**, 189 (2004).
[6] H.-C. Mertins *et al*., J. Magn. Magn. Mater. **240**, 451 (2002).

Creation of multi-dimensional operando photoelectron spectroscopy (I) Selection of industry-government-academia collaborative model sample

Hirokazu Fukidome[1], Takamasa Kamogawa[1], Naoka Nagamura[2,3], Masaharu Oshima[4], Masato Kotsugi[5], and Issei Watanabe[6]

[1]*Research Institute of Electrical Communication, Tohoku University, Sendai, Miyagi, Japan.*
[2]*National Institute for Materials Science (NIMS), Tsukuba, Ibaraki, Japan.*
[3]*PRESTO, Japan Science and Technology Agency, Honcho, Saitama, Japan.*
[4]*Institute for Solid State Physics, The University of Tokyo, Kashiwa, Chiba, Japan.*
[5]*Tokyo University of Science, Katsushika, Tokyo, Japan.*
[6] *National Institute of Information and Communications Technology (NICT), Koganei, Tokyo, Japan.*

Virus and environmental issues threaten the sustainability of mankind. To balance the suppression of virus infection and active socio-economic activities, we should develop information technologies enabling a high telepresence communications. For this purpose, the wireless communication using THz frequencies is needed, indicating 100 times speeding up, compared to the current wireless communication, so-called 5G.

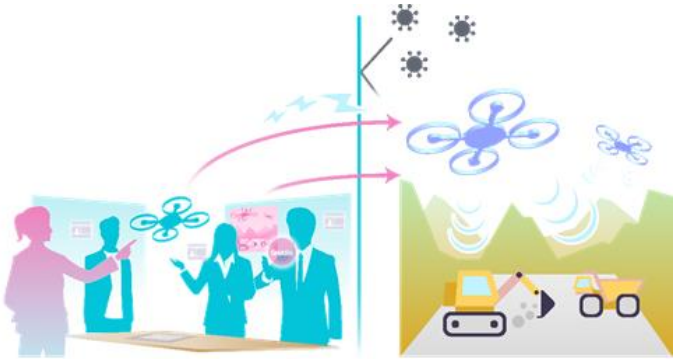

Fig. 1 A schematic view of the high telepresence communication

Two-dimensional (2D) materials such as graphene and ultrathin semiconductor devices using AlGaN/GaN [1] and InGaAs heterointerfaces is promsing for THz devices for high speed wireless communication, 6G and more. This due to excellent electronic properties, such as giant carrier mobility and ultrahigh saturation velocity, and suppression of so-called short-channel effects arising from the ultrathinness of the channles. With the advance of miniaturization and integration of devices, the importance of interfaces further increases. Especially, 2D materials are sensitive to interface environment, so many environmental parameters drive the electronic and chemical properties of 2D materials. Moreover, better spatial and time resolution is required for the advanced device analysis. Then, we attempt to realize multi-dimensional operando photoelectron spectroscopy using machine learning analysis techniques in the viewpoint of Measurement Informatic.

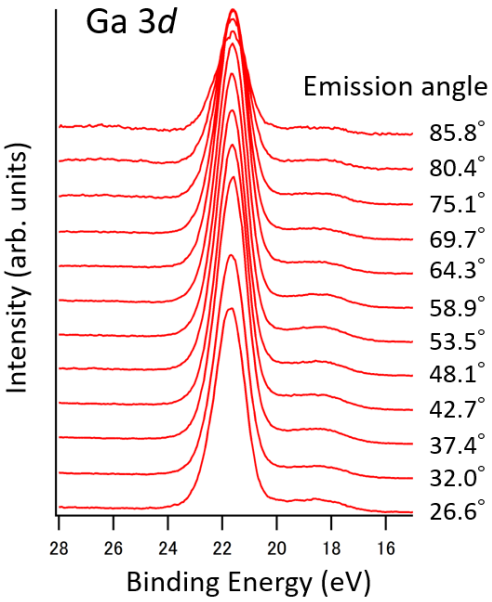

Fig. 2 Angle resolved Photoelectron spectroscopy of Ga 3*d* peak for the GaAs heteroepitaxial layers.

At first, we performed depth profiling of III-V compound semiconductor heteroepitaxial layers by ARPES measurements. Maximum Entropy Method is applied to enable sub nm order analysis (Fig. 2)[2].

In-plane 2D spectral mapping is also carried out for InP high electron mobility transistor (HEMT) device structures. Present in-plane spatial resolution of 3D nano-ESCA is ~70 nm,

which is deteriorated by mechanical vibrations, thermal drift, charging effect, and so on. To overcome the limit of spatial resolution and make it possible to observe objects in the size of several nms, we adopt sparse modelling approach for the spectral intensity mapping datasets. Fig. 3(a) is a low-resolution image taken by coarse steps in short measurement time. Using this kind of down-sampling mappings, super-resolution image processing by sparse modelling [3] was performed as shown in Fig. 2(b). Effective spatial resolution seems to be improved by this machine learning approach.

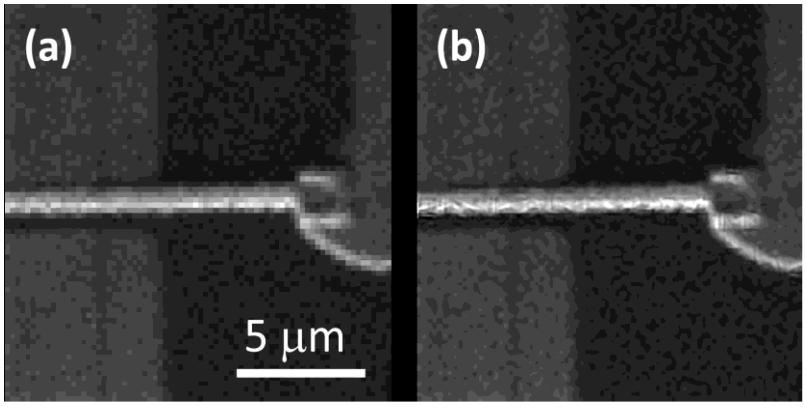

Fig. 3 (a) Photoelectron intensity mapping image for the Au 4*f* peak for the InP-HEMT device structure. Low-resolution image by down sampling. (b) Super-resolution image using sparce modeling.

Our final goal is to achieve below 10 nm-resolution with the aid of machine learning, such as super-resolution. Then, we will plan to execute industry-government-academia collaboration that utilize operando 3D nano-ESCA to develop novel next-generation communication devices necessary for balancing the suppression of virus infection and active socio-economic activities.

REFERENCES

[1] H. Fukidome et al. Sci. Rep.8, 13268 (2018).
[2] K. Horiba et al. Rev. Sci. Instrum. 82, 113701 (2011).
[3] T. Kato et al. Neurocomputing 240, 115 (2017).

OPERAND MEASUREMENT OF ALL SOLID-STATE LI-ION BATTERYS BY PHOTOELECTRON MICROSPECTROSCOPY

Eiji Hosono[a,b,c], Wenxiong Zhang[d], Daisuke Asakura[b,c], Naoka Nagamura[e], Masaharu Oshima[f], Yoshihisa Harada[c,d, f]

[a] National Institute of Advanced Industrial Science and Technology (AIST), Global Zero Emission Research Center, 1-1-1 Umezono, Tsukuba, Ibaraki 305-8568, Japan

[b] National Institute of Advanced Industrial Science and Technology (AIST), Research Institute for Energy Conservation, 1-1-1 Umezono, Tsukuba, Ibaraki 305-8568, Japan

[c] AIST-UTokyo Advanced Operando-Measurement Technology Open Innovation Laboratory, 5-1-5 Kashiwanoha, Kashiwa, Chiba 277-8565, Japan

[d] Institute for Solid State Physics (ISSP), The University of Tokyo, 5-1-5 Kashiwanoha, Kashiwa, Chiba 277-8581, Japan

[e] National Institute for Materials Science, Research Center for Advanced Measurement and Characterization, 1-2-1 Sengen, Tsukuba, Ibaraki 305-0047, Japan

[f] Synchrotron Radiation Research Organization, The University of Tokyo, 7-3-1 Hongo, Bunkyo-ku, Tokyo, 113-8656, Japan

Development of high-performance lithium-ion battery (LIB) for stationary type and vehicle is an important research topic. The total development of LIB is very difficult, because performances such as energy density, power performance, cycle performance, and safety property are in the trade-off relationships. Thus, comprehensive researches and developments are highly important to development of LIB. Detailed understanding of the redox reactions by Li-insertion/extraction, structural change, electronic state change for the materials in LIBs is important to develop innovative materials for LIBs. In these days, cutting-edge analyses methods are necessary in addition to the innovative materials development.

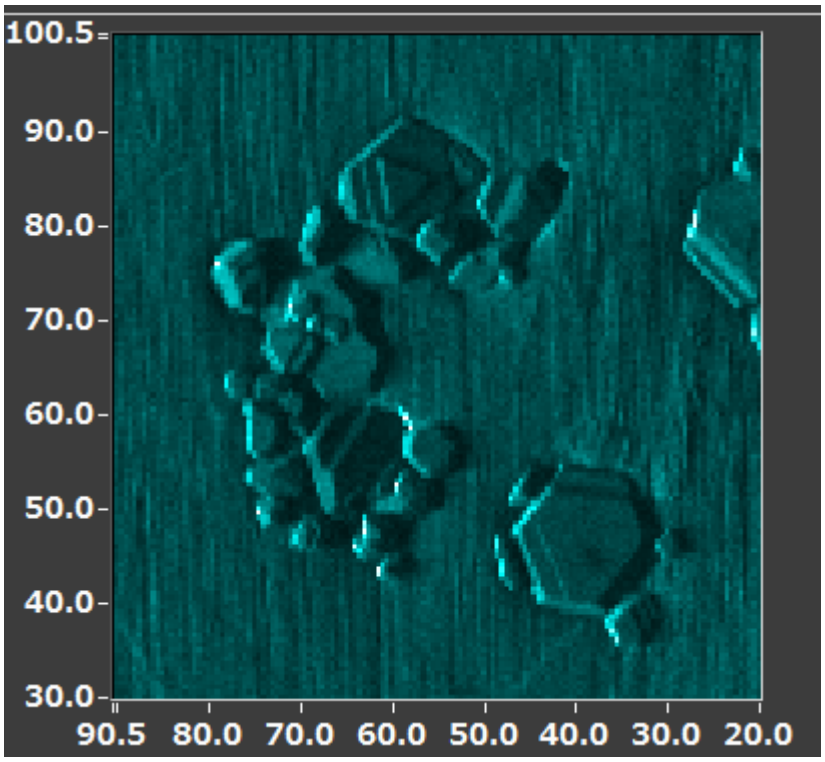

Figure 1 XPS images of $LiCoO_2$

To truly understand LIBs, synchrotron radiation soft X-ray spectroscopy is a useful technique with elemental selectivity, valence selectivity and orbital selectivity. We have been studying the charge-discharge mechanisms of LIBs based on the electronic-structure analysis by soft X-ray spectroscopy. In addition, *operando* measurement is very important because LIB is a high voltage device. Even deconstruction of LIB in the glovebox filled by inert Ar gas, the potential control of active material is difficult. *Operando* measurement system in soft X-ray beamline is our core-technique. We reported the operando soft x-ray emission spectroscopy under the charge-discharge operation [1,2].

Furthermore, microspectroscopy is another important point because the redox reaction by charge-discharge reaction influenced by the position like a facet of an electrode material and the interfaces between the electrode materials and electrolytes. Spectroscopy with spatial resolution is of particular importance.

We reported *operando* photoemission spectromicroscopy of single crystalline $Li_4Ti_5O_{12}$ (an anode material) [2] and $LiCoO_2$ (an cathode materials) [3] by 3DnanoESCA [4] with all-solid-state LIB. The soft X-ray photoemission spectromicroscopy experiments have been conducted at BL07LSU of SPring-8.

Here, we measured single crystalline LiCoO2 cathode material with clear facet. Figure 1 shows images of XPS mapping image of single crystalline $LiCoO_2$. From the clear image of each facet, resonant XPS was conducted.

ACKNOWLEDGEMENT

This work was conducted under the international joint research program for innovative energy technology by METI, Japan.

REFERENCES

[1] D. Asakura, E. Hosono, H. Niwa, H. Kiuchi, J. Miyawaki, Y. Nanba, M. Okubo, H. Matsuda, H.S. Zhou, M. Oshima, and Y. Harada, "Operando Soft X-ray Emission Spectroscopy of $LiMn_2O_4$ Thin Film Involving Li-ion Extraction/insertion Reaction", Electrochem. Commun., 50, 93 (2015).

[2] D. Asakura, Y. Nanba, M. Okubo, H. Niwa, H. Kiuchi, J.Miyawaki, M. Oshima, E. Hosono, Y. Harada, "Operando soft X-ray emission spectroscopy of the Fe_2O_3 anode to observe the conversion reaction", *Physical Chemistry Chemical Physics*, 21, 26351 (2019).

[3] K. Akada, T. Sudayama, D. Asakura, H. Kitaura, N. Nagamura, K. Horiba, M. Oshima, E. Hosono, Y. Harada, "Operando measurement of single crystalline Li4Ti5O12 with octahedral-like morphology by microscopic X-ray photoelectron spectroscopy", J. Electron Spectrosc. Relat. Phenom., 233, 64 (2019).

[4] K. Akada, T. Sudayama, D. Asakura, H. Kitaura, N. Nagamura, K. Horiba, M. Oshima, E. Hosono, Y. Harada, "Microscopic photoelectron analysis of single crystalline $LiCoO_2$ particles during the charge-discharge in an all solid-state lithium ion battery", *Scientific Reports*, *9*, 12452 (2019).

[5] K. Horiba, Y. Nakamura, N. Nagamura, S. Toyoda, H. Kumigashira, M. Oshima, K. Amemiya, Y. Senba, H. Ohashi, Scanning photoelectron microscope for nanoscale three-dimensional spatial-resolved electron spectroscopy for chemical analysis. *Rev. Sci. Instrum.* 82, 113701 (2011).

MAPPING MEASURMENT OF SINGLE CRYSALLINE LITHIUM METAL OXIDE BY ALL SOLID-STATE LI-ION BATTERYS

Eiji Hosono[a,b,c], Wenxiong Zhang[d], Daisuke Asakura[b,c], Naoka Nagamura[e], Masaharu Oshima[f], Yoshihisa Harada[c,d, f]

[a] National Institute of Advanced Industrial Science and Technology (AIST), Global Zero Emission Research Center, 1-1-1 Umezono, Tsukuba, Ibaraki 305-8568, Japan

[b] National Institute of Advanced Industrial Science and Technology (AIST), Research Institute for Energy Conservation, 1-1-1 Umezono, Tsukuba, Ibaraki 305-8568, Japan

[c] AIST-UTokyo Advanced Operando-Measurement Technology Open Innovation Laboratory, 5-1-5 Kashiwanoha, Kashiwa, Chiba 277-8565, Japan

[d] Institute for Solid State Physics (ISSP), The University of Tokyo, 5-1-5 Kashiwanoha, Kashiwa, Chiba 277-8581, Japan

[e] National Institute for Materials Science, Research Center for Advanced Measurement and Characterization, 1-2-1 Sengen, Tsukuba, Ibaraki 305-0047, Japan

[f] Synchrotron Radiation Research Organization, The University of Tokyo, 7-3-1 Hongo, Bunkyo-ku, Tokyo, 113-8656, Japan

Many researchers have studied development of clean energy devices for the realization of a low-carbon society. There is a great need to develop innovative clean energy devices. In particular, high performance LIBs are important not only for electric vehicles, but also for power source of next-generation semiconductor devices for "Beyond 5G", which will enable high-speed, high-capacity data communication in the IoT society.

In response to these high societal needs, LIBs with higher performance than the current state are required. In recent years, research and development of all-solid-state LIBs have been focused for innovative improvement of the performances of LIBs. It is necessary to establish design guidelines based on fundamental science because a lot of technical issues remain unresolved in the all-solid-state LIBs. Thus, understanding the charge-discharge mechanism of LIBs is important to improve their properties.

In addition, *operando* measurement under the control of potential is important for detail and precise understanding because LIBs are high voltage device. Even deconstruction of LIB in the glovebox filled by inert Ar gas, the potential maintaining of active material is difficult. Recently Akada and Hosono *et al*. have successfully introduced *operando* soft X-ray photoelectron spectroscopy as a novel method to understand the LIBs during Li-intercalation/deintercalation process in LIB cathode and anode materials [1, 2]. These are results of photoelectron microscopy with spatially resolved information by 3D nanoESCA station at BL07LSU of SPring-8 [3]. Microspectroscopy is another important point in addition to *operando* measurement because the redox reaction by charge-discharge reaction affected by the position like a facet of an electrode material and the interfaces between the electrode materials and solid-state electrolytes. Spectroscopy with spatial resolution is important techniques.

Figure 1 shows the intensity mapping of Ni 3p and Mn 3s of $Li_xNi_{0.5}Mn_{1.5}O_4$. Here, lithium ratio is controlled by the cell using liquid electrolyte. We obtained intensity mapping. The next step is *operando* measurement by all-solid-state LIBs. We will create *oprerando* measurement system and conduct XPS mapping measurement.

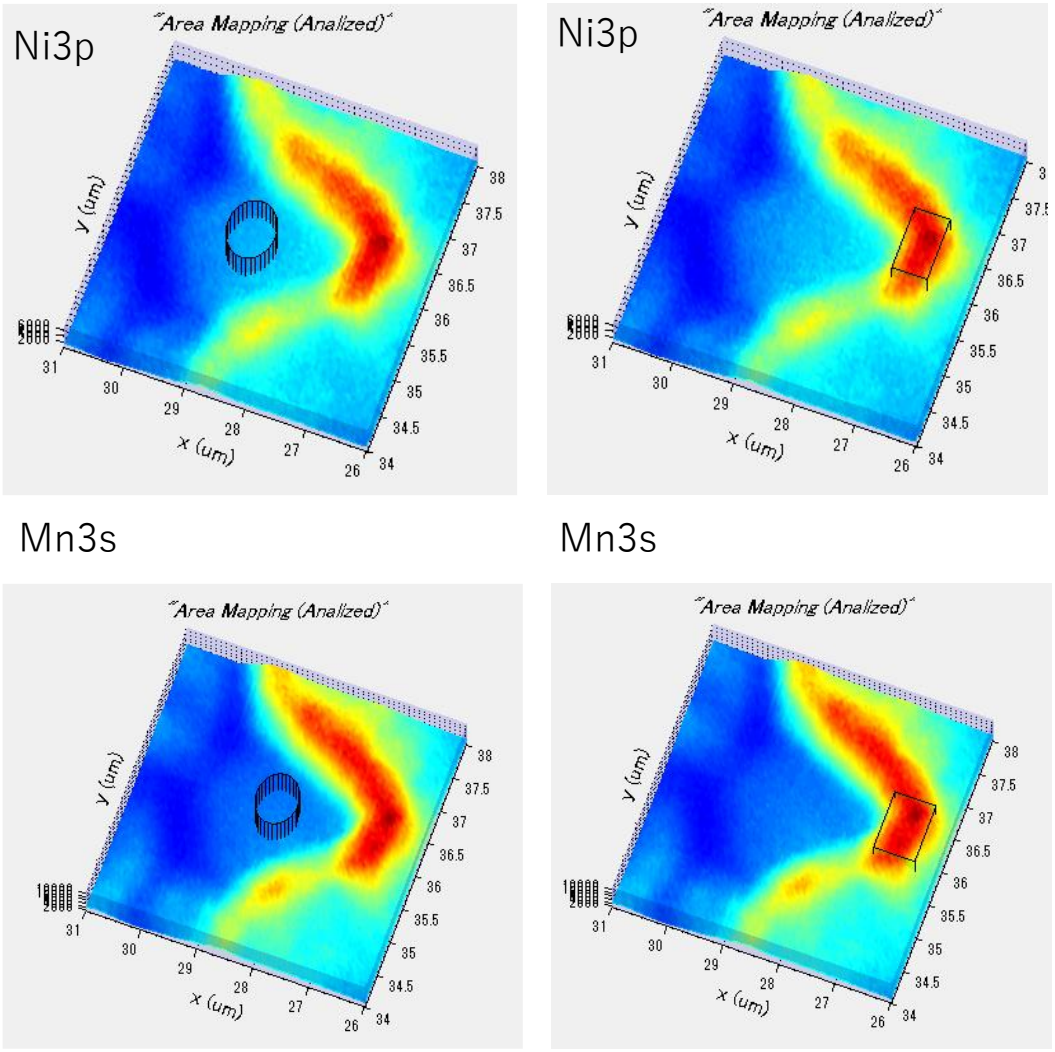

Figure 1 Intensity mapping of Ni 3p and Mn 3s of $Li_xNi_{0.5}Mn_{1.5}O_4$.

ACKNOWLEDGEMENT

This work is partially conducted on the basis of the International joint research program for innovative energy technology by Ministry of Economy, Trade and Industry, Japan.

REFERENCES

[1] K. Akada, T. Sudayama, D. Asakura, H. Kitaura, N. Nagamura, K. Horiba, M. Oshima, E. Hosono, Y. Harada, "Operando measurement of single crystalline Li4Ti5O12 with octahedral-like morphology by microscopic X-ray photoelectron spectroscopy", J. Electron Spectrosc. Relat. Phenom., 233, 64 (2019).

[2] K. Akada, T. Sudayama, D. Asakura, H. Kitaura, N. Nagamura, K. Horiba, M. Oshima, E. Hosono, Y. Harada, "Microscopic photoelectron analysis of single crystalline $LiCoO_2$ particles during the charge-discharge in an all solid-state lithium ion battery", *Scientific Reports*, *9*, 12452 (2019).

[3] K. Horiba, Y. Nakamura, N. Nagamura, S. Toyoda, H. Kumigashira, M. Oshima, K. Amemiya, Y. Senba, H. Ohashi, Scanning photoelectron microscope for nanoscale three-dimensional spatial-resolved electron spectroscopy for chemical analysis. *Rev. Sci. Instrum.* 82, 113701 (2011).

Resonant inelastic soft x-ray diffraction of nanoparticles

J. Miyawaki[1], T. Yachi[2], S. Maki[2], K. Kanie[2] and Y. Harada[1]

[1]*Institute for Solid State Physics, The University of Tokyo*
[2]*Institute of Multidisciplinary Research for Advanced Materials, Tohoku University*

The excitation energy dependence of soft X-ray emission spectra (XES) was first measured for TiN in 1988 [1]. Four years later, Ma *et al.* proposed that the excitation energy dependence could be interpreted by the theory of resonant inelastic X-ray scattering (RIXS), and band dispersions of electronic state were observed [2]. This indicates that the absorption- and emission-processes are described by a single scattering theory, and the momentum is conserved during that process. In other words, when a core electron with momentum $\boldsymbol{k}$ is excited to the conduction band and an electron at the valence band is decayed to the core hole, the emissions from the different cores could interfere with each other, and Bragg-like diffraction results in the emissions of the same momentum $\boldsymbol{k}$. These facts suggest that a more general Bragg's law, $\boldsymbol{q}_{\mathrm{in}} = \boldsymbol{q}_{\mathrm{out}} + \boldsymbol{k}_{\mathrm{h}} - \boldsymbol{k}_{\mathrm{e}} + \boldsymbol{G}$ is valid, in addition to the energy conservation law in RIXS, $h\nu_{\mathrm{in}} = h\nu_{\mathrm{out}} + E_{\mathrm{h}} - E_{\mathrm{e}}$, where $h\nu_{\mathrm{in}}$ ($\boldsymbol{q}_{\mathrm{in}}$) and $h\nu_{\mathrm{out}}$ ($\boldsymbol{q}_{\mathrm{out}}$) are the energy (momentum) of the incident and scattered X-ray, E_{h} ($\boldsymbol{k}_{\mathrm{h}}$) and E_{e} ($\boldsymbol{k}_{\mathrm{e}}$) are the energy (momentum) of the hole in the valence band and the electron in the conduction band at the final state, and $\boldsymbol{G}$ is the reciprocal vector of the crystal. When the excitation and scattered energies are the same, the momentum conservation law gives $\boldsymbol{q}_{\mathrm{in}} = \boldsymbol{q}_{\mathrm{out}} + \boldsymbol{G}$, which is widely accepted as Brass's law. The more general Bragg's law $\boldsymbol{q}_{\mathrm{in}} = \boldsymbol{q}_{\mathrm{out}} + \boldsymbol{k}_{\mathrm{h}} - \boldsymbol{k}_{\mathrm{e}} + \boldsymbol{G}$ (the momentum conservation law in RIXS) has been validated by the RIXS studies of the band dispersions in SiC [3], graphite, diamond [4], Si [5], and LiBC [6]. Recent observations of the dispersions of orbitons, magnons, and phonons also confirmed the validity of the principle [7].

In the above discussion, the Bragg diffraction and RIXS were treated as independent processes. However, if the Bragg diffraction and RIXS occur simultaneously, the intensity of RIXS is expected to increase assisted by the Bragg diffraction. We named this method resonant inelastic X-ray diffraction (RIXD). In the case of nanoparticles, the momentum dispersion of the elementary excitations is small, and the diffraction from the nanoparticles, that is, small angle X-ray scattering (SAXS), is expected to increase the intensity of RIXS. Therefore, we measured soft X-ray SAXS of FePt nanoparticles by a RIXS spectrometer and discussed the feasibility of RIXD by comparing the SAXS profile obtained by the elastic scattering and the momentum dependence of RIXS.

The measurement of SAXS and RIXD were conducted at HORNET end-station of SPring-8 BL07LUS using θ-2θ scan system. In this scan system, RIXS spectra can be measured at an arbitrary scattering angle 2θ in the range between 45° and 135°, and SAXS and RIXD profiles can obtained from momentum dependence of the intensity of the elastic and inelastic peaks, respectively. The measured sample was FePt nanoparticles. The average particle size and standard deviation were 2.7 nm and 0.37 nm, respectively.

Figure 1 shows the RIXS spectra of the FePt nanoparticle measured at 708.1 eV, which is the peak top of Fe L_3-edge X-ray absorption spectra. A SAXS profile was obtained by integrating the intensity of the elastic peak (Fig. 2). A peak was observed in the SAXS profile at around θ=31°. In the hard X-ray SAXS, the SAXS profile is observed at small angles (typically 0.1–10°), but in the case of soft X-ray SAXS, SAXS profile is observed at larger angle, since the wave length of the soft X-ray is longer than that of hard X-ray. The obtained profile is well reproduced by a simulation with the particle size of 2.73 nm and standard deviation of 0.37 nm, and thus the obtained $\boldsymbol{q}$-dependence of the elastic peak was confirmed to be SAXS. Furthermore, the momentum dependence of the inelastic scattering indicated by a1, a2, a3, and a123 in Fig. 1 was calculated, and the increase of the intensity of

a3 peak was found at the same scattering angle of the SAXS peak, indicating the observation of RIXD. In the future, we will measure the particle size and incident energy dependences of various samples to further establish RIXD and elucidate its mechanism.

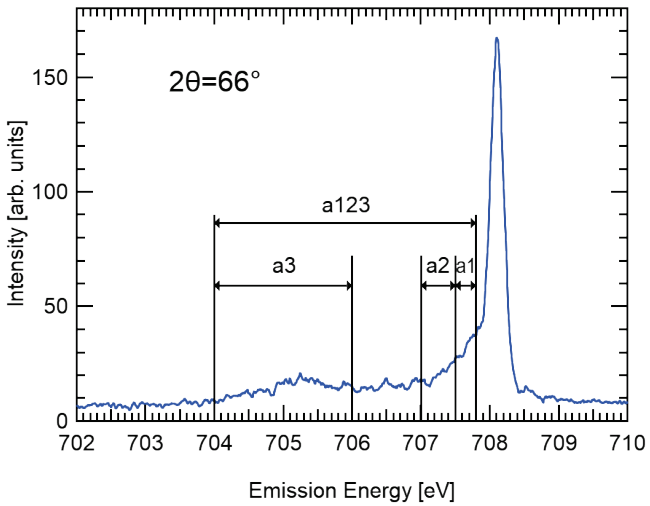

Fig. 1 RIXS spectra of FePt nanoparticle measured at 708.1 eV and 2θ=66°.

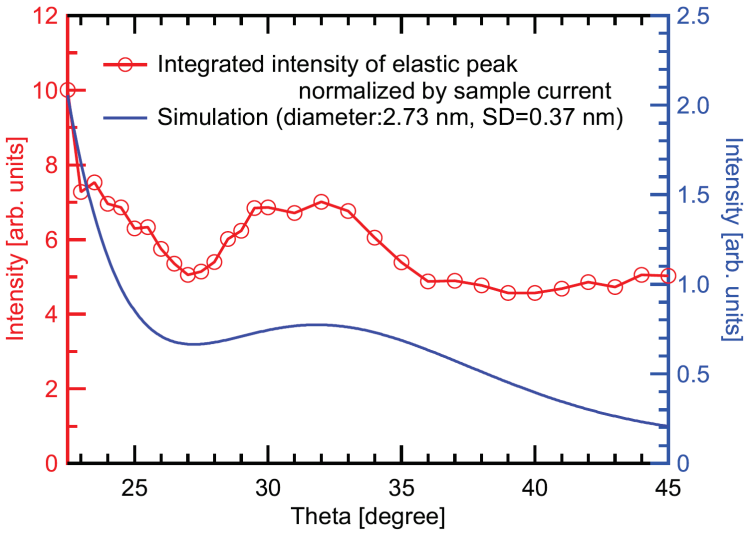

Fig. 2 The momentum dependence of the elastic peak intensity in RIXS spectra of FePt nanoparticle. Red circle and blue line correspond to the experimental result and simulation, respectively.

REFERENCES

[1] J. E. Rubensson, *et al.*, Phys. Rev. Lett. **60**, 1759 (1988).
[2] Y. Ma, *et al.*, Phys. Rev. Lett. **69**, 2598 (1992).
[3] J. Luning, *et al.*, Phys. Rev. B **56**, 13147 (1997).
[4] A. V. Sokolov, *et al.*, J. Phys. Condes. Matter **15**, 2081 (2003).
[5] A. V. Sokolov, *et al.*, J. Electron Spectrosc. **137**, 591 (2004).
[6] P. F. Karimov, *et al.*, J. Phys. Condens. Matter **16**, 5137 (2004).
[7] L. J. P. Ament, *et al.*, Rev. Mod. Phys. **83**, 705 (2011).

Development of X-ray Polarization Precession Spectroscopy

J. Miyawaki, Y. Hirata[†], K. Yamagami[‡], I. Matsuda, and Y. Harada

Institute for Solid State Physics, The University of Tokyo

Magnonics is a next-generation technology, that utilizes a collective excitation of electron spin (magnon or spin wave), and is an alternative technology to electronics, which utilizes electrons for information transfer and computation. Compared with electron- and spin-based electronics and spintronics, magnonics does not suffer from Joule heat. Magnon has longer mean free path, which is advantageous for long-distance information transfer. Magnon has a wave nature, which offers a possibility of quantum computation. Thus, researchers are trying to use high-frequency terahertz magnons to speed up magnonic devices and observe magnons injected to magnonics materials to understand the operating mechanism of devices [1–6].

For the magnon observation, ferromagnetic resonance (FMR), Brillouin light scattering (BLS), inelastic neutron scattering (INS), spin-polarized electron energy loss spectroscopy (SPEELS), and time-resolved spectroscopy have mainly been used. FMR and BLS observe magnons only at $\boldsymbol{q}\approx 0\ \mathrm{nm}^{-1}$ and cannot observe propagating magnons at $\boldsymbol{q}\neq 0\ \mathrm{nm}^{-1}$. INS and SPEELS can observe at larger $\boldsymbol{q}$, but INS cannot observe higher energy magnons and require large sample volume, and SPEELS is surface sensitive. Therefore, INS and SPEELS is not suitable for *operando* experiments. Thus, a new technique to observe propagating magnons in *operando* condition has been explored. In this study, we developed X-ray polarization precession spectroscopy (XPPS), which is a new method to observe dispersion of magnons by X-ray with high energy resolution to understand the properties of magnon in devices.

XPPS was proposed as a new technique to measure the frequency of spin waves by observing a rotational/angular Doppler effect in the polarization of scattered X-ray induced by spin waves in the sample via magnetic linear dichroism [7]. Since magnetic linear dichroism is employed in XPPS, resonant condition is required to measure XPPS signal. The measurement principle and experimental setup are shown in Fig. 1(a). The scattered X-ray is irradiated to a multilayer polarizer, the intensity of the reflected X-ray is spatially resolved by CCD, and the period of the rotation of the polarization can be detected. The energy resolution of XPPS reaches 50 GHz (0.2 meV), which is very high energy resolution for X-ray based spectroscopy to obtain the energy of magnons. Thus, XPPS has a promising technique for *operando* experiment of magnonic devices.

XPPS experiments were conducted at free-port end-station of SPring-8 BL07LSU using superconducting magnet chamber equipped with a polarization analyser (Fig. 2). The linear vertical polarization was used for the incident X-ray, and the multilayer polarizer of the polarization analyser was positioned orthogonal to the electronic vector of the incident X-ray. The position dependence of the reflected X-ray intensity was measured by CCD.

Figure 3 shows a XPPS result of $Y_3Fe_5O_{12}$ (YIG) and Pt. 705.0 eV and 709.6 eV correspond pre-edge and the peak-top of Fe L_3-edge X-ray absorption spectra of YIG. YIG showed the difference between pre- and post-edge of Fe L_3-edge, while Pt, which is non-magnetic, showed no difference. In YIG, the difference spectra showed the intensity modulation with a period of ~100 μm. This period corresponds the magnon energy of ~5.5 meV, which matches the energy obtained by inelastic neutron scatterings [8]. Thus, we succeeded in detecting XPPS signal and extracting the energy of magnon.

[†]Present Address: *Department of Applied Physics, National Defense Academy*

[‡]Present Address: *Quantum Materials Science Unit, Okinawa Institute of Science and Technology Graduate University*

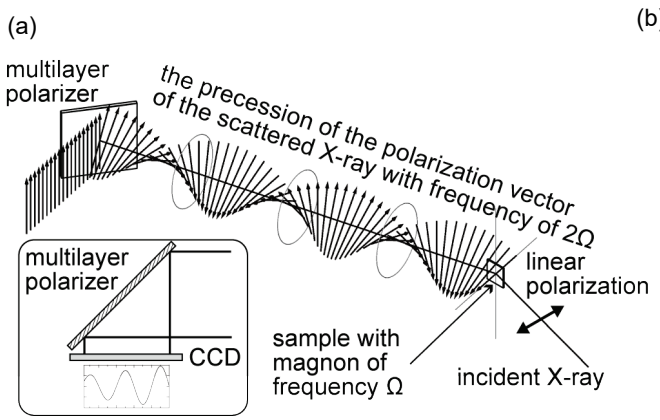

FIG. 1. (a) The measurement principle and (b) experimental setup of XPPS. Linearly polarized X-ray of a resonant energy is irradiated to a sample that possesses a spin wave of frequency Ω, and the precessional motion of frequency 2Ω is induced to the polarization vector of the scattered X-ray. The multilayer polarizer reflects the vertically polarized component of the scattered X-ray, and thus spatially resolved reflection intensity gives the intensity modulation due to the precession in the scattered X-ray.

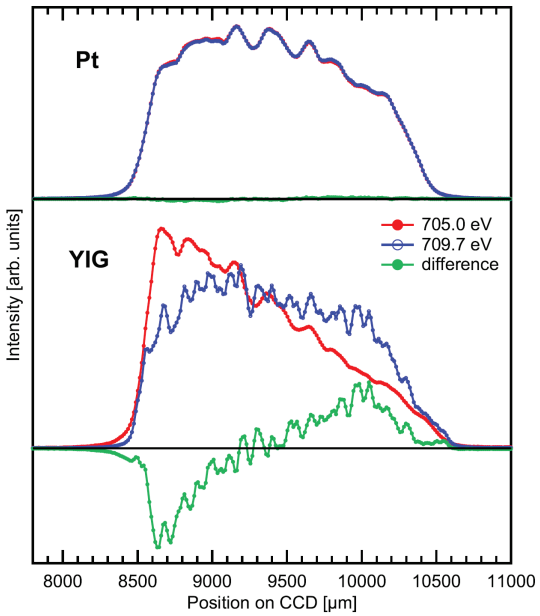

FIG. 2. XPPS of Pt and YIG at Fe L_3-edge. Spatially resolved reflection intensity of the scattered X-ray from the multilayer polarizer was measured at pre- (red) and post-edge (blue) of Fe L_3-edge. Since the intensity profiles by the pre-edge excitation has no resonant effect, the signal can be regarded as a background affected by the surface of the sample and the polarizer.

REFERENCES

[1] S. Neusser *et al.*, Adv. Mater. **21**, 2927 (2009).
[2] Y. Kajiwara *et al.*, Nature **464**, 262 (2010).
[3] V. V. Kruglyak *et al.*, J. Phys. D: Appl. Phys. **43**, 264001 (2010).
[4] A. V. Chumak *et al.*, Nat. Phys. **11**, 453 (2015).
[5] H. Yu *et al.*, Nat. Comm. **7**, 11255 (2016).
[6] C. Du *et al.*, Science **357**, 195 (2017).
[7] R. Röhlsberger, Phys. Rev. Lett. **112**, 117205 (2014).
[8] J. S. Plant, J. Phys. C: solid State Phys. 10 4805 (1977).

Resonant Inelastic Soft X-ray Scattering of $Y_3Fe_5O_{12}$

J. Miyawaki and Y. Harada

Institute for Solid State Physics, The University of Tokyo

Further development of the information society requires innovation in information technology, and faster, compact, and low energy-consumption devices have been pursued. One of the next generation technologies to realize this goal is magnonics, which utilizes magnons (spin waves), that is, a collective excitation of spins instead of electrons for the transmission and processing of information. Since no electronic current is induced when the magnon propagates through the magnetic material, there is no energy dissipation due to Joule heating. There is a very wide frequency of magnons known, and if higher frequency magnons can be used, ultra-fast devices could be created. Currently, fundamental research is in progress to realize actual devices. Higher-frequency terahertz magnons have been investigated to speed up the devices, and the magnons injected in the magnonic materials has been investigated to understand the behaviour of the magnons in the device and efficiently utilize magnons. Magnons have been observed by using ferromagnetic resonance, Brillouin light scattering, inelastic neutron scattering, spin-polarized electron energy loss spectroscopy, and time-resolved spectroscopy. However, these experimental methods are not suitable for observing high-energy magnons at larger $\boldsymbol{q}$, and the development of a new method to observe a propagating magnons is urgently needed. In this study, we focus on X-ray spectroscopy for the observation of the high-frequency propagating magnons and apply resonant inelastic soft X-ray scattering (SX-RIXS) to magnonic materials to elucidate the behaviour of the high-energy magnon.

A $Y_3Fe_5O_{12}$(YIG)(111) single crystal was measured, which is very promising for magnonics due to its very low damping and long mean free path of magnon. X-ray absorption spectra (XAS) and RIXS were measured at HORNET end-station of SPring-8 BL07LSU. All the measurements were performed at room temperature. XAS was measured in partial fluorescence yield mode using a silicon drift detector, and Fe L_3-edge inverse partial fluorescence yield (IPFY) XAS was obtained from O K emission. The energy resolution of RIXS at Fe L-edge was set at 175 meV. A momentum-resolved RIXS was obtained by θ-2θ scan of 2θ=45–135° and 9° step. During the θ-2θ scan, an elastic peak was measured at each 2θ from Au with σ polarization. For RIXS of YIG, π polarization was used.

Fe L_3-edge XAS of YIG is shown in Fig. 1(a). The spectral shape of XAS is good agreement of YIG, having two characters of Fe^{3+} in octahedral (O_h) and tetrahedral (T_d) symmetry [1,2]. Figure 1(b) shows the incident photon energy dependence of RIXS spectra of YIG at θ=45° and 2θ=90°. In addition to *dd* excitations at ~1.3 eV and ~1.8 eV, which mainly originate from O_h Fe^{3+}, *dd* excitations around 2.5 eV were observed, which would be assigned for T_d Fe^{3+}. The peak width at around loss energy of 0 eV is clearly larger than the energy resolution, indicating that there is a contribution of inelastic scattering. For the momentum-resolved RIXS, #7 (710.1 eV) was chosen since the contribution of inelastic scattering was largest among the measured energies. Figure 2 shows RIXS spectra near the elastic peak obtained by θ-2θ scan. The peak at each 2θ was analyzed by a peak fitting of two gaussian profiles: One is the elastic peak, ant the other is for inelastic scattering. The experimental results (red circles) were well reproduced by the two gaussian profiles. Since the energy resolution was set at 175 meV, it was difficult to identify low energy magnons below 100 meV. The inelastic peaks (green lines) at ~110 meV showed a weak dispersion. The energy scale of the inelastic peaks ranges from ~110 meV to ~130 meV. Inelastic neutron scattering measurements and a theoretical calculation revealed that YIG possessed magnon dispersions up to 100 meV [3,4]. The energy scale of the observed dispersion is higher than

that of magnons of YIG, indicating that the observed inelastic scattering would be assigned to bimagnon. The identification of the bimagnon requires a complete picture of the magnetic excitations in YIG. Further analysis will be conducted to understand RIXS spectra and the dispersion of the inelastic peak near the elastic peak.

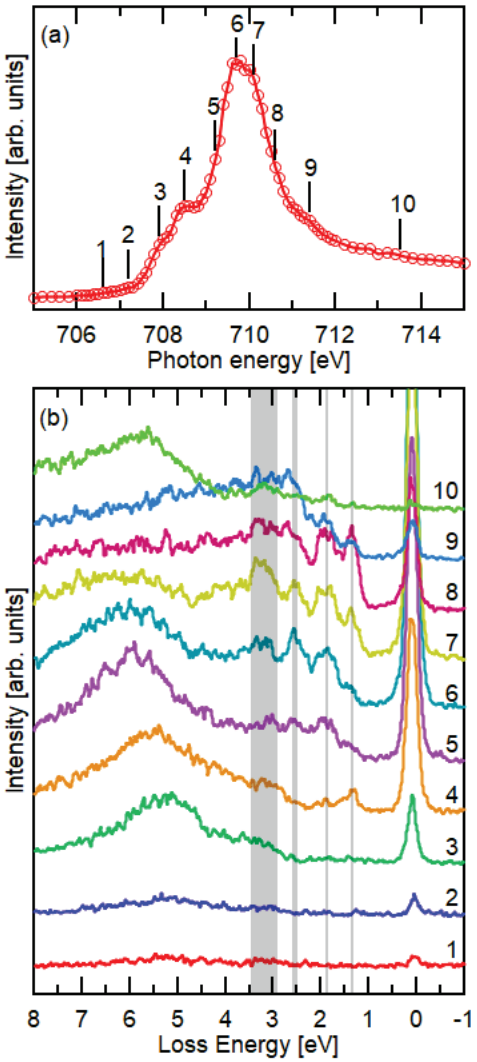

FIG. 1. Fe L_3-edge (a) XAS and (b) RIXS spectra of YIG(111) single crystal. The numbers labeled in (a) indicate the incident photon energies used to measure RIXS spectra in (b).

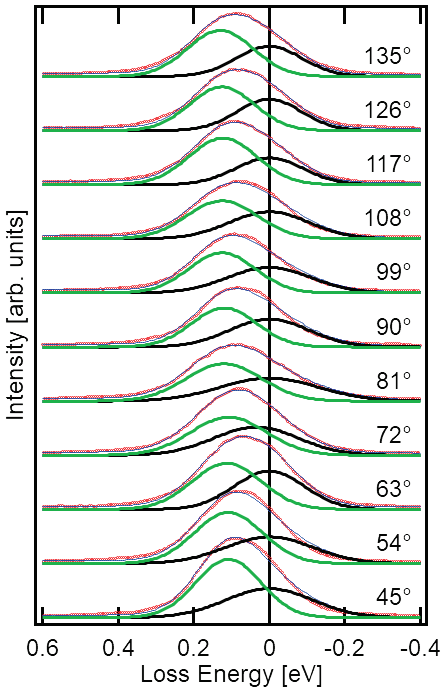

FIG. 2. Fe L_3-edge RIXS spectra of YIG measured at different θ-2θ angles. Red circles are experimental results, and black, green, and blue lines correspond to the fitting results of elastic peaks, inelastic peaks, and sum of two peaks and background. Angles labeled on the spectra indicate 2θ angle.

REFERENCES

[1] F. M. F. de Groot *et al.*, J. Phys. Chem. B **109**, 20761 (2005).
[2] H. B. Vasili *et al.*, Phys. Rev. B **96**, 014433 (2017).
[3] J. S. Plant, J. Phys. C: Solid State Phys. **10**, 4805 (1977).
[4] A. J. Princep *et al.*, npj Quantum Materials **2**, 63 (2017).

Development of Coherent Soft X-ray Diffraction Imaging Technique for Observation of Ultra-fast Magnetic Dynamics

Yuichi Yamasaki[1,2,3], Kohei Yamamoto[4,5], Yuichi Yokoyama[1,6], Yasuyuki Hirata[4], Hiroki Wadati4,7, and Taka-hisa Arima[3,8]

[1]*Research and Services Division of Materials Data and Integrated System (MaDIS), National Institute for Materials Science (NIMS)*

[2]*PRESTO, Japan Science and Technology Agency (JST)*

[3]*RIKEN Center for Emergent Matter Science (CEMS)*

[4]*The Institute for Solid State Physics, University of Tokyo*

[5]*Department of Materials Molecular Science, Institute for Molecular Science*

[6] *Japan Synchrotron Radiation Institute (JASRI)*

[7]*Graduate School of Material Science, University of Hyogo*

[8]*Department of Advanced Materials Science, University of Tokyo*

Introduction:

In recent years, topological magnetic structures, such as magnetic skyrmions, have been actively studied. Magnetic skyrmions, nanometer-scale vortex-like magnetic structures, can be controlled by external stimuli, such as electric field and pressure, and thus are expected to be a promising candidate for next-generation spintronics device materials. To understand the dynamics of magnetic skyrmions, it is important to observe them at high spatial and temporal resolutions. Resonant soft X-ray scattering is also known to be a suitable technique for observing such magnetic skyrmion dynamics because of its high sensitivity in detecting spin polarization [1-3]. Therefore, in the present study, we have developed a diffractometer of small-angle resonant soft x-ray magnetic scattering to observe topological magnetic textures in the undulator beamline BL07LSU, SPring-8. The apparatus is equipped with a vacuum chamber having a background pressure of $< 1 \times 10^{-5}$ Pa, a CCD camera (2048x2048 pixel, Princeton Instrument), a direct beam catcher, and a sample holder. To observe transmitted soft X-ray scattering, we prepared thin plate sample thinned by FIB method or magnetic thin films fabricated on Si_3N_4 substrates.

Results:

We tried to measure resonant soft X-ray small-angle scattering from magnetic multilayer films and multiferroic $BiFeO_3$ lamellas. The magnetic films were fabricated with thickness of several tens nano-meters and with different compositions, $Ta_5[Pt_3CoTa_2]_{10}$, $Ta_5[Pt_3Co_{1.2}Ta_2]_{10}$, $[Co/Pt]_{15}$, and $[Co/Pt]_6$. The thickness of the samples were sufficiently thin for soft X-rays to penetrate, and absorption measurements confirmed the presence of the sample. A pinhole with a diameter of several micro-meters was placed on the thin film sample to irradiate a circularly shaped soft X-ray to the sample. Figure 1 shows resonant soft x-ray diffraction image

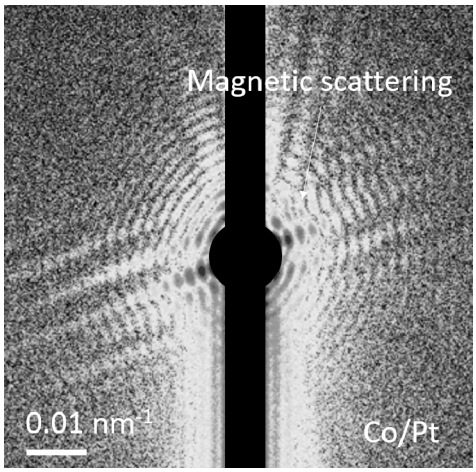

Figure 1: Diffraction pattern from Co/Pt multilayer thin film.

from $[Co/Pt]_6$ observed at the Co *L*-edge resonance energy. However, the scattering intensity was weak and the diffraction pattern was not sufficiently accurate to reconstruct the real space image from the obtained coherent diffraction pattern. This is probably due to the small perpendicular magnetization component in the magnetic multilayer film. The other samples were damaged during the experiment and no significant data could be obtained.

The multiferroic iron oxide BiFeO3 is known to have a ferroelectric polarization, which gives rise a long-period cycloidal magnetic structure with a wave-length of 62 nm. The competition between ferromagnetic interaction and the Dzyaloshinskii-Moriya interactions between the Fe ions results in the non-collinear magnetic structure. We performed small-angle scattering experiments at the *L*-absorption edge of Fe on the lamella samples to observe the magnetic scattering derived from the cycloid magnetic structure. Figure 2 shows diffraction patterns from the lamella sample of $BiFeO_3$. Magnetic scattering was observed with superimposing on the concentric diffraction pattern from pinhole. In the previous study, six magnetic scatters were observed for the (110) surface sample, whereas in the present experiment, magnetic scattering was found to be broad in the azimuthal direction. It is assumed that the magnetic structure may be different due to the influence of FIB processing. To confirm whether the magnetic scattering observed in the lamella sample is intrinsic or not, a follow-up experiment comparing with other FIB processed samples is required in the future.

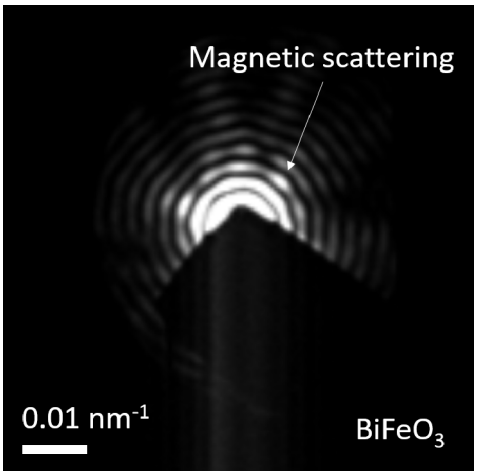

Figure 2: Diffraction pattern from BiFeO3 lamella sample.

Conclusion:

In this study, we developed the equipment for resonant soft x-ray small angle scattering and succeeded in observing the magnetic scattering from the magnetic thin films and multiferroic $BiFeO_3$ lamella sample. As a next step, we aim to observe temporal variations of the magnetic structure in real space by combining the coherent soft x-ray diffraction imaging technique with time-resolved pump-probe measurement.

References

[1] "Dynamical Process of Skyrmion-Helical Magnetic Transformation in Chiral-Lattice Magnet FeGe as Probed by Small-Angle Resonant Soft X-ray Scattering", Y. Yamasaki, D. Morikawa, T. Honda, H. Nakao, Y. Murakami, N. Kanazawa, M. Kawasaki, T. Arima, and Y. Tokura, Phys. Rev. B 92, 220421(R) (2015)

[2] "Coherent Resonant Soft X-ray Scattering Study of Magnetic Textures in FeGe", Victor Ukleev, Y. Yamasaki, Daisuke Morikawa, Naoya Kanazawa, Yoshihiro Okamura, Hironori Nakao, Yoshinori Tokura, Taka-hisa Arima, Quantum Beam Science. 2 [1] 3 (2018)

[3] "Element-specific soft x-ray spectroscopy, scattering, and imaging studies of the skyrmion-hosting compound $Co_8Zn_8Mn_4$", V. Ukleev, Y. Yamasaki, D. Morikawa, K. Karube, K. Shibata, Y. Tokunaga, Y. Okamura, K. Amemiya, M. Valvidares, H. Nakao, Y. Taguchi, Y. Tokura, T. Arima, Physical Review B. 99 [14] 144408 (2019)

REVERSIBLE AND IRREVERSIBLE ANIONIC REDOX FOR HIGH-CAPACITY BATTERY MATERIALS

Naoaki Yabuuchi[1] and Daisuke Asakura[2]
[1]*Department of Chemistry and Life Science, Yokohama National University*
[2]*Research Institute for Energy Conservation, National Institute of Advanced Industrial Science and Technology*

To realize the sustainable energy development, the electrification of automobiles has progressed in the past several years. This movement reduces the dependence on fossil fuels used for internal combustion engine technology together with accelerating the use of renewable energy, including solar, wind, and biomass. In the past three decades, technology of rechargeable lithium batteries, *i.e.*, lithium-ion batteries, has been highly sophisticated, and currently Ni-based layered materials dominate the market of lithium-ion batteries for electric vehicles. However, further increase in energy density of lithium-ion batteries is required to extend cruising distances of electric vehicles. In the past few years, many lithium-excess metal oxides with layered and disordered rocksalt structures, Li_2MnO_3-based electrode materials have been studied as potential high capacity electrode materials. However, Mn ions in Li_2MnO_3 ($Li_{1.33}Mn_{0.67}O_2$) cannot be oxidized beyond the tetravalent limit, and therefore, anionic species, oxide ions, donate electrons on Li extraction. Nevertheless, low reversibility of anionic redox for pure Li_2MnO_3 is experimentally observed, leading to insufficient reversibility as electrode materials. To increase in the reversibility of anionic redox, the substitution of metal ions with higher ionic characters with oxide ions, for instance, Nb^{5+} (Li_3NbO_4) and Ti^{4+} (Li_2TiO_3), has been proposed. For the Li-excess metal oxides, the charge compensation process on Li extraction is achieved by electron donation from oxide ions, but detailed reaction mechanisms remain as a debatable subject, *e.g.*, dimerization of oxygen and formation of holes in oxygen.

In this study, a binary system of Li_2TiO_3–$LiMnO_2$ is examined as electrode materials for Li storage applications, and its reaction mechanism is studied by resonant inelastic X-ray scattering (RIXS) study. In this binary system, nanosized $Li_{7/6}Ti_{1/3}Mn_{1/2}O_2$ has been prepared by mechanical milling from a mixture of Li_2TiO_3 and $LiMnO_2$.[1] TEM observation reveals that particle size is reduced to 5 – 20 nm, and these nanosize particles are agglomerated for each other, forming secondary particles with diameters of 50 – 200 nm after milling. Nanosize $Li_{7/6}Ti_{1/3}Mn_{1/2}O_2$ delivers large reversible capacities in Li cells, and an initial discharge capacity reaches 295 mA h g^{-1} even at room temperature (Figure 1). Charge compensation processes for nanosize $Li_{7/6-y}Ti_{1/3}Mn_{1/2}O_2$ were further examined by O K-edge RIXS study (Figure 2a). From the data of Mn K-edge and L-edge XAS study, Mn oxidation from a trivalent to tetravalent state is evidenced on charge for the slope region of 3 – 4 V [1], but no oxidation of Mn ions is

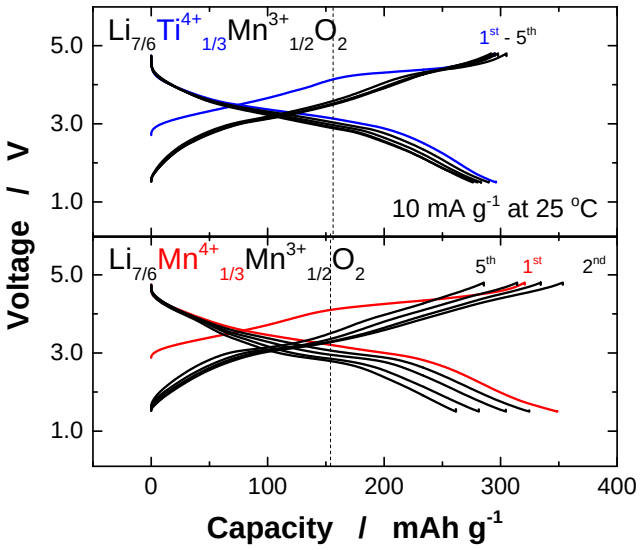

Fig. 1. Charge/discharge curves of nanosize $Li_{7/6}Ti_{1/3}Mn_{1/2}O_2$ at room temperature. The data of $Li_{7/6}Mn^{4+}{}_{1/3}Mn^{3+}{}_{1/2}O_2$ is also shown for comparison.

found at the plateau region. O K-edge RIXS spectra clearly reveals that a new peak is observed after charge at 8 eV, which suggests that charge compensation is achieved by the donation of electron from oxide ions at the plateau region, and the formation of holes by electrochemical oxidation.[2]

To further clarify the role of Ti ions on anionic redox reversibility, a binary system of Li_2MnO_3-$LiMnO_2$ is also prepared and tested as electrode materials. $Li_{7/6}Mn^{4+}{}_{1/3}Mn^{3+}{}_{1/2}O^2$ was also successfully prepared by mechanical milling from the mixture of Li_2MnO_3 and $LiMnO_2$. This phase is metastable containing Mn^{4+} and Mn^{3+} ions and cannot be obtained by a conventional calcination process. Charge/discharge curves of nanosize $Li_{7/6}Mn^{4+}{}_{1/3}Mn^{3+}{}_{1/2}O_2$ in a Li cell are also shown in Figure 1. An observed initial discharge capacity reaches 350 mA h g^{-1}, which is larger than that of $Li_{7/6}Ti_{1/3}Mn_{1/2}O_2$. Nevertheless, cyclability is insufficient as electrode materials, and a reversible capacity of *ca*. 100 mA h g^{-1} is lost on initial five cycles. Much better capacity retention is achieved for $Li_{7/6}Ti_{1/3}Mn_{1/2}O_2$. Reversibility of anionic redox for $Li_{7/6}Mn^{4+}{}_{1/3}Mn^{3+}{}_{1/2}O^2$ has been also examined by RIXS study as shown in Figure 2b. A similar peak with $Li_{7/6}Ti_{1/3}Mn_{1/2}O_2$ at 8 eV is observed for $Li_{7/6}Mn^{4+}{}_{1/3}Mn^{3+}{}_{1/2}O^2$ after charge. However, intensity of the peak is much higher for the $Li_{7/6}Ti_{1/3}Mn_{1/2}O_2$, indicating that oxygen redox chemistry is clearly stable for the Ti-substituted sample. This result directly supports the role of Ti^{4+} ions, which are effective to stabilize anionic redox associated with the high ionic character and donation of electron to oxide ions.

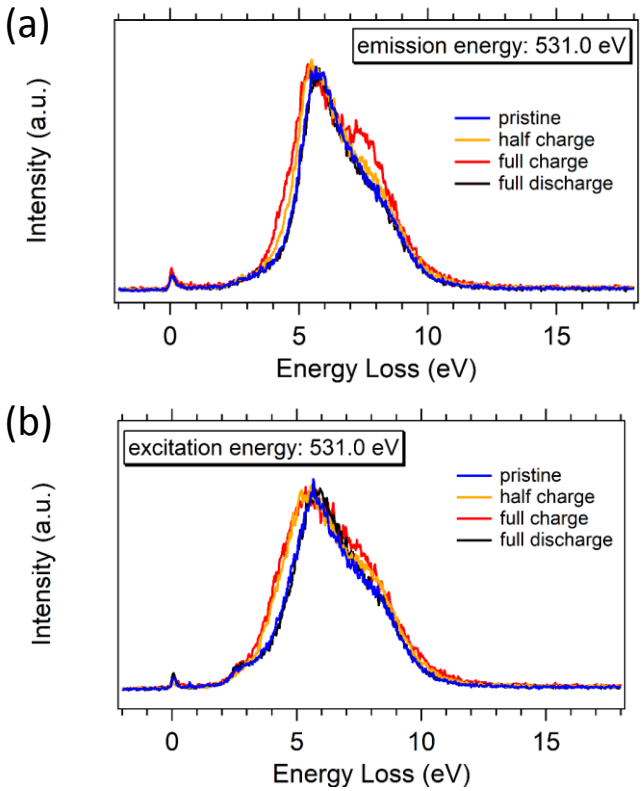

Fig. 2. Comparison of changes in RIXS spectra for nanosize $Li_{7/6}Ti_{1/3}Mn_{1/2}O_2$ and $Li_{7/6}Mn^{4+}{}_{1/3}Mn^{3+}{}_{1/2}O_2$ on charge/discharge processes.

These findings open a new direction to design high-capacity positive electrode materials with highly reversible electrochemistry on the basis of anionic redox. Further optimization of chemistries, compositions, and particle sizes on these electrode materials contributes the development of advanced high-energy rechargeable Li batteries in the future.

REFERENCES

[1] Y. Kobayashi, M. Sawamura, S. Kondo, M. Harada, Y. Noda, M. Nakayama, S. Kobayakawa, W. Zhao 1, A. Nakao, A.Yasui, H. B.Rajendra, K.Yamanaka, T.Ohta, and chi, Materials Today, in-press

[2] T. Sudayama, K. Uehara, T. Mukai, D. Asakura, X.-M. Shi, A. Tsuchimoto, B. Mortemard de Boisse, T. Shimada, E. Watanabe, Y. Harada, M. Nakayama, M. Okubo and A. Yamada, *Energy & Environmental Sciences*, in-press

ELECTRONIC STATE OF INTERMEDIATE WATER IN BIOCOMPATIBLE POLYMERS INVESTIGATED BY XAS AND XES

Koichi Ozaki[1], Jumpei Yahiro[1], Masaru Nakada[1], Masahiro Kunisu[1],
Kosuke Yamazoe[2], Jun Miyawaki[2] and Yoshihisa Harada[2]
[1]*Toray Research Center, Inc.*,
[2]*The Institute for Solid State Physics, The University of Tokyo*

Introduction

Poly (vinyl-pyrrolidone) (PVP) and Poly (ethylene-glycol) (PEG) have been widely used for various biomedical applications because of their excellent biocompatibility. Biocompatibility is one of the important factors for polymers used for biomedical applications. It is considered that adsorbed water on the polymer surface contributes to expression of biocompatibility. Water molecules existing near the biocompatible polymer could be classified into three types; free water, intermediate water and non-freezing water [1]. In particular, the intermediate water has an important role to control the biocompatibility of polymers. However, the local structural and dynamical properties of intermediate water are not well understood yet. It has been reported that water molecules confined in a polyelectrolyte brush form characteristic local hydrogen-bonded structure [2]. Based on this result, water molecules in the close vicinity of a biocompatible polymer are expected to form a specific hydrogen-bonded structure to express biocompatibility. In order to reveal the role of hydrogen-bonded structure of water on biocompatibility, it is necessary to obtain accurate information about the hydrogen-bonded structure of those water molecules. In this study, we examine the hydrogen-bonded structure of water molecules hydrating PVP and PEG molecules in detail using X-ray absorption spectroscopy (XAS) and X-ray emission spectroscopy (XES).

Experimental

The PVP (M_w=4000-5000) and PEG (M_w=3350 and 20000) were purchased from Sigma-Aldrich. PVP and PEG aqueous solutions at different concentrations were prepared as measurement samples. Absolutely dry PVP (dry-PVP) and PEG (dry-PEG) were also measured. O 1s XAS and XES measurements were performed at the BL07LSU HORNET station in SPring-8. The measurement of the polymer aqueous solution was performed using a solution cell under ambient pressure by circulating the aqueous solution. The dry samples were mounted on a Cu sample plate and measured in a high vacuum condition.

Results and Discussion

Figure 1 shows the O 1s XES spectra of dry-PEG (M_w=20000) measured at various scan rates of the Cu plate. XES measurements were performed at the excitation energy of 537 eV. A broad peak around 527 eV was observed for the XES spectra with the scan rate of 0.16 and 0 μm/s. The shape of the XES spectra changed gradually with increasing the scan rate, indicating the presence of X-ray induced degradation of the polymer during the XES measurement at lower scan rate. Since the shapes of the XES spectra above the 5.0 μm/s scan rate were almost the same, we set the scan rate of 5.0 μm /s to obtain the XES spectra of the dry-PVP and dry-PEG samples.

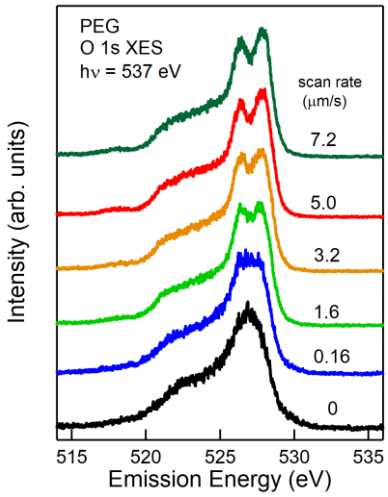

Figure 1. O 1s XES spectra of dry-PEG with various scan rate: 7.2, 5.0, 3.2, 1.6, 0.16 and 0 (μm /s).

Figure 2(a) depicts O 1s XES spectra of PVP aqueous solution at the excitation energy of 550 eV. XES measurements were performed with a flow rate of 5.0 ml/s to avoid the accumulation of radiation damage.

Two $1b_1$-derived peaks ($1b_1$' and $1b_1$'') were observed in the XES spectra of pure water [3]. The raw XES spectra for aqueous solutions contain X-ray emission signals from oxygens both in water molecules and in PVP. Subtracting the polymer component, we can obtain the signal from water molecules. In order to remove the PVP polymer contribution from the raw XES spectra, we focused on the energy range below 522 eV. In this region, the spectral intensity seems to well reflect the relative contributions of water and polymer. Thus each contribution was estimated by performing least-squares fit of the XES spectrum of dry-PVP and pure water in the energy range below 522 eV. The results after subtraction of the polymer contribution are shown in the bottom of Figure 2(a). It was found that the $1b_1$' peak is dominant in the extracted spectra. The $1b_1$'-dominant peak profile with a clear shoulder structure around 524.5 eV (possibly assigned as $3a_1$ derived peak) obtained for the 65 wt% PVP solution is quite similar to the previously obtained spectrum for water molecules confined in a polyelectrolyte brush [2]. Therefore water molecules in the 65 wt% PVP solution may exist almost in the form of non-freezing and intermediate water hydrating the PVP polymer. Water molecules in the 30 wt% PVP solution consist of strong $1b_1$' and weak $1b_1$'' profiles, which can be reproduced by the mixture of bulk liquid water as well as non-freezing and intermediate water hydrating the PVP polymer. Detailed analysis of the XES fraction for the water hydrating PVP may have rich information about the hydrogen-bonded structure of intermediate water and its relation to the biocompatibility of PVP.

Figure 2(b) shows the O 1s XES spectra of PEG (M_w=3350) aqueous solutions. Broad peaks at ~526.5 eV and ~528.0 eV were observed for the XES spectra of dry-PEG. In this case, in addition to the energy range below 522 eV, the energy range above 526 eV was also used for the fitting to estimate the PEG contribution. The results after removal of the polymer contribution are shown in the bottom of Figure 2(b). It should be noted that the extracted XES profiles are close to the spectrum of pure water, in contrast to the PVP results. The present study raises the possibility that a *static* hydrogen-bonded structure of intermediate water is different between PVP and PEG aqueous solutions. In contrast, *dynamical* hydrogen-bonded structure of intermediate water hydrating PVP and PEG aqueous solutions is similar [4, 5]. Consequently, to understand the behavior of intermediate water, it is important to understand both the *dynamical* and the *static* hydrogen-bonded structures. Several questions remain unanswered at present yet. Future studies on the current topic are recommended.

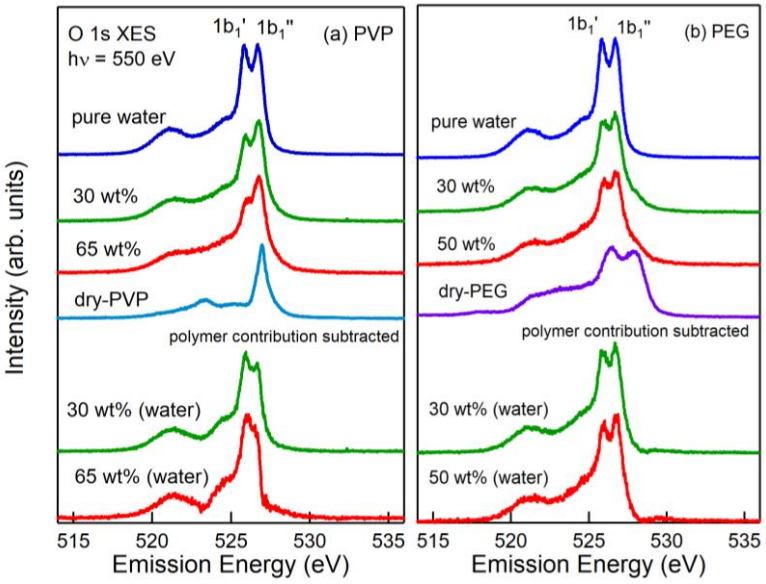

Figure 2. O 1s XES spectra of (a) PVP and (b) PEG aqueous solutions. The spectra of pure water and dried polymer powder were also shown for comparison. Bottom: Spectra with the polymer contribution subtracted.

References

[1] T. Tsuruta, *J. Biomater*. Sci. **21** (2010) 1831.
[2] K. Yamazoe *et al*., *Langmuir* **33** (2017) 3954.
[3] T. Tokushima *et al.*, *Chem. Phys. Lett*. **460** (2008) 387.
[4] T. Takei *et al.*, *Anal. Sci.***26** (2010) 337.
[5] M. Nakada *et al.*, *Materialia* **12** (2020) 100743.

Present status of the development of time-resolved ambient pressure X-ray photoelectron spectroscopy system at SPring-8 BL07LSU

Susumu Yamamoto* and Iwao Matsuda

The Institute for Solid State Physics, The University of Tokyo

** Present affiliation: Institute of Multidisciplinary Research for Advanced Materials, Tohoku University*

Introduction

Operando spectroscopy, observation of working catalysts under reaction conditions, is essential for our understanding of reaction mechanisms as well as the rational development guidelines for novel catalysts. Ambient pressure X-ray photoelectron spectroscopy (AP-XPS) is one of the most powerful *operando* spectroscopies, which permits the investigation of the electronic and chemical states of adsorbates and catalysts under gas atmospheres at near-ambient pressure. However, the typical temporal resolution of AP-XPS has been limited to ms, and thus the dynamic processes faster than ms could not be studied. A pump-probe measurement can overcome the limitation of the temporal resolution, in which a sample is pumped by ultrafast optical laser and probed by X-ray. At SPring-8 BL07LSU, we developed time-resolved X-ray photoelectron spectroscopy (tr-XPS) in ultrahigh vacuum in a pump-probe fashion [1, 2]. The temporal resolution of tr-XPS is ~50 ps, which is determined by the pulse width of probe X-ray.

In this study, we aimed to develop a time-resolved ambient pressure X-ray photoelectron spectroscopy (tr-APXPS) by combining AP-XPS with tr-XPS. tr-APXPS permits monitoring the time evolution of photocatalytic reactions in real time and under reaction conditions; all the players in photocatalytic reactions such as photo-excited carriers, adsorbates, substrates can be investigated by tr-APXPS.

Experimental

The experiments were performed at the soft X-ray undulator beamline BL07LSU at SPring-8 [3]. AP-XPS experiments were carried out using an AP-XPS apparatus that combines a differentially pumped electron analyzer (SPECS, PHOIBOS 150 NAP) with an ambient-pressure gas cell [4]. A one-dimensional delay-line detector (DLD) is adopted as a detector of the electron analyzer.

Femtosecond (fs) laser systems were installed at SPring-8 BL07LSU. The fs laser pulses were synchronized to synchrotron radiation X-ray pulses, and the delay time of fs laser pump pulse relative to X-ray probe pulse can be controlled. There were two different fs laser systems; high pulse energy and low repetition rate (mJ, 1 kHz) and low pulse energy and high

repetition rate (μJ, 208 kHz). Optical parametric amplifier (OPA) was installed in both laser systems, which can change the wavelength of fs laser. In the present study, high pulse energy and low repetition rate (mJ, 1 kHz) laser system was used.

Results and discussion

In the development of tr-APXPS, we reported the installation of a soft X-ray chopper at SPring-8 BL07LSU. The soft X-ray chopper was operated at 1 kHz, and reduced the repetition rate of probe X-ray (208 kHz in the H-mode operation of SPring-8) to 1 kHz to match that of pump laser. Consequently, time-resolved XPS measurements became possible with the same experimental setup as in conventional static XPS measurements. In addition, soft X-ray chopper blocks all the X-ray pulses that are not used in pump-probe measurements. This decreases unnecessary burden on the sample and the detector. Thus, the photon flux can be increased by opening slits in X-ray beamline to improve measurement efficiency.

Test tr-APXPS measurements were performed on the naturally oxidized *p*-type Si(111) (SiO_2/*p*-Si(111)) surface in 1 mbar CO_2. The wavelength of pump laser was changed from 800 nm to 400 nm. This was because the small pre-pulses in 800 nm can induce the surface photovoltage effect of Si. The amplitude of the pre-pulses was much decreased by frequency doubling to 400 nm. In addition to the energy shift of Si 2*p* core level due to surface photovoltage effect, we could detect the energy shift of CO_2 gas phase peak in O 1*s* core level. The energy shift of gas phase peak in AP-XPS reflects the change of the sample work function. Notably, the energy shift was different between Si 2*p* and O 1*s* core levels. The present results demonstrate that of tr-APXPS can provide a wealth of information in photo-excited systems and will be very suited to study various light-induced reactions including photocatalysts and plasmonic chemical reactions.

REFERENCES

[1] K. Ozawa, S. Yamamoto, *et al.*, e-J. Surf. Sci. Nanotechnol. **17**, 130-147 (2019).

[2] M. Ogawa, S. Yamamoto, *et al.*, Rev. Sci. Instrum. **83**, 023109 (2012).

[3] S. Yamamoto *et al.*, J. Synchrotron Rad. **21**, 352-365 (2014).

[4] T. Koitaya, S. Yamamoto, *et al.*, e-J. Surf. Sci. Nanotechnol. **17**, 169-178 (2019).

Development of time-resolved X-ray absorption and photoelectron spectroscopy system using time-of-flight electron analyzer

Susumu Yamamoto[1,*], Rei Hobara[2], Kenichi Ozawa[3], and Iwao Matsuda[1]

[1] *The Institute for Solid State Physics, The University of Tokyo*

[2] *Department of Physics, The University of Tokyo*

[3] *Department of Chemistry, Tokyo Institute of Technology*

** Present affiliation: Institute of Multidisciplinary Research for Advanced Materials, Tohoku University*

Introduction

Understanding the dynamics of photoexcited carriers is essential for improving the efficiency of light-energy conversion materials such as photocatalysts and solar cells. Photoexcited carriers (electrons/holes) generated by light absorption move between an occupied state and an unoccupied state. Therefore, it is important to observe both occupied and unoccupied states in order to get the whole picture of the photoexcited carriers dynamics. However, there has been no experimental method that allows the observation of both occupied and unoccupied states dynamics.

In this study, we aim to develop a picosecond time-resolved X-ray absorption/photoelectron spectroscopy (XPS/XAS) system using a time-of-flight (TOF) electron analyzer, and track the temporal changes of electronic structures in both occupied and unoccupied states. In addition, the TOF electron analyzer has a unique feature that all kinetic energy electrons can be detected and energy-resolved by the detector. In the case of a hemispherical electron analyzer, only electrons with the fixed kinetic energy determined by electrostatic lenses are detected by the detector. Taking advantage of this unique feature of TOF electron analyzer, we can measure XAS spectra with different probing depths at once. The time-resolved XAS spectra using TOF analyzer will allow the temporal evolution of excited electronic states along the depth direction.

Experimental

The experiments were performed using a TOF electron analyzer (VG Scienta, ARTOF 10k) at the soft X-ray undulator beamline BL07LSU at SPring-8 [1]. We developed a picosecond time-resolved XPS system using the TOF electron analyzer, and studied the relaxation dynamics of photoexcited carriers on various surfaces and interfaces [2]. In the present study, thus, we aim to extend the application of the TOF electron analyzer to XAS measurements. We developed the software program that can control both TOF electron analyzer and the soft X-ray beamline (undulator and monochromator) to measure XAS spectra. The sample studied in this research was the rutile TiO_2(110) surface. The sample surface was cleaned by Ar ion sputtering (1.0 kV, $1x10^{-4}$ Pa Ar, 10 min), and annealing in an oxygen atmosphere (920 K in $1x10^{-4}$ Pa O_2). The surface order was confirmed by low energy electron diffraction (LEED).

Results and discussion

Figure 1 shows the Ti L-edge XAS spectrum of the clean TiO_2(110) surface measured using TOF electron analyzer. The XAS spectrum in total electron yield (TEY) was obtained by integrating the whole TOF region indicated by the blue lines in Fig. 1(a). The obtained XAS spectrum in Fig. 1(b) is in good agreement with the TEY-XAS spectrum measured with the sample current. This confirms the successful measurement of XAS spectra using TOF electron analyzer. By changing the TOF window for the integration, we can change the probing depth. For example, we could obtain the surface sensitive XAS spectra if the TOF window is tuned to Auger electrons. Now we plan to perform XAS experiments on the sample that has a distribution of chemical states in the depth direction (*e.g.*, ice H_2O thin films adsorbed on the TiO_2 surface).

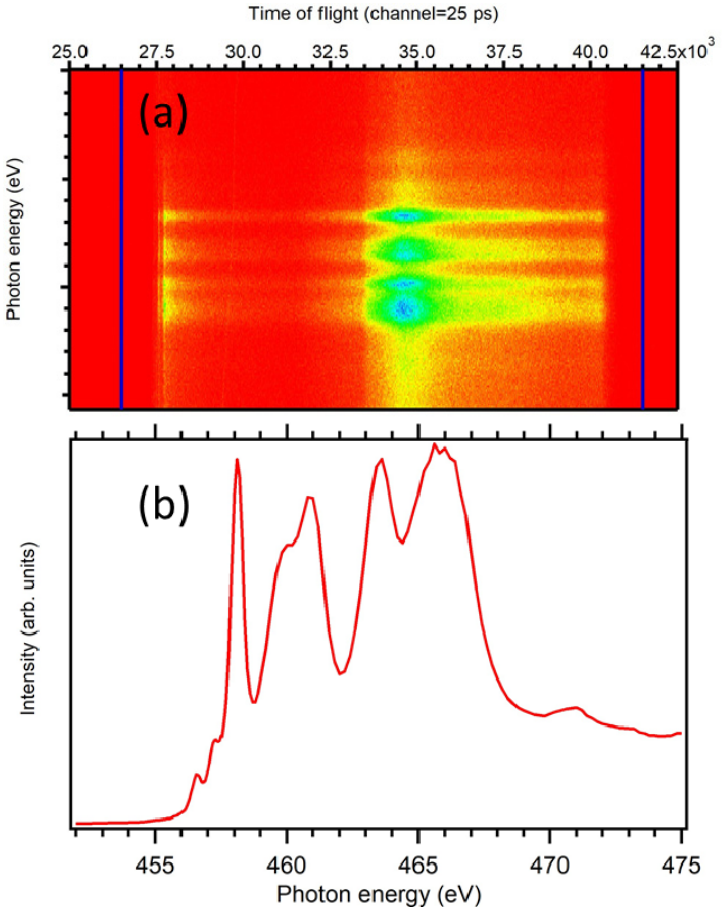

Figure 1. Ti L-edge XAS spectrum of the clean TiO_2(110) surface measured using TOF electron analyzer. (a) TOF spectra as a function of photon energy (b) XAS spectrum obtained by integrating the TOF region indicated by the blue lines in the panel (a).

REFERENCES

[1] S. Yamamoto *et al.*, J. Synchrotron Rad. **21**, 352-365 (2014).

[2] S. Yamamoto *et al.*, J. Phys. Soc. Jpn. **82**, 021003 (2013).

SOFT X-RAY ABSORPTION SPECTROSCOPY OF Ca_2RuO_4 UNDER ELECTRIC FIELD

Daiki Ootsuki[1], Yukie Takasuka[1], Ayuko Hishikawa[1],
Tatsuhiro Ishida[1], Teppei Yoshida[1], Kosuke Yamazoe[2], Tomoyuki Tsukada[2],
Jun Miyawaki[2], Yoshihisa Harada[2],
Chanchal Sow[3], Shingo Yonezawa[3], Yoshiteru Maeno[3], and Fumihiko Nakamura[4]
[1]*Graduate School of Human and Environmental studies, Kyoto University,*
[2]*Synchrotron Radiation Laboratory, The Institute for Solid State Physics, The University of Tokyo,*
[3]*Department of Physics, Kyoto University,*
[4]*Department of Education and Creation Engineering, Kurume Institute of Technology*

The exploration of non-equilibrium phase transition and non-linear conductivity in strongly correlated electron systems is one of the frontier of condensed matter physics. By applying electric fields, Mott insulators exhibit the insulator to metal transition with a non-linear conductivity [1-2], which is so called "Mott breakdown" analogous to dielectric breakdown [3]. Recently, Nakamura *et al*. have discovered an electric-field induced insulator to metal transition of Ca_2RuO_4 with nonlinear conductivity. The threshold electric field E_{th} of ~40 V/cm is weakest among the Mott insulators [4]. It would be desirable to understand how the electronic structure is changed by applying electric field and to clarify the origin of the non-linear conductivity of Ca_2RuO_4.

The various stimuli such as temperature, chemical substitution, and applied pressure induce the metal to insulator transition of Ca_2RuO_4 with a structural phase transition [5-7]. The structural phase transition affects the orbital configuration of this system through RuO_6 octahedra [5]. Actually, the insulating state of Ca_2RuO_4 is characterized by the crystal field splitting as well as on-site Coulomb interaction. The recent polarization-dependence of angle-resolved photoemission spectroscopy combined with dynamical mean-field theory (DMFT) revealed the coexistence of the band insulating state of d_{xy} orbitals originating from the crystal-field splitting and the Mott insulating states of half-filled $d_{xz/yz}$ orbitals [8].

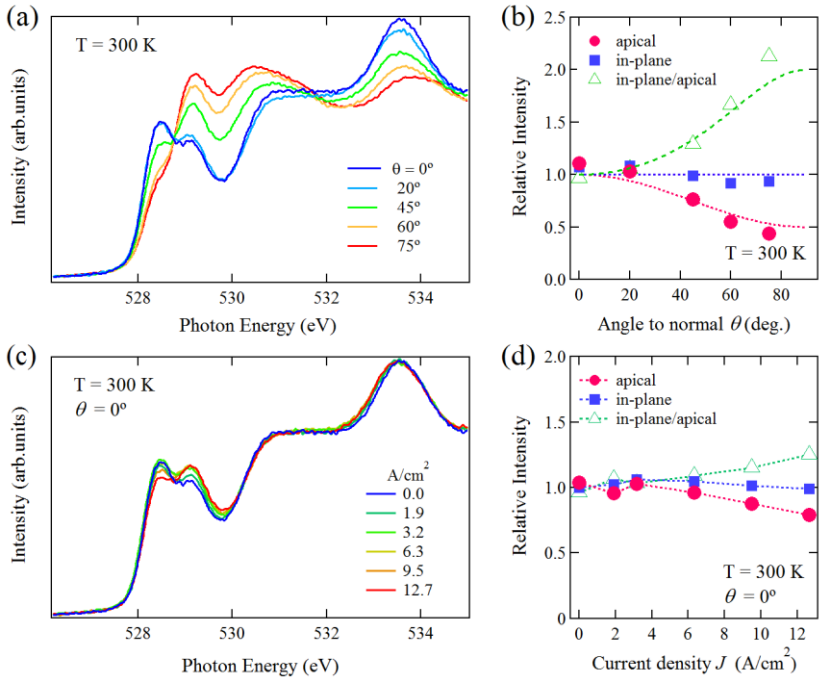

Figure 1. O 1*s* XAS spectra of Ca_2RuO_4 as a function of (a) angle θ and (c) current density J. Intensities of apical and in-plane components as a function of (b) angle θ and (d) current density J.

In this study, we have investigated the electric-filed dependence of the electronic structure for Ca_2RuO_4 by means of soft x-ray absorption spectroscopy (XAS) under electric field at SPring-8 BL07LSU. High quality single crystals of Ca_2RuO_4 were grown by floating-zone method. In order to apply the electric field, the gold wires were attached to the terminals both ends of the sample using silver epoxy. The electric field was applied parallel to the *ab*-plane and the voltage-current characteristics were measured *in situ* during the XAS measurements. The sample temperature is monitored by the directly attached Pt thermometer and controlled by liquid helium. Although the current flow gives rise to the joule heating effect, the sample heating kept less than 3 K during all measurements.

Figure 1 (a) shows the angle dependence of the O 1*s* x-ray XAS spectra take at T = 300 K. The XAS spectrum strongly depends on the angle θ. We focus on the intensities at ~528.3 eV and ~529.1 eV derived from the apical and in-plane oxygen, respectively. To quantify the intensities of the apical and in-plane components, we fitted the intensities derived from apical and in-plane oxygen with a Gaussian as shown in Fig. 1 (b). The angle dependence of XAS spectra is basically consistent with the previous XAS study reported by Mizokawa *et al* [9]. This indicates that the carrier concentration between the Ru $4d_{xy}$ and $4d_{yz/zx}$ orbitals is close to 1:1 at T = 300 K. Figures 1 (c) and (d) show the electric field dependence of the XAS spectra at T = 300 K. Here, we obtained the electric-field dependence of XAS spectra at the normal incidence. By increasing current density J, the apical intensity decreases, while the in-plane intensity increases. As shown in Fig. 1 (d), the intensity ratio of the apical and in-plane components gradually increases with current density J.

Figure 2 shows the relationship between the crystal-field splitting Δ, spin-orbit coupling λ_{so}, and the intensity ratio of the apical and in-plane components of XAS spectra. The solid curve indicate the theoretical estimation on the basis of the simple Hamiltonian of Ref. 10. From the theoretical curve, we obtained the crystal-field splitting Δ and spin-orbit coupling λ_{so}. With increasing current density, the crystal field splitting energy increases from the compressed RuO_6 octahedra to the elongated RuO_6 octahedra. These results suggest that the electric field induces the elongation of the RuO_6 octahedra.

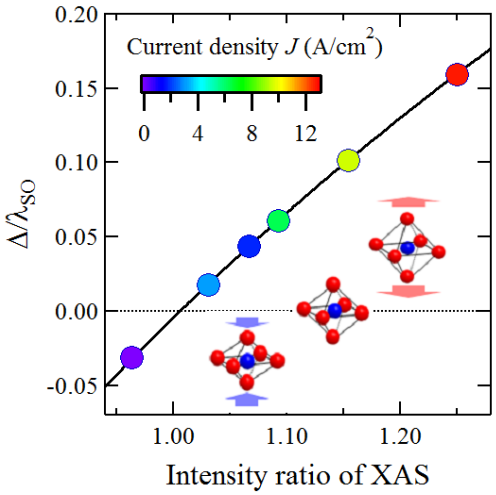

Figure 2. XAS intensity ratio between the apical and in-plane components. The solid line is the model expectation of the Hamiltonian of Ref. 10.

REFERENCES

[1] Y. Taguchi *et al.*, Phys. Rev. B **62**, 7015 (2000).
[2] K. Inagaki *et al.*, J. Phys. Soc. Jpn. **73**, 3364-3369 (2004).
[3] T. Oka, Phys. Rev. B **86**, 075148 (2012).
[4] F. Nakamura *et al.*, Sci. Rep. **3**, 2536 (2013).
[5] O. Friedt *et al.*, Phys. Rev. B **63**, 174432 (2001).
[6] F. Nakamura *et al.*, Phys. Rev. B **65**, 220402 (2002)
[7] S. Nakatsuji and Y. Maeno, Phys. Rev. Lett. **84**, 2666–2669 (2000).
[8] D. Sutter *et al.*, Nat. Commun. **8**, 15176 (2017).
[9] T. Mizokawa *et al.*, Phys. Rev. Lett. **87**, 07702 (2001).
[10] G. Fatuzzo *et al.*, Phys Rev. B **91**, 155104 (2015).

OPERANDO XPS STUDY OF CO_2 HYDROGENATION ON A SINGLE-ATOM ALLOY Pd-Cu MODEL CATALYST

J. Yoshinobu, S. Tanaka, K. Mukai, W. Osada, T. Matsuda, S. Nakano, Y. Choi,
S. Yamamoto, and I. Matsuda
The Institute for Solid State Physics, The University of Tokyo

Introduction

Single-atom alloy catalyst (SAAC) is an alloy in which a small amount of functional metal atoms are deposited and embedded in the surface of a metal substrate. The deposited atoms give a new specific function to the substrate, where the main catalytic activity of the substrate is still active [1]. When high-resolution XPS measurement is performed using high-intensity synchrotron radiation, a very small amount (a few percent or less) of embedded atoms on the substrate surface can be detected, and their chemical states can be clearly identified. Furthermore, it is possible to observe the changes in the electronic and chemical states of the adsorbed atoms/molecules as well as the catalyst surface in ambient conditions using NAP-XPS. *Operando* measurments using mass spectrometry and NAP-XPS can elucidate the catalytic function of SAAC during the reaction.

In this study, we prepared a single-atom alloy catalyst (SAAC) Pd-Cu(111) and investigated the hydrogenation of carbon dioxide (CO_2) using NAP-XPS. CO_2 is one of the greenhouse effect gases. At present, methanol synthesis from CO_2 is performed at high temperature (~500K) and under high pressure using Cu/ZnO catalysts. This reaction is an exothermic reaction, in which the molar number decreases for the forward direction. Thus, more active and efficient catalysts which can be operated at lower temperature are highly demanded.

Recently, we found the desorptions of hydrogenated species after a large amount of hydrogen exposure to formate species (HCOO) on a Pd-Cu(111) surface using temperature programmed desorption. In the present study, we aimed to clarify the hydrogenation reaction process of CO_2 on a single-atom alloy catalyst Pd-Cu(111) by NAP-XPS.

Experimental

Experiments were carried out using NAP-XPS system at SPring-8 BL07LSU. The clean Cu(111) was prepared in a UHV preparation chamber of NAP-XPS system. A small amount of Pd was vapor-deposited on the surface to prepare a single atom alloy model catalyst Pd-Cu(111). The amount of Pd deposited was estimated to be 0.02 ML (monolayer). In a NAP cell, CO_2 (0.9 mbar) and H_2 (0.5 mbar) were introduced under isothermal conditions near room temperature. During this process, the model catalyst surface was observed by NAP-XPS. Next, the substrate temperature was raised stepwise by heating under constant pressure of CO_2 (0.9 mbar) and H_2 (0.5 mbar).

Results and discussion

Before the introduction of mixed gases (CO_2 + H_2), only H_2 was gradually introduced in the NAP cell at 300 K up to 3.0 mbar, and the model catalyst surface was investigated by NAP-XPS; the core-level spectra of Cu 2p, Cu LVV Auger, Cu 3p, and Pd 3d were measured. However, any peak shifts due to hydrogen adsorption and an appearance of new peaks were not

observed under the present conditions. Even if the dissociative adsorption of hydrogen occurs, hydrogen is thermally desorbed at room temperature, i.e., a sufficient amount of hydrogen is not adsorbed on the surface.

CO_2 (0.9 mbar) and H_2 (0.5 mbar) were introduced into the NAP cell at 300 K, and Pd3d, C1s, and O1s were observed by AP-XPS (see Fig. 1). Based on our previous study [2], major surface species were attributed to CO_3 species; a small amount of atomic oxygen were also observed. In the case of Pd3d, a small peak was newly observed on the high binding energy side. This may be assigned to the Pd atoms bonded to atomic oxygen species.

When heating the sample from 300K to 500K, the C1s and O1s peaks originating from CO_3 species were observed up to 375K but almost disappeared above 390K. The O1s peak attributed to atomic oxygen almost disappeared above 375K. On the other hand, the peak derived from carbon species (~284 eV) gradually increased with heating.

The present study suggests that the dissociation of CO_2 and the formation of CO_3 and O species occur at 300 K (disproportionation). However, no experimental evidence was detected to indicate hydrogenation of CO_2 at the present experimental conditions. Therefore, in order to achieve a sufficient amount of adsorbed hydrogen atoms at the surface to induce hydrogenation, lower temperature and/or higher H_2 pressure may be needed.

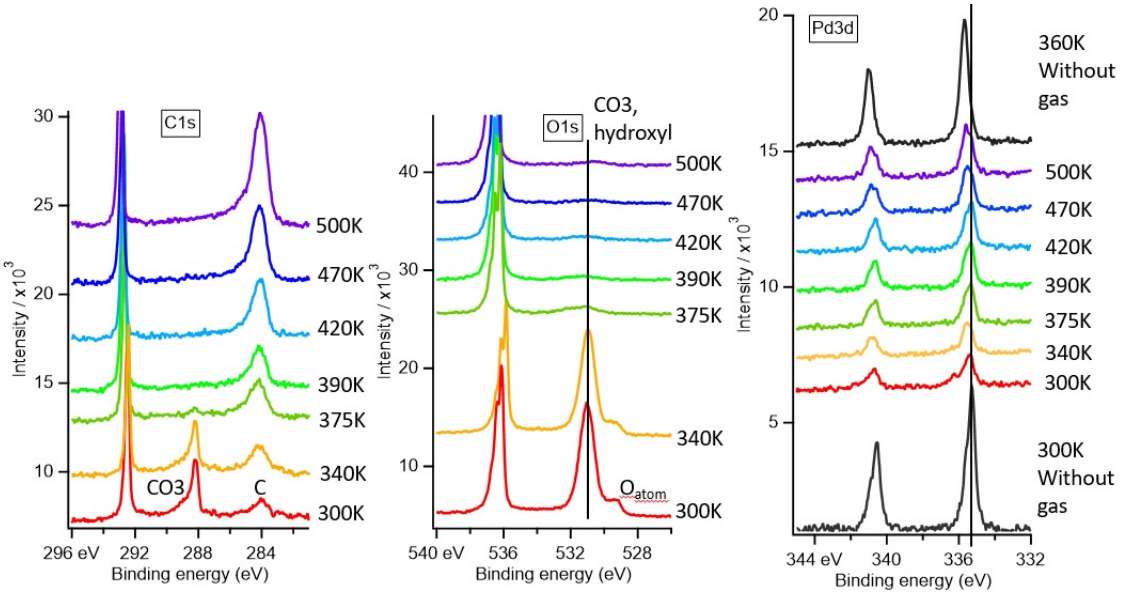

- Figure 1 A series of XPS spectra of C 1s, O 1s and Pd 3d of the Pd-Cu(111) surface under CO_2 (0.9 mbar) and H_2 (0.5 mbar) at 300 K and subsequent heating.

REFERENCES

[1] G. Giannakakis et al., Accounts of Chemical Research, **52**, 237 (2018).
[2] T. Koitaya et al., Topics in Catalysis, **59**, 526 (2016).

AP-XPS STUDY OF ELECTRONIC STATES OF METAL NANO PARTICLES AND METAL HYDRIDE COMPLEX

J. Yoshinobu[1], W. Osada[1], Y. Choi[1], S. Tanaka[1], K. Mukai[1],
T. Koitaya[2], S. Yamamoto[3], and I. Matsuda[1]
[1]*The Institute for Solid State Physics, The University of Tokyo*
[2]*Institute for Molecular Science*
[3]*Institute of Multidisciplinary Research for Advanced Materials, Tohoku University*

Introduction

When a hydrogen atom is bonded to metal, the chemical state of hydrogen can be classified into atomic hydrogen (H), proton (H^+) or hydride (H^-), or an intermediate state between them; it can easily change, depending on its surrounding environment. The chemical state of metal which is bonded to hydrogen also changes accordingly. By utilizing various hydrogen species on a metal surface, a new reaction path can be developed for "highly selective", "very difficult" and/or "highly efficient" processes. One might think that a metal is “reduced” when it is bonded to hydrogen. However, when neutral hydrogen takes an electron from metal and it becomes hydride (H^-), the metal is now “oxidized”. Using high-resolution X-ray photoelectron spectroscopy (XPS), the chemical state of metal can be elucidated at each site, based on the chemical shift of its core level peak. In the case of surface chemistry, we can trace the chemical states of surface and bulk during the processes including hydrogen adsorption, absorption and desorption. Although the formal charges of hydrogen and metal have been estimated based on valency in a hydrogen-containing metal complex, one can experimentally elucidate the chemical state of a metal atom using XPS. In this study, we planned to perform ambient pressure (AP) XPS measurements of metal-alloy nanoparticles and multinuclear metal complexes in the presence of hydrogen.

Experimental

In this beam time, we carried out XPS measurements of Pt nano particles and $Pt_{75}Pd_{25}$ nano particles synthesized by Yamauchi group at Kyushu University, and multinuclear Ti complexes including Ti_4N_4 $[C_5Me_4SiMe_3]_4$ synthesized by Shima group at RIKEN (hereafter abbreviated as Ti_4N_4 complex).

(A) In the case of Pt and $Pt_{75}Pd_{25}$ nano particles, these nano particles were deposited on a Au foil. First, we measured Pt 4f and Pd 3d XPS in vacuum at room temperature. Next, the sample was heated to 250 °C in vacuum, and Pt 4f and Pd 3d XPS spectra were measured in vacuum at room temperature. Finally, the sample was heated under H_2 (20 mbar) at 250 °C for 20 minutes, and XPS of Pt 4f and Pd 3d measurements were performed at room temperature.

(B) In the case of Ti_4N_4 complex, a small amount of Ti_4N_4 complex was dissolved in degassed n-hexane in an Ar glove box and 5 μL of this solution was dropped on a PdCu alloy substrate. After evaporating and drying the sample solvent, the sample was carefully moved from the glove box to the load-lock chamber of the AP-XPS system using a vacuum transfer device. First, we measured XPS spectra of Ti 2p, C 1s, O 1s and N 1s in vacuum at room temperature. Next, H_2 gas (5 mbar) was introduced and subsequently evacuated; during this process AP-XPS measurement was carried out for Ti 2p, C 1s, O 1s and N 1s.

Results and discussion

(A) XPS spectra of Pt nano particles and $Pt_{75}Pd_{25}$ nano particles during the above processes were obtained. When comparing the XPS spectra of the as-installed sample and the heated

sample at 250°C, we confirmed that the O 1s intensity was decreased after heating, but a remarkable change in the spectral shapes of Pt 4f and Pd 3d was not observed. Even after heating at 250°C under H_2 pressure (20 mbar) for 20 minutes, no significant change was observed in Pt 4f and Pd 3d XPS in vacuum. Thus, the significant surface segregation of Pd atoms in the alloy nano particle was not observed under the present hydrogen pressure and heating conditions.

(B) Our previous experiments suggested that the present Ti_4N_4 complex reacts with oxygen and water, and it is easily oxidized. In this experiment, we carefully prepared the sample and transferred it to the AP-XPS chamber as described above. Figure 1 shows Ti 2p, C 1s, O 1s and N 1s XPS spectra of Ti_4N_4 complex on a PdCu substrate. Ti $2p_{3/2}$ and N1s peaks were observed at 456.8 eV and 397.2 eV, respectively, indicating that Ti takes a tetravalent state and N atoms are bonded to the metal. Next, we also carried out AP-XPS measurements during the H_2 exposure and pumping processes. Upon H_2 exposure, we found the disappearance of N 1s peak, the increase of O1s and the peak shift of Ti $2p_{3/2}$ to 459.6eV. These results indicate that there is no nitrogen in the complex and it was oxidized. We assume that upon H_2 exposure the partial pressure of water vapor was increased in the AP cell by some reactions between hydrogen and the inner wall of a stainless-steel AP cell, and thus produced water reacts with the complex.

For future work, we need to control the gases in the AP cell to eliminate the possibility of oxidation of metal complex.

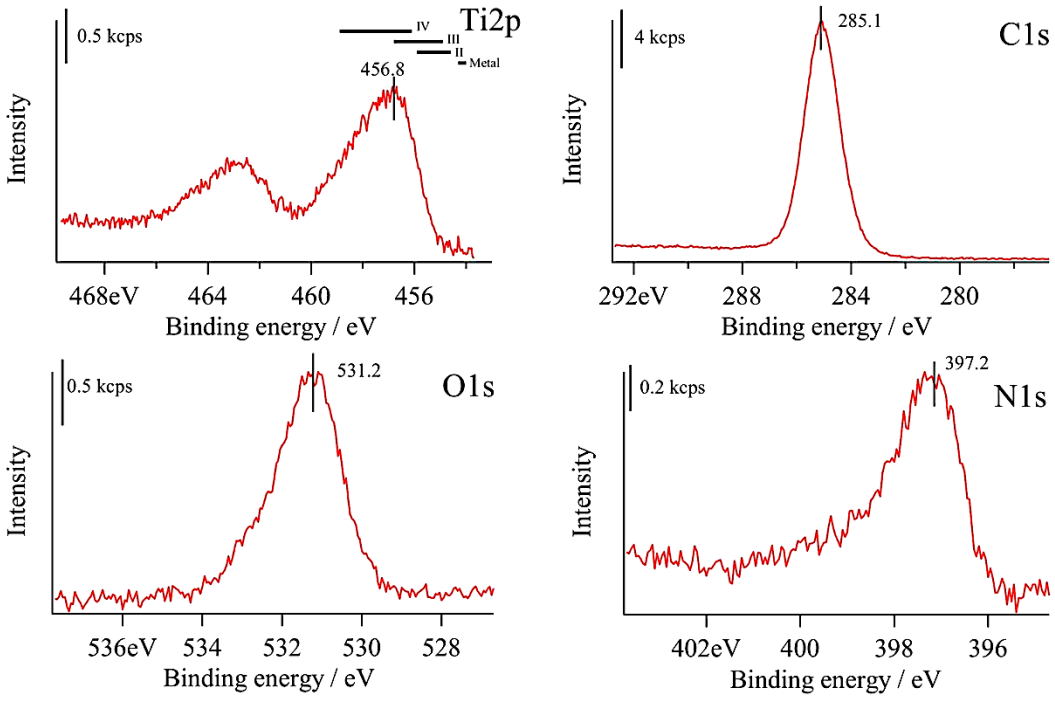

Figure 1 Ti 2p, C 1s, O 1s and N 1s XPS spectra of Ti_4N_4 complex deposited on a PdCu substrate. XPS measurements were carried out in vacuum at room temperature (hν =680 eV).

DYNAMICS OF PHOTOCATALYTIC MATERIALS FOR WATER SPLITTING REACTION STUDIED BY TRANSIENT X-RAY ABSORPTION SPECTROSCOPY

Yohei Uemura,[1] Ahmed Ismail,[1] Hebatalla Elnaggar,[1] Federica Frati,[1] Hiroki Wadati,[2,3] Yasuyuki Hirata,[2] Yujun Zhang,[2] Kohei Yamagami,[2] Susumu Yamamoto,[2] Iwao Matsuda,[2] Frank de Groot[1]

[1]*Inorganic Chemistry and Catalysis, Debye Institute for Nanomaterials Science, Utrecht University, Universiteitslaan 99, 3584 CG Utrecht, The Netherlands*

[2] *Institute for Solid State Physics, University of Tokyo, Kashiwa, Chiba 277-8581, Japan*

[3] *Graduate School of Material Science, University of Hyogo, Kamigori, Hyogo 678-1297, Japan*

Introduction

From the viewpoint of building a sustainable society, developing a renewable energy resource is an important subject in the modern science and technologies. Water splitting reaction where water molecules (H_2O) are decomposed into hydrogen (H_2) and oxygen (O_2) is expected to be a key reaction to achieve a renewable energy process. Photocatalysts and photoelectrodes play a central role in the water splitting reaction utilizing sunlight. Semiconductors such as TiO_2, α-Fe_2O_3 is typical photocatalysts/photoelectrodes. They have been developed for several decades and new materials are still explored to enhance its catalytic efficiency for our daily use. Fundamental studies on the mechanisms of photocatalysts/photoelectrodes have been based on theoretical calculations, electrochemical methods and spectroscopic studies. X-ray absorption spectroscopy (XAS) is a new trend to study the excited states of photocatalytic materials. XAS can address local symmetries and electronic states of a specific element in the material under investigation and give complementary information which is not provided from optical spectroscopies. In order to understand dynamics of excited states of photocatalysts and photoelectrodes, we measured thin films of hematite (α-Fe_2O_3) and copper tungstate ($CuWO_4$). α-Fe_2O_3 and $CuWO_4$ are have been studied as photoelectrodes for solar-assisted water splitting reaction. We have already measured fast carrier dynamics of both the samples based on femtosecond XAS measurements in PAL-XFEL. [1] We focused on how the photoexcited states are progressed in hundreds of picoseconds. Here, we will present the result of the transient XAS study on the photoexcited state of α-Fe_2O_3, which has been recently published in ref. 1.

Experimental details

Pump probe XAS experiments were performed at BL07LSU, SPring-8. An illustration of the setup employed in this study is displayed in Figure 1 (a) and the details of the setup is described in ref. 2. The repetition of the excitation laser was ~1 kHz and its wavelength was ~400 nm which was generated by doubling the fundamental wavelength of a Ti:Sapphire laser (~800 nm) using a BBO crystal. The samples were thin films of α-Fe_2O_3 and $CuWO_4$ deposited on an Indium-Tin-oxide-coated glass substrate. The thickness of the samples was ~ 50 nm.

Results

Transient XAS measurements by the sample current: In our experiments, an x-ray chopper developed in SPring-8 was employed in order to select x-ray synchronised with an excitation laser.[3] In the previous experiments [2], the signals from the x-ray pulses synchronised with an excitation laser were accumulated by using electric gates. Although the x-ray signals can be efficiently by this method, a fast-response detector (response time: nanoseconds) is needed to be employed. The x-ray chopper can isolate the x-rays synchronised with the laser and only the selected x-rays hit a sample. As the consequence, a relatively slow-responce detector (~ miliseconds) could be employed. In our beamtime, we tried to measure transient XAS by measuring the sample current in addition to counting photoelectrons from the sample. transient XAS of the α-Fe_2O_3 sample was measured by the sample current.

Although XAS spectra with a good signal-to-noise ratio (S/N) was obtained by measuring the sample current, we did not confirm transient signals measured by the sample current. It would because the excitation laser affected the sample current signals, which could be smeared out transient signals. However, the synchronization of the x-ray pulses was achieved and obtained XAS spectra with a good S/N. It would be possible to measure XAS with a transmitting geometry by employing the x-ray chopper, which should extend the choice of the samples to be measured. It would be possible to distinguish transient signals from bulk and from surface of a sample when the sample current and PEY are employed at the same time.

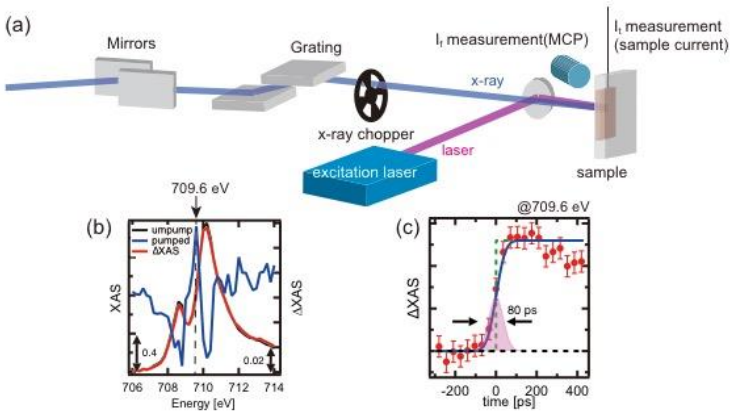

Figure 1 (a) an illustration of the experimental setup at BL07LSU, (b) the transient Fe L_{III} edge XAS spectra of hematite (c) the kinetic trace at 709.6 eV

The transient XAS of α-Fe_2O_3: Transient Fe L_{III} XAS of hematite was measured by a partial electron yield (PEY) detection. The fluence of the excitation laser was set to 10 mJ/cm^2, which is below the damage threshold of the sample. The transient XAS at a delay time of 80 ps is shown in the central panel of Figure 1. There are three distinctive transient features found around 708.6, 709.6 and 710.2 eV. The transient feature around 709.6 eV was also observed by the transient experiments in PAL-XFEL, which appeared just after the sample was excited by the laser.[1] The transient feature originates from the creation of Fe(II) species compared by the theoretical calculations. The transient features seen around 708.6 eV and 710.2 eV were not observed at faster delay time (< 10 ps) in PAL-XFEL. These new features could come from local structural changes which happens between 10 ps and 80 ps after the photoexcitation. Small polaron creation in a hematite thin film was observed around a delay time of 1 ps after photoexcitation by femtosecond transient extreme ultraviolet spectroscopic experiments[4]. Further local structural changes could happen in later delay time. Considering the time range of water splitting reaction, the excited state of hematite should be important to understand the driving force of the water splitting reaction. We have also measured transient XUV spectra of several hematite samples by a delay time of 1 ns. We would like to combine the transient Fe L_{III} XAS data with the XUV data to understand more details of photoexcited states of hematite.

REFERENCES

1. Ismail, A. S. M., et al., Direct Observation of the Electronic States of Photoexcited Hematite with Ultrafast 2p3d X-Ray Absorption Spectroscopy and Resonant Inelastic X-Ray Scattering. *Phys. Chem. Chem. Phys.* **2020**, *22*, 2685-2692.
2. Takubo, K., et al., Capturing Ultrafast Magnetic Dynamics by Time-Resolved Soft X-Ray Magnetic Circular Dichroism. *Appl. Phys. Lett.* **2017**, *110*, 162401.
3. Osawa, H.; Ohkochi, T.; Fujisawa, M.; Kimura, S.; Kinoshita, T., Development of Optical Choppers for Time-Resolved Measurements at Soft X-Ray Synchrotron Radiation Beamlines. *Journal of Synchrotron Radiation* **2017**, *24*, 560-565.
4. Carneiro, L. M.; Cushing, S. K.; Liu, C.; Su, Y.; Yang, P.; Alivisatos, A. P.; Leone, S. R., Excitation-Wavelength-Dependent Small Polaron Trapping of Photoexcited Carriers in A-Fe_2o_3. *Nat. Mater.* **2017**, *16*, 819-825.

INVESTIGATION OF THE ELECTRONIC STRUCTURE OF COBALT OXIDE SPINEL ON ELECTRODES FOR WATER OXIDATION CATALYSTS USING CO 2P3D RIXS

Minmin Chen,[a] Kosuke Yamazoe,[b,c] Jun Miyawaki,[b,c] Yoshihisa Harada,[b,c] Serena DeBeer,[a] Olaf Rüdiger[a]

[a]*Max Planck Institute for Chemical Energy Conversion, Mülheim an der Ruhr, Germany*

[b]*Institute for Solid State Physics, The University of Tokyo, Kashiwa, Chiba 277-8581, Japan*

[c]*Synchrotron Radiation Research Organization, The University of Tokyo, 7-3-1 Hongo, Bunkyo-ku, Tokyo 113-8656, Japan*

Development of new anode materials based on earth abundant transition metals for water splitting is strategically important for industrial and large-scale applications. Water splitting has been considered one of the most promising strategies for energy conversion and storage.[1] Here, we study Co_3O_4 spinel on electrode surfaces by spectroelectrochemistry. The spinels are synthesized as nanoparticles of around 10 nm that form aggregates of 100-300 nm diameter. The materials are drop cast on the electrode surface, in this case a gold-coated SiN window. In order to stabilize the small catalyst particles (particle size 300 nm) on the electrode surface, Nafion is used as a binder. Unfortunately, Nafion showed extreme X-ray sensitivity during our experiments. Being a fluorine-rich polymer, the F K-edge at 690 eV absorbed the X-rays and damaged the polymer structure, which resulted in a simultaneous decrease of the Co intensity.

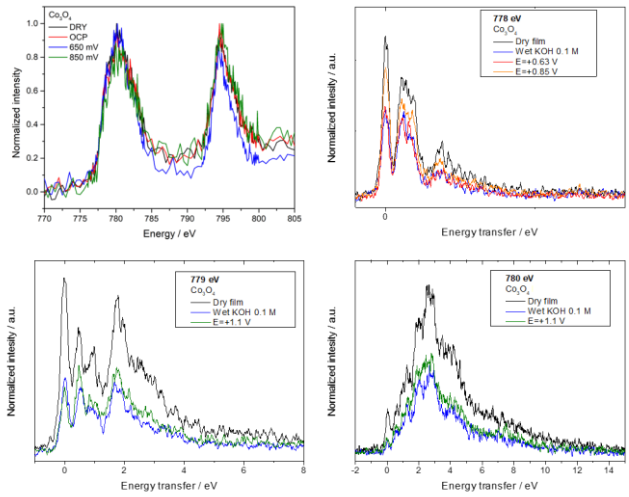

Figure 1. Co L-edge XAS (top-left) and 2p3d RIXS spectra of an electrode prepared by drop casting Co_3O_4 nanoparticles and Fumion as a binder. The conditions are indicated on the figure, the electrolvte was KOH 0.1 M.

The use of Fumion as a binder solves this problem. Fumion does not contain any F atoms in its structure and showed no detectable photodegradation during the spectroelectrochemical experiments. Nevertheless, we did not detect any significant changes on the 2p3d RIXS or at the Co L-edge XAS with the applied potential (Figure 1).

In order to understand the 2p3d RIXS of the spinel system, we also measured spectra from Al_2CoO_4, Co_2ZnO_4 and CoO as powder samples. The Al_2CoO_4 is a spinel, where the Co^{3+} at the O_h sites has been substituted with Al^{3+} atoms. Similarly, on the Co_2ZnO_4, the T_d Co^{2+} has been substituted with Zn^{2+} ions. CoO has a NaCl-like structure with all the Co^{2+} ions in a O_h geometry. The total electron yield Co L-edge XAS shown in Figure 2 (left), correspond to what would be expected for a Co^{3+} HS in the case of the Co_2ZnO_4. The lower L_3 edge position for the CoO and Al_2CoO_4 is also in agreement with a lower oxidation state of the cobalt and the different fine structure may reflect the different multiplet structure resulting from a T_d vs an O_h coordination geometry. The Al_2CoO_4 L_3 edge shows a broad peak around 785 eV that at this point we suspect is an artefact. The RIXS spectra of the CoO show a well-defined feature at 0.9 eV and a second feature that appears at higher excitation energies at 2 eV. The Al_2CoO_4 has 2 features at 0.5 and 0.9 eV. At higher incident energy an additional band appears at 2 eV. The Co_2ZnO_4 does

not show any well-defined bands, only a peak a 1.8 eV and at higher excitation energies (780-784 eV, not shown) a broad band was observed. The 2p3d RIXS spectra have been compared to the powder Co_3O_4 measured at Sextants (Figure 2, right). The spectra have been normalized to the elastic peak, except for the spectra at 779 where the elastic peak was quite weak. At low excitation energies there is a band at 0.75 eV, most likely resulting from the Co^{2+} sites on the spinel, while as the excitation energy is increased the most prominent features at around 2 eV could be assigned to the Co^{3+} sites, demonstrating the potential of 2p3d RIXS to study such materials. Multiplet calculations are planned for the near future to analyse these results in detail.

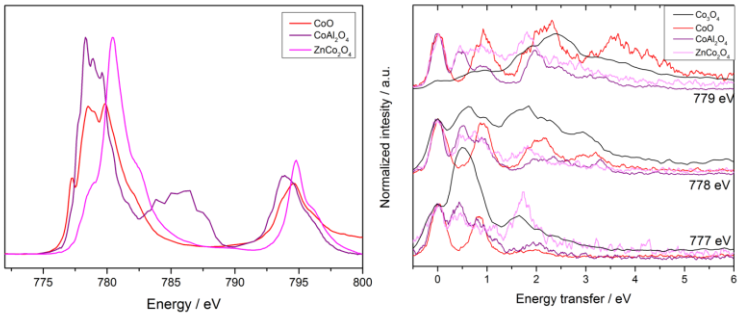

Figure 2. Co L-edge XAS (TEY) from powder samples (left) and 2p3d RIXS (right) of the same samples at three different incident energies. The spectra of Co_3O_4 powder measured at SOLEIL Sextants beamline was added to the figure as a comparison.

No significant changes were observed for the Co_3O_4 particles under different applied electrode potentials. This could be a limitation of the experimental setup used in soft X-ray measurements. Electrochemistry takes place at the interface with the electrolyte. If particle films are too thick and the changes with the applied potential take place far from the electrode surface, the X-ray beam may not penetrate enough on the film to observe any changes. Another possibility is that the particle conductivity is too small, as a result, only a minor fraction of the film may be under potential control. Consequently, we may be measuring all the time the bulk of the particles, which remain unresponsive to the applied potential (see Figure 3). We have repeated these measurements at the Co K-edge. When using hard X-rays, we probe the whole film.[2] Similarly to what we have observed on the soft X-ray regime, we could not detect significant changes on the spectral signatures with the applied potential. This suggests, that the particles may be isolating, and that only a minor fraction is responding to the potential. We are currently investigating how to produce homogeneous Co_3O_4 spinel-structured films with controlled thicknesses on electrodes to see if we can overcome this limitation in future experiments.

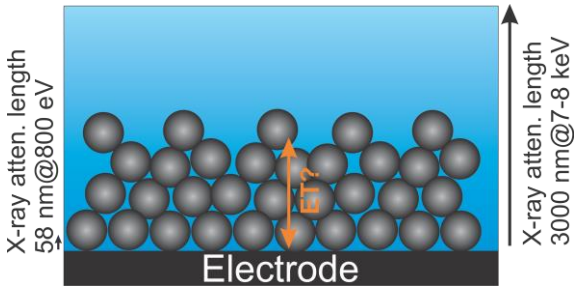

Figure 3. Schematic representation of the particles on an electrode and the attenuation lengths at different energies for X-ray. The arrows on the side of the figure are scaled to the represented particle size (assuming particles of around 150 nm in diameter).

References

1. T. Grewe, M. Meggouh and H. Tuysuz, *Chem.-Asian J.*, 2016, **11**, 22-42.
2. H. J. King, M. Fournier, S. A. Bonke, E. Seeman, M. Chatti, A. N. Jumabekov, B. Johannessen, P. Kappen, A. N. Simonov and R. K. Hocking, *The Journal of Physical Chemistry C*, 2019, **123**, 28533-28549.

INVESTIGATION OF THE ELECTRONIC STRUCTURE OF ELECTRODEPOSITED COBALT OXIDE FILMS ON ELECTRODES FOR WATER OXIDATION CATALYSTS USING CO 2P3D RIXS

Minmin Chen,[a] Kosuke Yamazoe,[b,c] Jun Miyawaki,[b,c] Yoshihisa Harada,[b,c] Serena DeBeer,[a] Olaf Rüdiger[a]

[a]*Max Planck Institute for Chemical Energy Conversion, Mülheim an der Ruhr, Germany*

[b]*Institute for Solid State Physics, The University of Tokyo, Kashiwa, Chiba 277-8581, Japan*

[c]*Synchrotron Radiation Research Organization, The University of Tokyo, 7-3-1 Hongo, Bunkyo-ku, Tokyo 113-8656, Japan*

Development of new anode materials based on earth abundant transition metals for water splitting is strategically important for industrial and large-scale applications. Water splitting has been considered one of the most promising strategies for energy conversion and storage.[1] Cobalt oxide films electrodeposited from Co^{2+} salts in neutral pH buffered solutions show high catalytic activity at low overpotential in mild environments, combined with extended stability as a result of a self-healing mechanism.[2] Although this catalyst has been studied over the last years using different spectroscopic techniques (including operando Co K-edge XAS) and EPR, most of the studies presented so far, did not employ ultra-pure electrolytes and it has recently been shown that trace amounts of iron dramatically improve the catalytic performance of such materials.[3] At this point, the role of iron in catalyst activation is still not fully understood.

We measured the Co L-edge XAS while we were electrodepositing Co oxide on the electrode from a solution of $Co(NO_3)_2$ 0.5 mM in phosphate buffer solution (PBS) at pH 7.0. In Figure 1, one can see that the electrode did not contain any Co. Once the cell was filled with the $Co(NO_3)_2$ solution, but kept at open circuit potential (OCP), we can already detect a cobalt signal from the Co in solution. As we apply a potential of 0.9 V (vs Ag/AgCl), the intensity of the Co L-edge increases. After the second 60 s potential pulse, the intensity does not increase any further, indicating that either the film does not grow anymore, or that the film is too thick and the growth goes beyond the penetration limit of the X-rays. After the electrodeposition, the electrolyte was switched to PBS without cobalt. Unfortunately, the Co signal rapidly disappears upon changing the electrolyte. Even if the potential was kept high to stabilize higher oxidation states on the film. If the electrolyte was switched to KOH 0.1 M, the films were more stable so that we could measure spectra at different applied potentials as a result of the lower solubility of Co at high pH.

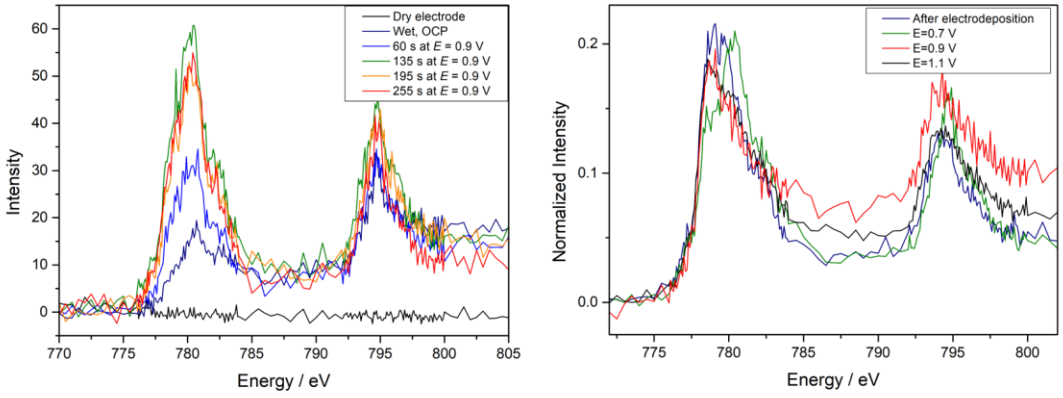

Figure 1. Co L-edge XAS of an electrode where Co was electrodeposited. On the left, the spectra measured during electrodeposition are shown. Measured in PBS pH 7.0 and in the presence of $Co(NO_3)_2$ 0.5 mM in solution. On the right figure, the L-edges measured at different applied electrode potentials in KOH 0.1 M.

Interestingly, the Co L-edge shifts to higher energy at 0.7 V (vs Ag/AgCl), with a maximum intensity for the L_3 at 782 eV, similar to what was measured for Co_2ZnO_4 (see our 2019 activity report on spinel Co_3O_4), suggesting that the cobalt has been oxidized to Co^{3+}. On the other hand, when the potential was increased and the catalyst started doing water oxidation the L-edge maximum shifts to lower energy (Figure 1).

The 2p3d RIXS spectra of these electrodeposited Co oxides is less structured than that measured for the spinel systems. The operando measurements showed just a small change at 779 eV excitation energy, where the spectra recorded at the highest potential did not show a separate feature at 1 eV (Figure 2).

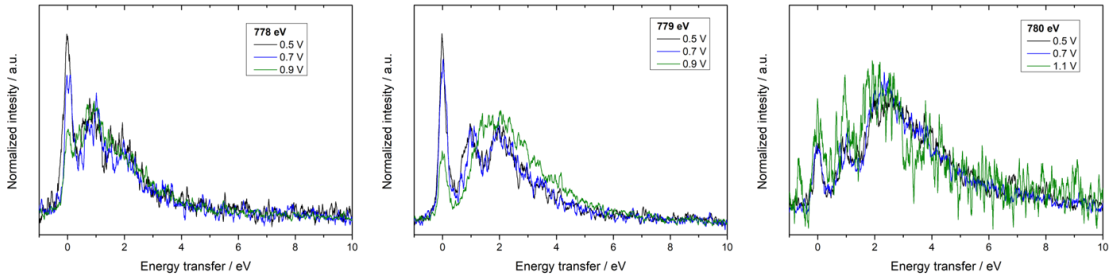

Figure 2. Corresponding 2p3d RIXS spectra measured for the electrodeposited Co oxide film shown in figure 6 at 3 different incident energies as indicated on the figure. Measured in KOH 0.1 M.

Operando studies in the soft X-ray regime are extremely challenging. On one hand, the experimental setup requires a vacuum environment, which makes the design of the spectroelectrochemical cell challenging. Nevertheless, we have successfully designed a cell that operates on a three-electrode configuration. The cell did not leak during the measurements.

The electrodeposited films showed a small response to the applied potential. We could monitor the film growth by following the Co L-edge XAS. Under basic pH conditions, the measured spectra suggest the formation of Co^{3+} at applied potentials just before the catalytic wave starts. Under turnover conditions, the L_3 edge shifts to lower energy, suggesting a Co^{2+} configuration. This may be because the rate-limiting step is the oxidation of Co^{2+}, and once this state is formed, water oxidation takes place at a fast rate, and the higher valence states cannot be observed on the time scale of the experiment. This contrasts with what we have measured using in situ EPR for the same catalyst, where a Co^{4+} signal was detected.[4] Nevertheless, EPR measurements are not real operando experiments, since the measurement requires low temperatures (10K). The freezing process may slow down the catalytic cycle and allow the detection of Co^{4+}.

REFERENCES

1. T. Grewe, M. Meggouh and H. Tuysuz, *Chem.-Asian J.*, 2016, **11**, 22-42.
2. C. Costentin and D. G. Nocera, *Proceedings of the National Academy of Sciences*, 2017, **114**, 13380-13384.
3. F. Song, L. Bai, A. Moysiadou, S. Lee, C. Hu, L. Liardet and X. Hu, *J. Am. Chem. Soc.*, 2018, **140**, 7748-7759.
4. Y. Kutin, N. Cox, W. Lubitz, A. Schnegg and O. Rüdiger, *catalysts*, 2019, **9**, 926.